

INTERNAL AND EXTERNAL SOURCE ELECTROSPRAY  
IONIZATION FOURIER TRANSFORM ION CYCLOTRON  
RESONANCE MASS SPECTROMETRY

BY

RAGULAN RAMANATHAN

A DISSERTATION PRESENTED TO THE GRADUATE SCHOOL  
OF THE UNIVERSITY OF FLORIDA IN PARTIAL FULFILLMENT  
OF THE REQUIREMENTS FOR THE DEGREE OF  
DOCTOR OF PHILOSOPHY

UNIVERSITY OF FLORIDA

1994

#### ACKNOWLEDGEMENTS

I would like to express my sincere thanks to Dr. John R. Eyler for his constant support, patience and guidance throughout this work. Special appreciation is extended to Drs. Martin Vala, Kirk Schanze, Robert Hanrahan and Gar Hoflund, members of my committee, for their time and helpful suggestions.

I would like to thank past group members for their friendship and help in getting me started in Dr. Eyler's research group. In addition, I would like to thank all my colleagues for their assistance with my experiments. In particular, I would like to thank Dil Peiris for help, support and encouragement during my graduate studies.

The excellent technical facilities (machine and electronic shops) available in the department of chemistry have greatly facilitated this work. I thank specially Mr. Joseph Shalosky; without his machining skills and dedication, I doubt that I could have completed most of the work presented in chapter 3.

This work would not have been possible without the love, encouragement and support of my parents and brothers.

## TABLE OF CONTENTS

	<u>Page</u>
ACKNOWLEDGMENTS.....	ii
TABLE OF CONTENTS.....	iii
LIST OF FIGURES.....	vi
LIST OF TABLES.....	xiv
ABSTRACT.....	xv
CHAPTER	
1    INTRODUCTION.....	1
Ionization Methods.....	2
Electron Ionization and Chemical Ionization.	2
Field Desorption.....	3
Secondary Ion.....	4
Fast Atom Bombardment.....	4
Plasma Desorption.....	5
Electrohydrodynamic Ionization.....	6
Laser Desorption.....	7
Matrix Assisted Laser Desorption/Ionization.	7
Electrospray Ionization.....	9
Mass Spectrometric Methods.....	11
Time of Flight.....	11
Ion Trap.....	13
Quadrupole.....	14
Magnetic Sector.....	16
Fourier Transform Ion Cyclotron Resonance...	18
Scope of the Dissertation.....	21
2    THEORY AND INSTRUMENTATION.....	24
FTICR Mass Spectrometry.....	24
Historical Evaluation.....	24
Ion Formation and Trapping.....	25
Ion Excitation.....	28
Ion Detection.....	34
FTICR Analyzer Cell.....	41
Mass Resolution.....	43
Mass Accuracy.....	44

Electrospray Ionization.....	46
Ion Formation Process.....	46
Charged Droplet Formation.....	50
Gas Phase Ion Formation from Charged Droplet.....	50
Spray Needle Operated at High Voltage.....	51
Needle Operated at Ground Potential.....	54
Instrumentation.....	56
Internal Source ESI/FTICR Mass Spectrometer.	56
FTICR Cell Used in Internal ESI Studies.....	58
FTICR Pulse Sequences Used with Internal ESI Experiments.....	60
External Source ESI/FTICR Mass Spectrometer.	63
FTICR Cell Used in External ESI Studies.....	64
Laser Desorption FTICR Mass Spectrometer....	67
FTICR Cell Used in LD Studies.....	68
FTICR Pulse Sequences Used with LD Experiments.....	68
 3 DEVELOPMENT AND OPTIMIZATION OF INTERNAL SOURCE ELECTROSPRAY IONIZATION FTICR MASS SPECTROMETER.....	70
Introduction.....	70
Concentric Tube Vacuum Chamber Assembly.....	73
First Differentially Pumped Vacuum Chamber.....	74
Second Differentially Pumped Vacuum Chamber....	76
Third and Fourth Differentially Pumped Vacuum Chambers.....	78
Optimization of the ESI Source.....	82
Optimization of the Spray Needle-Capillary Distance, Spray Needle Potential and the Sample Solution Flow Rate.....	93
Optimization of the Desolvating Capillary.....	105
Optimization of the Skimmer/Lens Holder Assembly.....	112
Optimization of the Capillary-Skimmer Distance.....	120
Optimization of the Trapping Versus Skimmer Potentials.....	131
Unstable Spray Due To Heat Transfer.....	135
High Magnetic Field Shutter.....	136
Conclusions.....	140
 4 APPLICATIONS OF THE INTERNAL SOURCE ELECTROSPRAY IONIZATION FTICR MASS SPECTROMETER.....	145
Introduction.....	145
Experimental.....	147
Results and Discussion.....	148

Application To Organic Molecules.....	148
Application To Biological Molecules.....	153
Application To Organometallic Complexes.....	156
Conclusions.....	165
 5 APPLICATIONS OF THE EXTERNAL SOURCE ELECTROSPRAY IONIZATION FTICR MASS SPECTROMETER TO ORGANOMETALLIC COMPLEXES.....	172
Introduction.....	172
Experimental.....	177
Results.....	179
Discussion.....	180
Capillary/Skimmer CID.....	180
In-Cell CID.....	199
Conclusions.....	204
 6 ELECTRON AFFINITIES OF SMALL CARBON CLUSTERS.....	206
Introduction.....	206
Experimental.....	212
Results.....	215
Discussion.....	221
Carbon Cluster Distribution.....	221
Charger-Transfer Reactions Versus Side Reactions.....	225
EA's of C <sub>4</sub> - C <sub>9</sub> .....	236
Conclusions.....	244
 7 CONCLUSIONS AND FUTURE WORK.....	245
Conclusions.....	245
Future Work.....	247
Instrument Modifications.....	247
Negative Ion Electrospray.....	248
 REFERENCES.....	252
 BIOGRAPHICAL SKETCH.....	271

LIST OF FIGURES

<u>Figures</u>	<u>Page</u>
2.1 Digitized time domain signal due to $[\text{Ru}(\text{bpy})_3]^{2+}$ produced by the internal source ESI/FTICR mass spectrometer ( $1 \times 10^{-5}$ M $[\text{Ru}(\text{bpy})_3](\text{PF}_6)_2$ in 49/49/2 methanol/water/acetonitrile solution).....	36
2.2 Digitized time domain signal due to $\text{C}_2^- - \text{C}_{10}^-$ produced by laser desorption from a graphite plug.....	38
2.3 Mass spectrum of $[\text{Ru}(\text{bpy})_3]^{2+}$ resulting from Fourier transformation of the transient observed in Figure 2.1.....	39
2.4 Mass spectrum of $\text{C}_2^- - \text{C}_{10}^-$ resulting from Fourier transformation of the transient observed in Figure 2.2.....	40
2.5 Ion formation process in electrospray.....	48
2.6 A schematic representation of the internal electrospray source used with the 2 T FTICR mass spectrometer.....	52
2.7 A schematic representation of the external electrospray source used with the 4.7 T FTICR mass spectrometer.....	55
2.8 A schematic representation of the internal source electrospray ionization FTICR mass spectrometer.....	57
2.9 A schematic representation of the cubic FTICR cell used with internal source ESI/FTICR mass spectrometry.....	61
2.10 Pulse sequence used with internal source ESI/FTICR mass spectrometry.....	62
2.11 A schematic representation of the external source electrospray ionization FTICR mass spectrometer.....	65

2.12 A schematic representation of the Infinity FTICR cell used with external source ESI/FTICR mass spectrometry.....	66
3.1 A schematic representation of the first differentially pumped vacuum chamber and its components.....	75
3.2 A schematic representation of the second differentially pumped vacuum chamber and its components.....	77
3.3 A schematic representation of the third and the fourth differentially pumped vacuum chambers and their components.....	79
3.4 Concentric tube vacuum chamber assembly positioned inside the bore of the 2 Tesla FTICR mass spectrometer.....	81
3.5 A schematic representation of the first design adopted in constructing the internal ESI source..	83
3.6 A schematic representation of the "ESI source I" positioned inside the 1.9 cm od stainless steel probe.....	85
3.7 A schematic representation of the second design adopted in constructing the internal ESI source..	87
3.8 A schematic representation of the "ESI source II" positioned inside the 1.9 cm od stainless steel probe.....	88
3.9 A schematic representation of the third design adopted in constructing the internal ESI source..	90
3.10 A schematic representation of the fourth design adopted in constructing the internal ESI source..	92
3.11 A schematic representation of the electrical connections to the spray needle and the desolvating capillary during (top) ESI/FTICR experiments or detection of ion beam current on the skimmer and (bottom) detection of ion current on desolvating capillary away from the magnetic field.....	98
3.12 A plot of ion beam current detected at the desolvating capillary vs. the spray needle potential with respect to sample solution flow rate corresponding to a distance of 5 mm between the spray needle and the desolvating capillary... 101	

3.13 A plot of ion beam current detected at the desolvating capillary vs. the spray needle potential with respect to sample solution flow rate corresponding to a distance of 6 mm between the spray needle and the desolvating capillary...	102
3.14 A plot of ion beam current detected at the desolvating capillary vs. the spray needle potential with respect to sample solution flow rate corresponding to a distance of 7 mm between the spray needle and the desolvating capillary...	103
3.15 A plot of ion beam current detected at the desolvating capillary vs. the spray needle potential with respect to sample solution flow rate corresponding to a distance of 10 mm between the spray needle and the desolvating capillary...	104
3.16 A schematic representation of the vacuum chamber used in detecting the ion beam current exiting the capillary without the magnetic field.....	106
3.17 A schematic representation of the internal ESI/FTICR mass spectrometer modified to accommodate the 2.5 m long probe which was used in monitoring the ion beam current along the z-axis.....	110
3.18 A schematic representation of the first design adopted in constructing the skimmer holder.....	113
3.19 A schematic representation of the second design adopted in constructing the skimmer holder.....	115
3.20 A plot of ion kinetic energy and pressure in the cell region as a function of the distance between the desolvating capillary exit orifice and the skimmer entrance.....	117
3.21 SIMION plot of ion trajectories and electrostatic field lines in the capillary-skimmer and the first conductance limiting region: (top) without the tube lens and (bottom) with the tube lens.....	118
3.22 SIMION plot of ion trajectories and electrostatic field lines in the capillary-skimmer and the first conductance limiting region (top) without the magnetic field and (bottom) with the 1.8 Tesla magnetic field.....	119
3.23 A schematic representation of the third design adopted in constructing the skimmer holder and the ESI source positioned inside it.....	121

3.24 A schematic representation showing the expansion of molecules and ions at near atmospheric pressure from the desolvating capillary into the capillary - skimmer region. Sampling of molecules and ions with the skimmer orifice positioned at the mach distance and within the silent zone (magnetic and electrostatic fields are absent) ..	123
3.25 A schematic representation showing the expansion of molecules and ions at near atmospheric pressure from the desolvating capillary into the capillary - skimmer region. Sampling of molecules and ions with the skimmer orifice positioned away from the mach distance and outside the silent zone (magnetic and electrostatic fields are absent) ..	125
3.26 A schematic representation showing the expansion of molecules and ions at near atmospheric pressure from the desolvating capillary into the capillary - skimmer region. Sampling of molecules and ions with the skimmer orifice positioned away from the mach distance and within the silent zone (magnetic and electrostatic fields are absent) ..	126
3.27 A plot of ion beam current detected on the front trap plate as a function of the potential applied to the second conductance plate obtained with skimmer biased at 10 V.....	128
3.28 A plot of ion beam current detected on the front trap plate as a function of the potential applied to the second conductance plate obtained with skimmer biased at 15 V.....	129
3.29 A plot of ion beam current detected on the front trap plate as a function of the potential applied to the second conductance plate obtained with skimmer biased at 30 V.....	130
3.30 Trapping profile of electrospray ions produced from $1 \times 10^{-5}$ M Ru(bpy) <sub>3</sub> (PF <sub>6</sub> ) <sub>2</sub> in 48/48/2 methanol/water/acetonitrile solution corresponding to a skimmer potential of (top) 3 V and (bottom) 4 V.....	132
3.31 Trapping profile of electrospray ions produced from $1 \times 10^{-5}$ M Ru(bpy) <sub>3</sub> (PF <sub>6</sub> ) <sub>2</sub> in 48/48/2 methanol/water/acetonitrile solution corresponding to a skimmer potential of (top) 6 V and (bottom) 7 V.....	133

3.32	Trapping profile of electrospray ions produced from $1 \times 10^{-5}$ M $\text{Ru}(\text{bpy})_3(\text{PF}_6)_2$ in 48/48/2 methanol/water/acetonitrile solution corresponding to a skimmer potential of (top) 10 V and (bottom) 12 V.....	134
3.33	A schematic representation of the high magnetic field shutter used with the internal source ESI/FTICR mass spectrometer.....	137
3.34	A schematic representation of the electrical circuit used to control the high magnetic field shutter.....	138
3.35	ESI/FTICR mass spectrum of $\text{Ru}(\text{bpy})_3(\text{PF}_6)_2$ obtained without the shutter using $1 \times 10^{-5}$ M 49/49/2 methanol/water/acetonitrile solution and detected using the broadband mode (15-1000 Da).....	141
3.36	ESI/FTICR mass spectrum of $\text{Ru}(\text{bpy})_3(\text{PF}_6)_2$ obtained with the shutter using $1 \times 10^{-5}$ M 49/49/2 methanol/water/acetonitrile solution and detected using the broadband mode (15-1000 Da).....	142
4.1	Mass spectra obtained electrospraying $1 \times 10^{-5}$ M Rhodamine 6G perchlorate in 50/50 methanol/water solution with capillary/skimmer CID energy of: (top) 240 V and (bottom) 420 V. The inset shows the high resolution mass spectrum with $^{13}\text{C}$ isotopes resolved.....	150
4.2	Mass spectra obtained electrospraying $1 \times 10^{-5}$ M rhodamine 6G perchlorate in 50/50 methanol/water solution with varying capillary/skimmer CID energies.....	152
4.3	Mass spectrum obtained electrospraying $1 \times 10^{-5}$ M cytochrome C in 49.9/49.9/0.2 methanol/water/ acetic acid solution. The inset shows the high resolution mass spectrum of the charge state 16... 155	
4.4	Mass spectrum obtained electrospraying $1 \times 10^{-5}$ M $\text{Ru}(\text{bpy})_3(\text{PF}_6)_2$ in 49/49/2 methanol/water/ acetonitrile solution (capillary/skimmer CID energy of 22 V).....	159
4.5	Mass spectrum obtained electrospraying $1 \times 10^{-5}$ M $\text{Ru}(\text{phen})_3(\text{PF}_6)_2$ in 49/49/2 methanol/water/ acetonitrile solution (capillary/skimmer CID energy of 22 V).....	160

4.6	Comparison of theoretically simulated mass spectrum with experimentally obtained mass spectrum of $[\text{Ru}(\text{bpy})_3]^{2+}$ .....	161
4.7	Comparison of theoretically simulated mass spectrum with experimentally obtained mass spectrum of $[\text{Ru}(\text{phen})_3]^{2+}$ .....	162
4.8	Mass spectra obtained electrospraying $1 \times 10^{-5}$ M $[\text{Ru}(\text{NH}_3)_5(\text{C}_4\text{N}_2\text{H}_4)](\text{PF}_6)_2$ in 49/49/2 methanol/water/acetonitrile solution with capillary/skimmer CID energy of (top) 28 V and (bottom) 60 V .....	163
4.9	Mass spectra obtained electrospraying $1 \times 10^{-5}$ M $[\text{Ru}(\text{NH}_3)_5(\text{C}_4\text{N}_2\text{H}_4)](\text{PF}_6)_2$ in 49/49/2 methanol/water/acetonitrile solution with capillary/skimmer CID energy of (top) 104 V and (bottom) 154 V.....	164
4.10	Comparison of theoretically simulated mass spectrum with experimentally obtained mass spectrum of $[\text{Ru}(\text{NH}_3)_5(\text{C}_4\text{N}_2\text{H}_4)\text{CH}_3\text{CN}]^{2+}$ .....	166
4.11	Mass spectra obtained electrospraying $1 \times 10^{-5}$ M $\text{Ru}(\text{bpy})_3(\text{PF}_6)_2$ in 49/49/2 methanol/water/acetonitrile solution with capillary/skimmer CID energy of (top) 94 V and (bottom) 144 V.....	167
4.12	Mass spectra obtained electrospraying $1 \times 10^{-5}$ M $\text{Ru}(\text{bpy})_3(\text{PF}_6)_2$ in 49/49/2 methanol/water/acetonitrile solution with capillary/skimmer CID energy of (top) 194 V and (bottom) 244 V.....	168
4.13	Mass spectra obtained electrospraying $1 \times 10^{-5}$ M $\text{Ru}(\text{bpy})_3(\text{PF}_6)_2$ in 49/49/2 methanol/water/acetonitrile solution with capillary/skimmer CID energy of (top) 294 V and (bottom) 344 V.....	169
4.14	Mass spectra obtained electrospraying $1 \times 10^{-5}$ M $\text{Ru}(\text{phen})_3(\text{PF}_6)_2$ in 49/49/2 methanol/water/acetonitrile solution with capillary/skimmer CID energy of (top) 94 V and (bottom) 154 V.....	170
4.15	Mass spectra obtained electrospraying $1 \times 10^{-5}$ M $\text{Ru}(\text{phen})_3(\text{PF}_6)_2$ in 49/49/2 methanol/water/acetonitrile solution with capillary/skimmer CID energy of (top) 224 V and (bottom) 254 V.....	171
5.1.	External source ESI/FTICR mass spectrum of $[\text{Ag}_2(\text{DPM})_2](\text{BF}_4)_2$ obtained with capillary/skimmer CID energy of 29 V.....	184

5.2. External source ESI/FTICR mass spectrum of [Ag <sub>2</sub> (DPM) <sub>2</sub> ](BF <sub>4</sub> ) <sub>2</sub> obtained with capillary/skimmer CID energy of 244 V.....	185
5.3. External source ESI/FTICR mass spectrum of [Ag <sub>2</sub> (DPM) <sub>2</sub> ](BF <sub>4</sub> ) <sub>2</sub> obtained with capillary/skimmer CID energy of 29 V.....	186
5.4. External source ESI/FTICR mass spectrum of [Ag <sub>2</sub> (DPM) <sub>3</sub> ](BF <sub>4</sub> ) <sub>2</sub> obtained with capillary/skimmer CID energy of 244 V.....	187
5.5. External source ESI/FTICR mass spectrum of [Ru(bpy) <sub>3</sub> ](PF <sub>6</sub> ) <sub>2</sub> obtained with capillary/skimmer CID energy of 29 V.....	188
5.6. External source ESI/FTICR mass spectrum of [Ru(bpy) <sub>3</sub> ](PF <sub>6</sub> ) <sub>2</sub> obtained with capillary/skimmer CID energy of 29 V.....	189
5.7. Mass spectra from in-cell CID of [Ag <sub>2</sub> (DPM) <sub>2</sub> ] <sup>2+</sup> . CID pulse width was (amplitude was 36 V <sub>p-p</sub> ): (a) 0.3 $\mu$ s; (b) 1 $\mu$ s; (c) 2 $\mu$ s; (d) 5 $\mu$ s; and (e) 10 $\mu$ s.....	202
6.1. Mass spectra of carbon cluster anions observed following laser vaporization of a graphite plug by 10.60 $\mu$ m wavelength light from a CO <sub>2</sub> laser with (top) 500 mJ/pulse and (bottom) 900 mJ/pulse.....	218
6.2. Ion intensity vs. reaction time plot for the reaction of C <sub>4</sub> <sup>-</sup> with 1,4-naphthoquinone.....	226
6.3. Mass spectra following C <sub>4</sub> <sup>-</sup> reaction with 1,4-naphthoquinone obtained at reaction times of (top) 800 ms and (bottom) 5000 ms.....	227
6.4. Ion intensity vs. reaction time plot for the reaction of C <sub>6</sub> <sup>-</sup> with 1,4-naphthoquinone.....	229
6.5. Mass spectra following C <sub>6</sub> <sup>-</sup> reaction with 1,4-naphthoquinone obtained at reaction times of (top) 100 ms and (bottom) 1500 ms.....	230
6.6. Mass spectra following C <sub>6</sub> <sup>-</sup> reaction with 1,4-naphthoquinone obtained at reaction times of (top) 4000 ms and (bottom) 10000 ms.....	231
6.7. Ion intensity vs. reaction time plot for the reaction of C <sub>4</sub> <sup>-</sup> with 1,4-dinitrobenzene.....	232

6.8	Mass spectra following C <sub>4</sub> <sup>-</sup> reaction with 1,4-dinitrobenzene obtained at reaction times of (top) 500 ms and (bottom) 10000 ms.....	233
6.9	Ion intensity vs. reaction time plot for the reaction of C <sub>5</sub> <sup>-</sup> with 2,6-dichloro- 1,4-benzoquinone.....	235
6.10	Mass spectrum following C <sub>5</sub> <sup>-</sup> reaction with 2,6-dichloro-1,4-benzoquinone obtained at 5000 ms reaction time while continuously ejecting <sup>37</sup> Cl <sup>-</sup> .....	237
6.11	Ion intensity vs. reaction time plot for the reaction of C <sub>8</sub> <sup>-</sup> with 2,6-dichloro-1,4- benzoquinone.....	238
6.12	Mass spectrum following C <sub>8</sub> <sup>-</sup> reaction with 2,6-dichloro-1,4-benzoquinone obtained at 6000 ms reaction time.....	239
7.1	Mass spectrum obtained electrospraying 1 × 10 <sup>-5</sup> M MnCl <sub>2</sub> and CaF <sub>2</sub> in 50/50 methanol/water solution.....	251

LIST OF TABLES

<u>Tables</u>	<u>Page</u>
3.1 Comparison of calculated and experimental V <sub>on</sub> values.....	96
3.2 Results from optimization of the desolvating capillary.....	107
5.1 Capillary/Skimmer CID results for $\text{Ag}_2(\text{DPM})_3(\text{BF}_4)_2$ .....	181
5.2 Capillary/Skimmer CID results for $\text{Ag}_2(\text{DPM})_3(\text{BF}_4)_2$ .....	182
5.3 Capillary/Skimmer CID results for $\text{Ru}(\text{bpy})_3(\text{PF}_6)_2$ .....	183
5.4 In-cell CID of $[\text{Ag}_2(\text{DPM})_2\text{CH}_3\text{COO}]^+$ produced from external source ESI.....	190
5.5 In-cell CID of $[\text{Ag}_2(\text{DPM})_2]^{2+}$ produced from external source ESI.....	191
5.6 In-cell CID of $[\text{Ru}(\text{bpy})_3]^{2+}$ produced from external source ESI.....	192
6.1 Charge-transfer reference compounds used in this chapter and their EA's.....	216
6.2 Results from reaction between C <sub>n</sub> <sup>-</sup> and charge- transfer reference compounds.....	219
6.3 Comparison of experimental and theoretical EA's of C <sub>4</sub> - C <sub>9</sub> .....	220
6.4 C <sub>n</sub> <sup>-</sup> reactions other than charge-transfer with charge-transfer reference compounds.....	222

Abstract of Dissertation Presented to the Graduate School  
of the University of Florida in Partial Fulfillment of the  
Requirements for the Degree of Doctor of Philosophy

INTERNAL AND EXTERNAL SOURCE ELECTROSPRAY IONIZATION  
FOURIER TRANSFORM ION CYCLOTRON RESONANCE MASS SPECTROMETRY

By

RAGULAN RAMANATHAN

December 1994

Chairman: John R. Eyler

Major Department: Chemistry

Since the coupling of electrospray ionization (ESI) with mass spectrometry in the early 1980s, ESI mass spectrometry has become a powerful tool for the analysis of a wide variety of compound types, ranging from metal ions to proteins. Intact proteins and peptides, which only a few years ago were completely inaccessible by mass spectrometry due to their high molecular weight and the requirement of a "soft" ionization method, are now routinely analyzed in the gas-phase. Electrospray ionization FTICR mass spectrometry further benefits from its high mass resolution and high mass accuracy.

Two types of ESI/FTICR mass spectrometers have been characterized in this dissertation. The first type positioned an electrospray source inside the high magnetic field of a FTICR mass spectrometer (internal) and the

magnetic field was used to focus the ions into the analyzer cell. The second type involved generating the ions outside the magnetic field (external) and transferring the ions using several electrostatic lenses.

Development and optimization of the internal electrospray source is presented in detail. Internal source ESI/FTICR mass spectrometry was used to study a variety of compound classes including cytochrome c,  $[\text{Ru}(2,2'\text{-bipyridyl})_3](\text{PF}_6)_2$ ,  $[\text{Ru}(1,10'\text{-phenanthroline})_3](\text{PF}_6)_2$  and  $[\text{Ru}(\text{NH}_3)_5(\text{C}_4\text{H}_4\text{N}_2)](\text{PF}_6)_2$ . The capillary/skimmer collision induced dissociation (CID) method was used to obtain detailed structural information on these molecules. The external source ESI/FTICR mass spectrometer was used to study fragmentation pathways of  $[\text{Ag}_2(\text{bis-diphenylphosphino-methane})_2](\text{BF}_4)_2$ ,  $[\text{Ag}_2(\text{bis-diphenylphosphino-methane})_3](\text{BF}_4)_2$  and  $[\text{Ru}(2,2'\text{-bipyridyl})_3](\text{PF}_6)_2$ . Both capillary/skimmer CID and CID in the analyzer cell were compared for obtaining fragmentation pathways of these complexes.

In addition, ion-molecule reactions between laser generated carbon cluster anions and several neutral electron affinity (EA) reference compounds were monitored and the EA's of  $\text{C}_4$  through  $\text{C}_9$  were bracketed successfully using the charge-transfer bracketing technique. Electron affinities of small carbon clusters along with several interesting side reactions are presented.

## CHAPTER 1 INTRODUCTION

Mass spectrometry, because of its high sensitivity and specificity, has been widely accepted by scientists as a technique for obtaining structural information, identifying unknown compounds and quantifying trace amounts of compounds in mixtures. Major factors which have contributed to the widespread application of the technique include minimum sample requirement, fast analysis time and detection based on mass and not on chromophores, flourophores, magnetic or dipole moments.

The utility of mass spectrometric methods for precise studies of atoms, isotopes, and small molecules was first recognized by J. J. Thomson in 1913 (1). For several years following Thomson's pioneering work, much effort went into obtaining a better vacuum to prevent unwanted ion/molecule reactions. In 1945, Hipple and Condon (2) observed and explained the presence of metastable ions and took the mass spectrometric technique one step forward. Since then mass spectrometry has found a wide variety of applications including determination of molecular composition and structure of unknown samples and studying energetics of gaseous ions and their reactions with neutral molecules and surfaces.

Ionization MethodsElectron Ionization and Chemical Ionization

The ion formation process is the starting point of mass spectrometric analysis and governs the limits and utility of this technique. Since the early days of mass spectrometry, most workers have relied on electron ionization (EI) (3) and chemical ionization (CI) (4) to create ions from vaporized neutral molecules. In EI, the source of electrons is usually a thin filament of metal (e.g. rhenium) which is heated electrically to emit electrons. These electrons are accelerated to high energies (typically 45-70 and 1-10 eV for positive and negative ions, respectively) to interact with gaseous samples present in the vacuum chamber. The efficiency of EI depends on the sample pressure and on the cross section of the electron beam. In CI, EI is used to ionize the CI gas (e.g. methane, isobutane, NH<sub>3</sub>) and subsequently a sample of interest is ionized by collisions with CI gas ions. For example, if methane is used as the CI gas, CH<sub>4</sub><sup>+</sup> is produced by EI along with some fragment ions of methane. Ion/molecule reactions lead to the formation of CH<sub>5</sub><sup>+</sup> and C<sub>2</sub>H<sub>5</sub><sup>+</sup>, which do not react further with methane molecules. Subsequently, when an analyte molecule (M) with higher proton affinity than methane is present, MH<sup>+</sup> is formed. These methods have one feature in common: they require the sample to be in the gas

phase and vapor pressures of  $10^{-7}$  to  $10^{-5}$  Torr have to be obtained by leaking in or heating the sample. These requirements excluded many classes of organic, inorganic, and biological molecules from mass spectrometric studies.

In order to circumvent the problems with EI and CI, new ionization methods such as field desorption (FD), plasma desorption (PD), laser desorption (LD), fast atom bombardment (FAB), secondary ion (SI), matrix-assisted laser desorption (MALDI) and electrospray ionization (ESI) were developed.

#### Field Desorption

In 1969, Beckey (5-6) used FD to obtain a mass spectrum of glucose and demonstrated the ability of FD to ionize less volatile compounds. In the FD technique a sample is coated on a filament or emitter on which microneedles of pyrolytic carbon have been grown. Then the emitter with the sample is placed in a high electric field of  $10^7$  to  $10^8$  V/cm (7) to produce the ions. The FD technique provided some of the earliest breakthroughs in the analysis of less volatile samples. Its application to such samples has been demonstrated by Schulten et al.(8) and Wada et al.(9). Excessive ion fragmentation during heating of the emitter, problems with emitter breaking and difficulties in establishing optimal FD conditions limited the application of this technique to less volatile samples.

Secondary Ion

The SI technique involves bombarding the sample with a beam of primary ions accelerated roughly to 2 to 20 kV followed by mass analysis of the secondary ions that are ejected from the sample surface. Argon, xenon, or cesium ions are most often used as the primary beam in this technique (10). SI mass spectrometry (SIMS) has been widely used for elemental analysis of surfaces and solids. In addition, it has been applied to polymers in the mass range of m/z 10,000 (11) and to some peptides (12). However, problems with charge buildup on the sample surface and thermal degradation have limited its application to less volatile molecules.

Fast Atom Bombardment

In 1981 the role of mass spectrometry in the analysis of fragile, less volatile molecules was dramatically changed by the development FAB technique (13). In this technique the sample is first mixed with a suitable liquid matrix (e.g. glycerol or thioglycerol) and then a beam of high energy (accelerated to 2-8 kV) atoms (e.g. xenon or argon) is used to bombard the matrix/sample surface. Although FAB is closely related to the SI technique, the ability of the liquid matrix to resupply fresh sample to the surface and the elimination of

ion source charging problems made it suitable for the analysis of less volatile samples. Naylor et al. (14) have demonstrated application of the FAB technique for the analysis of high molecular weight peptides. However, a number of problems limit the application of this technique to less volatile samples (i) formation of cluster ions from the matrix; (ii) requirement of an internal standard to eliminate problems with variations in ion intensities from sample to sample; and (iii) mass spectra which reflect only the molecules present on the surface when a mixture is analyzed. To circumvent the problems with FAB Caprioli et al. (15) introduced continuous flow FAB (CF-FAB). This new technique allowed peptides as large as trypsinogen (24,000 Da) to be analyzed using FAB (16). In addition CF-FAB has been interfaced with several liquid chromatographic (LC) techniques (17-18). Through these interfaces mass spectrometry was used to identify the components of a mixture which were separated by LC techniques.

#### Plasma Desorption

Plasma desorption mass spectrometry (PDMS) was first demonstrated by McFarlane et al.(19) in 1974. The sample is supported on a thin nickel foil or aluminized mylar and desorbed by the passage of high-energy (80-100 MeV) fission

fragments that result from radioactive decay of  $^{252}\text{Cf}$ . Recent developments in sample matrix optimization, such as using a nitrocellulose matrix, have greatly increased the PD ionization efficiency and increased the upper mass limit for this technique (20). Both protonated and multiprotonated molecular ions are common when a nitrocellulose matrix is used with this technique. The highest molecular weight reported using this technique is currently about 45,000 Da, the molecular weight of bovine serum albumin (21).

#### Electrohydrodynamic Ionization

In the electrohydrodynamic (EH) technique samples are dissolved in a solvent of low volatility (e.g. glycerol) and an electrolyte (e.g. NaCl, NaI, or KCl) is added to the solution to ionize the molecules (22-23). Then the solution is introduced into a capillary which is held at high potential and the charged droplets are extracted into the mass spectrometer. The formation of ions occurs in the solution via electrolytic dissociation or by ion attachment. Sodium attached ions up to 1900 Da have been observed with the EH technique (24). Problems with analyte-solvent interactions and difficulties in droplet desolvation after desorption limited this technique from application to less volatile samples, organometallic complexes, peptides and proteins.

Laser Desorption

The first laser desorption (LD) mass spectrometric study was reported by Honig et al. (25) in 1963. The sample is placed on a metal surface and bombarded with an intense photon beam. Intact molecular ions and/or H<sup>+</sup>, Na<sup>+</sup> or K<sup>+</sup> attached adduct ions are produced when the LD technique is used. Application of LD to study peptides, porphyrins and polymers has been demonstrated (26-28). LD appears to be mainly a thermal process and the extent of ion fragmentation is influenced by (i) the power density of irradiation; (ii) the wavelength of irradiation; (iii) the incident angle of irradiation; (iv) the thickness of the sample; and (v) the presence of a matrix. As in PD and FAB a matrix is not required in LD, although absorbance of the laser light by the sample or matrix reduces the fragmentation processes.

Matrix Assisted Laser Desorption/Ionization

Matrix assisted laser desorption/ionization (MALDI) is a popular outgrowth of LD technique. In 1988, Tanaka et al. (29) used a liquid matrix and demonstrated this technique. The use of solid matrices for MALDI was demonstrated by Karas and Hillenkamp (30) and later by Beavis and Chait (31). In a typical MALDI experiment, the analyte is deposited from a solution onto a metal probe along with a 100 to 50,000 M

excess of a suitable matrix. Then the solvents are allowed to evaporate and the sample is introduced into the mass spectrometer. Irradiation with a suitable laser (e.g. pulsed CO<sub>2</sub> laser (IR) or N<sub>2</sub> laser (UV)) causes ablation of the sample/matrix combination and ionization of the intact analyte (32a). It is clear from the studies of Cotter et al. (32b) and Vertes (32c) that the matrix plays a key role in the energy deposition process and the matrix enhancement is observed only when the wavelength of the laser is in resonance with an electronic or vibrational transition of the matrix (32). However, the process of ionization is not well understood (whether the ions are preformed before solution is deposited or ions are formed in the laser plume). Proteins and peptides in the range of 50,000 to 150,000 have been analyzed using the MALDI technique (33-34). Despite the enormous impact of MALDI on mass spectrometric analysis of less volatile molecules, problems with selecting a proper matrix and sample preparation methods have affected the efficiency of this technique. Since sample preparation/introduction for MALDI is done manually, on-line use of MALDI with chromatographic techniques has been precluded. However, Russell et al. (35) overcame this limitation by using aerosol MALDI and showed that chromatographic techniques can be interfaced with MALDI. In addition, aerosol MALDI avoids problems with reproducibility of sample preparation.

Electrospray Ionization

Electrospray ionization has literally revolutionized the mass spectrometric field over last few years. This breakthrough in mass spectrometry can be attributed to the multiple charging processes of the ESI technique. These processes allow conventional mass spectrometers with a m/z 500 to 2000 mass range to detect molecular masses up to 200,000 Da (36). Intact proteins of molecular mass 132,000 Da with as many as 100 charges has been observed with this technique (37).

Roots of ESI mass spectrometry can be traced back to the experiments performed by Dole et al. (38a). Although the study of electrospray phenomena extends back to the work done by Zeleny (38b), ESI/MS studies started after Dole's initial experiments. In 1968, Dole et al. attempted to obtain mass spectra of polystyrene macroions of 411,000 Da using the ESI technique. Dole tried to spray very dilute solutions of macromolecules into a gas filled chamber. The solution was forced through a hypodermic needle held at high potential to produce charged aerosol droplets. Since conventional mass spectrometers available at the time could not accommodate macromolecules, a Faraday cage or cup and a repeller grid were used to distinguish between the macroions and the low molecular weight solvent or nitrogen gas ions. The repeller potential required to stop the ions from entering the Faraday cage was measured. This potential was assumed to be equal to

the kinetic energy of the ion. Several voltage/current curves were obtained and compared with theoretical retarding potential for a particular ion.

A second attempt was made in 1973 by Dole et al. (39) to couple ESI with a time of flight (TOF) mass spectrometer. This resulted in limited success due to difficulties in transporting the ions into the mass spectrometer and detecting the ions with a normal secondary electron multiplier. A third and final attempt was made in 1977 by Dole et al. (40) to couple ESI with an ion drift mass spectrometer. This did not succeed due to excess formation of clusters and multiply charged ions. In 1981, Dole abandoned the work on ESI/MS and concluded that accurate molecular weights of high molecular weight samples could not be determined using this technique (41).

The explosive growth of ESI as an analytical tool came about in 1984 after Fenn et al. (42) and Aleksandrov et al. (43) demonstrated its capabilities in determining the molecular weight of less volatile samples via the formation of multiply charged ions. Fenn and Aleksandrov used quadrupole and magnetic sector mass spectrometers, respectively.

The availability of advanced technology allowed Fenn et al.(42) to overcome the difficulties encountered by Dole et al. (38-40). Since Fenn's demonstration, ESI has been successfully coupled with virtually every type of mass spectrometer including time of flight, ion trap, quadrupole,

magnetic sector and Fourier transform ion cyclotron resonance. Coupling of ESI sources with mass spectrometers benefits from the ability to (i) detect high molecular weight ions because of the multiple charging process; (ii) perform MS/MS experiments either in the ESI interface or in the mass analyzer; (iii) interface with LC techniques; (iv) study thermally unstable molecules; and (v) detect ions formed in solution.

#### Mass Spectrometric Methods

##### Time of Flight

Time of flight (TOF) mass spectrometry involves measuring the time required for an ion to travel from the source to the detector. Thus, TOF instruments have virtually unlimited mass range. All the ions are given the same kinetic energy and allowed to travel through a field-free region of specified length. Since the ions have different masses, they separate into groups based on their velocity. Heavier ions reach the detector later than those of lower mass ions, because heavier ions have a lower velocity. The  $m/z$  value of an ion is determined by its time of arrival at the detector.

Limited mass resolution has always presented a problem in conventional TOF mass spectrometry. There is a spread in flight times due to (i) difference in kinetic energies of the

ions as formed in the source; (ii) different starting positions of the ions, and (iii) ions moving in opposite directions before being pulsed out of the source (44). Several methods were introduced to improve mass resolution in TOF mass spectrometers (45). One of the solutions was using a V-shaped reflectron. In a reflectron/TOF (re/TOF) mass spectrometer, ions of the same m/z with different energy reach the detector together by travelling different distances through the reflectron. TOF mass spectrometers based on this design have achieved mass resolution as high as 100,000 (46), although resolution of less than 5000 is typical in most of the TOF instruments (46).

TOF detection is a pulsed technique which requires spatially and temporally well defined ion packets for mass analysis. Thus, ionization techniques such as PD (47), SIMS (48), LD (49) and MALDI (50) have been very successful with TOF mass spectrometry. In fact MALDI/TOF has shown sensitivity in the subfemtomole range (50b). With these techniques a well-defined start time can be established for the time of flight. However, the coupling of continuous beam techniques such as atmospheric pressure ionization (API) and ESI sources with TOF mass spectrometry has been more complicated. Methods such as beam deflection (51), orthogonal pulsed extraction (52) and quadrupole ion trap storage/reTOF (IT/retof) (53) have been used to convert the continuous ion beam into a well-defined pulsed beam. Results from coupling

an ESI source with IT/retOf have shown enhanced sensitivity and resolution ( $m/\Delta m = 3500$  at  $m/z$  1000).

#### Ion Trap

Another important advance in mass spectrometry over the last decade has been the development of the three-dimensional quadrupole as an analytical mass spectrometer. Origin of this technique can be traced back to experiments done in 1953 by Paul and Steinwedel (54). The mass spectrometer consists of three electrically isolated hyperbolic electrodes: top end cap, ring electrode and bottom end cap. The trap is extremely compact, usually 2.5" x 3" and can be operated on a bench-top. Ions are trapped by applying combined RF and DC electric fields between the electrodes. An ion of a given  $m/z$  will be trapped and stored if its stability parameters satisfy the Matieu equation (55). Usually the ion detection is performed by ramping the RF amplitude applied to the ring electrode. This is referred to as the mass-selective instability mode of ion detection (56a). As the ring RF voltage is ramped, trajectories of ions become unstable (sequentially in increasing  $m/z$ ) in the axial direction. The ions are ejected sequentially from the trap and detected by an electron multiplier. The ion trapping mechanism and different modes of operation of ITMS have been explained in detail (56b). The mass selective instability mode of operation (56a) and the use of helium buffer or "bath" gas (typically operated with  $1 \times 10^{-3}$

Torr of background gas) for increasing trapping efficiencies of externally formed ions (56c) contributed to the advancement of ion trap mass spectrometry (ITMS).

Ionization techniques such as LD (56a), MALDI (56b) and ESI (56c-56e) has been successfully coupled with ITMS. Coupling external sources with an ion trap and its limitations have been discussed in detail (57). Coupling high pressure sources with ion traps benefits from its ability to (i) function under high pressure conditions (1 mTorr) (55c); and (ii) perform multiple MS/MS (58). ITMS is limited to several classes of biological samples due to its lower upper mass limit. The maximum  $m/z$  which can be detected in the normal operating mode is determined from the maximum amplitude of the RF voltage which can be applied to the ring electrode (7500 V<sub>o-p</sub>). The commercial ion traps have mass range up to 650 amu and resolution less than 2000 at this mass range. Several research groups are actively involved in improving the upper mass range and the resolution. Although a high mass limit of 45,000 (59) and resolution > 100,000 (60) have been demonstrated, they were under impractical conditions for routine experiments.

#### Quadrupole

During the past two decades, by far the most popular mass spectrometer has been the quadrupole mass analyzer. It was

developed in theory by Paul, who shared the Nobel prize for Physics in 1989. The quadrupole mass spectrometer consists of four parallel rods arranged in a diamond shape. Ideally these four rods should have the shape of hyperbola but in practice they are usually cylindrical. These rods are usually 20-30 cm long and the opposite rods are connected together electrically and to direct current (DC) and radio frequency (RF) supplies. Combined RF and DC fields voltages to the rods cause the region between the rods to act as a mass filter. The absolute values of RF and DC components determine the mass transmitted by the filter. Ions with stable trajectories are transmitted by the filter, whereas the ions with unstable trajectories are ejected by collisions with quadrupole rods. Simplicity of operation, low cost and ease of coupling with desorption techniques (high tolerance for poor vacuum, usually  $10^{-4}$  -  $10^{-5}$  Torr) attracted many researchers to quadrupole mass spectrometers for studying high molecular weight samples. Several groups have coupled ESI source with single quadrupole mass spectrometers (61). The performance of single quadrupole instruments is limited due to their inability to do MS/MS experiments after mass selecting a parent ion. To circumvent this problem, a triple quadrupole mass spectrometer was built in 1978 by Yost and Enke (62). In a triple quadrupole, the first and third quadrupoles are operated in the normal mode with a combination of rf and dc voltages. The center quadrupole is operated in the rf-only mode and

functions as a reaction region. The availability of unit resolution MS/MS product ion spectra was the strong driving force for coupling ESI with triple quadrupole mass spectrometers in several laboratories (63). Limitations of quadrupole instruments are their low resolution (unit resolution), slow scan rates (1000 Da/s) limited upper mass range (500-2000 Da) and absence of multichannel detection. An upper mass limit of 70,000 has been demonstrated for a quadrupole mass spectrometer (64). The mass resolution in a quadrupole instrument is a function of DC/RF voltage ratio (65). When the ratio is optimized for maximum resolution, fewer and fewer ions become stable in the quadrupoles and this lowers the sensitivity. The unit resolution commonly available with quadrupoles limits their utility for accurate mass measurements and elemental composition calculations.

#### Magnetic Sector

The most common type of sector mass spectrometer used is the two-sector instrument, composed of a wedge shaped magnetic sector ( $B$ ) (for ion momentum analysis) and a concentric pair of electrically biased plates, known as the electric sector ( $E$ ) (for ion kinetic energy analysis) (67). Both BE and EB configurations have been employed: the BE configuration is usually used to study kinetic energy release associated with the dissociation of mass selected ions and the EB

configuration is used in experiments where high resolution is required. Three- and four-sector instruments have been developed with a variety of combinations of electric and magnetic fields (66) to perform MS/MS experiments and to obtain high resolution spectra of daughter ions.

Larsen et al. (68) coupled an ESI source with a magnetic sector and demonstrated that carbonic anhydrase (MW of 29,000) and ovalbumin (MW of 45,000) could be detected with resolution in excess of 10,000. Fabris et al. (68b) coupled an ESI source with a four-sector instrument (EBEB configuration) to exploit the higher mass resolution and higher mass accuracy and study some polypeptides. Cody et al. (69) followed Larsen's demonstration and reported a mass spectrum of leucine enkephalin ( $[M+H]^+$ ) with 5000 resolution and 4.0 ppm mass accuracy. To obtain this high resolution spectrum the magnet was scanned over the mass range 450-650 Da in 25 s, with a 5 s dead time between scans. Increasing the scan speed caused the magnetic field to change rapidly and causing the ion beam to be distorted. This resulted in losses in both resolution and sensitivity (70). The highest mass range reported for a sector instrument is about 12,000 Da. (68). Another disadvantage of sector instruments is their operation with acceleration voltages in KeV range as opposed to quadrupoles which operate in the 2-15 eV range. With this higher energy charge stripping competes with collision induced dissociation and complicates MS/MS experiments (70).

Fourier Transform Ion Cyclotron Resonance

Fourier transform ion cyclotron resonance (FTICR) mass spectrometry is rapidly advancing as a viable analytical tool with unique potential for structural characterization. In FTICR ions are trapped in a cell by a combination of electric and magnetic fields. When alternating electric fields with frequencies corresponding to their characteristic cyclotron frequencies are applied to these ions, they will absorb energy and circulate in phase with one another. As the ions cyclotron in the cell, they induce an image current corresponding to their cyclotron frequencies on the cell plates. This current can be detected and an ion's  $m/z$  can be determined from its frequency. Unlike ion traps, where ions are ejected from the trap for detection, in FTICR the same ion cloud can be relaxed and remeasured several times (71). The ability of FTICR to trap ions for long times makes it a suitable instrument for ion/molecule and photodissociation studies (72). Unlike the beam instruments where the ion formation, excitation, analyzing and detection regions are separated in space, in FTICR analysis excitation and detection are separated in time.

Some of the features that enhance the utility of FTICR as an analytical tool include ultrahigh mass resolution (73), sequential MS/MS (74), high resolution mass analysis of MS/MS products (75) and the ability to perform collision-induced dissociation (CID) (76) as well as photodissociation (77).

The requirement of lower pressure ( $< 10^{-7}$  Torr) in the FTICR cell region delayed successful coupling of high resolution FTICR with high pressure ionization sources. To satisfy the low pressure requirements four approaches were exploited (i) using an ionization method which does not produce a high flux of neutral species--such as LD (78) and Cs<sup>+</sup> desorption (79); (ii) using a two section trapped ion cell (80)--producing the ions in the high pressure region and transferring the ions through a conductance limit into the analyzer region; (iii) external formation of ions--ions are formed almost 1 meter away from the cell and transferred through a differentially pumped system using quadrupole rods (81-82) or electrostatic lenses (83-84); and (iv) using several concentric vacuum chambers which are differentially pumped and transferring ions with assistance from the high magnetic field of the FTICR instrument (85-87).

These four methods allowed the pressure barrier to be overcome and ionization techniques such as LD (88), SI (89), PD (90), FAB (91), MALDI (92) and ESI (85-87) to be coupled with FTICR mass spectrometry. As a result, coupling ESI with FTICR now allows thermally labile, high molecular weight samples, which are stable in solution, to be analyzed using the high mass resolution and high mass accuracy capabilities of FTICR mass spectrometry.

In 1989, McLafferty et al. (93-96) coupled an ESI source with a FTICR mass spectrometer and demonstrated that molecular masses up to 29,000 Da could be introduced into gas phase. Capabilities such as high mass resolution, tandem mass spectrometry and photodissociation were performed on these electrosprayed ions. This instrument was based on an external source design, where the ESI source is placed outside the magnetic field and ions are guided into the cell with quadrupole rods. The major drawback of their external source ESI/FTICR configuration was the inefficient transfer of ions from the source to the cell.

In 1991, Laude et al. (85-87) overcame some of the problems encountered by McLafferty et al. (93-96) by positioning the ESI source 25 cm from the cell and using the FTICR high magnetic field to guide ions into the cell. Positioning the atmospheric pressure ESI source closer to cell required the use of five concentric vacuum chambers of increasing diameter for achieving the required lower pressure for FTICR excitation and detection. Laude's group reported the detection of bovine albumin, molecular weight of 132,532 Da. However, their design was limited due to the presence of higher pressures in the FTICR cell (source and analyzer regions limited to low  $10^{-5}$  Torr and mid  $10^{-7}$  Torr, respectively).

Scope of the Dissertation

Chapter 1 has provided a summary of different types of ionization techniques and mass spectrometric methods. In addition, the purpose and history behind the development of ESI/MS has been outlined. The focus of this dissertation is ESI/FTICR mass spectrometry.

In Chapter 2 of this dissertation, the fundamental theory of FTICR is described. The ion formation process in the ESI source involves formation of: (1) small highly charged droplets and (2) gas phase ions from charged droplets. In addition, the method of ion transfer from atmospheric pressure to low pressure regions is discussed. Both internal and external ESI source FTICR mass spectrometers and their operating conditions are explained. Also, the setup and the instrumentation for laser desorption experiments presented in Chapter 6 is explained.

In Chapter 3 the design and the construction of the internal ESI/FTICR mass spectrometer at the University of Florida is presented. Several problems were encountered during this endeavor (i) inability of the ESI source material to withstand the required heating of the desolvating capillary; (ii) alignment of each component with respect to the cell and the magnetic field; (iii) focusing the ions exiting the capillary; and (iv) inability of this design to

attain required low pressures for FTICR excitation and detection events. Steps taken to circumvent these problems are presented along with optimum parameters required to obtain the best performance of the internal source ESI/FTICR mass spectrometer.

Electrospray ionization FTICR mass spectrometry benefits from the ability to perform CID experiments in the capillary/skimmer region and/or in the FTICR analyzer cell. The potential difference between the skimmer and the capillary causes the ions exiting the capillary to undergo energetic collisions with gases present in the capillary/skimmer region. At lower values of the potential difference intact molecular ions are observed. At higher values, the molecular ions can be dissociated to give structurally informative fragment ions (88). Application of capillary/skimmer CID to organometallic complexes such as Ru(bpy)<sub>3</sub>(PF<sub>6</sub>)<sub>2</sub>, Ru(phen)<sub>3</sub>(PF<sub>6</sub>)<sub>2</sub> and Ru(Pz)(NH<sub>3</sub>)<sub>5</sub>(PF<sub>6</sub>)<sub>2</sub> is presented in Chapter 4. The application of this source was extended to proteins and organic dyes by studying cytochrome c and Rhodamine 6G ions.

Since the initial ESI/FTICR demonstration by McLafferty et al.(93), several other possibilities were explored by the FTICR community for coupling ESI sources externally with FTICR mass spectrometers (98-99). One such attempt was coupling an ESI source externally and using electrostatic lenses instead of quadrupoles to guide the ions into the analyzer cell. The

concept of using electrostatic lenses to guide the ions is not new to FTICR mass spectrometry. Ions produced using techniques such as FAB, LD and MALDI have been successfully transferred using electrostatic lenses (100). In Chapter 5, ions produced using an external ESI source are studied. Specifically, ESI/FTICR mass spectrometry was used to study the complexes  $\text{Ru}(\text{bpy})_3(\text{PF}_6)_2$ ,  $\text{Ag}_2(\text{DPM})_2(\text{BF}_4)_2$  and  $\text{Ag}_2(\text{DPM})_2(\text{BF}_4)_2$ . Both capillary/skimmer and in-cell CID were used to obtain structural information for these complexes.

In Chapter 6, studies of ions formed by laser desorption/ionization are presented. The ability of the FTICR mass spectrometer to trap ions for long times makes it an excellent instrument for studying ion/molecule reactions. Ion/molecule reactions between carbon cluster anions and neutral reference compounds with known electron affinities (EA) were carried out to bracket the EA's of carbon clusters. EA's of  $\text{C}_4 - \text{C}_9$  are reported and the results are compared with existing theoretical and experimental values.

Finally, in Chapter 7, conclusions from internal and external source ESI/FTICR mass spectrometry are presented along with electron affinities of small carbon clusters determined by LD/FTICR mass spectrometry.

CHAPTER 2  
THEORY AND INSTRUMENTATION

FTICR Mass Spectrometry

Historical Evaluation

Progress in the field of FTICR mass spectrometry has been documented in several review articles (101-103). In addition, a historical perspective on how FTICR reached its present state has been described in a book chapter by Dunbar (104). Briefly, the fundamental basis for ion cyclotron resonance mass spectrometry was established by Lawrence in the 1930s when he demonstrated that ions could be accelerated to higher energy by using an electric field having the same frequency as the ions' cyclotron frequency (105). However, the first practical ion cyclotron resonance mass spectrometer, the Omegatron, was developed in 1950 by Sommer et al. (106). This was followed by the development of a resonance detection ICR instrument by Wobschall et al. (107). Wobschall's instrument was used primarily for studying ion-molecule reactions. Development of pulsed ICR with a trapped ion cell by McIver in 1970 (108) and Fourier transform ion cyclotron resonance (FTICR) mass spectrometry by Comisarow and Marshall in 1974 (109) improved the capabilities of ICR as an analytical tool.

The coupling of FT with ICR mass spectrometry improved the sensitivity of the method and allowed a complete mass spectrum to be acquired in a few tenths of a second. Commercialization of FTICR mass spectrometers in 1981 further helped the technique to advance rapidly.

The next two decades were spent in (i) modifying vacuum systems for adapting to different high pressure ionization methods; (ii) improving mass resolution and mass accuracy capabilities by using higher magnetic fields (aided by the availability of superconducting magnets); (iii) modifying FTICR analyzer cell geometries for improved trapping capabilities (higher mass ions); and (iv) improving the speed of the technique by using faster computers.

#### **Ion Formation and Trapping**

The basic theory of FTICR mass spectrometry has been explained in several papers (110-111) and books (112-113). In FTICR mass spectrometry, ions are first produced in or transferred into an analyzer cell. Ion formation methods have been explained in Chapter 1 of this dissertation. These ions are trapped in the analyzer cell, which is located in a high vacuum chamber most often within the solenoid of a superconducting magnet. In a magnetic field,  $B$ , ions moving parallel to the magnetic field are not deflected and ions moving perpendicular to the magnetic field are deflected into

circular motion. For ions to move in a stable circular orbit, the centrifugal force exerted outward should be balanced by the magnetic or Lorentz force experienced inward. The magnetic force inward can be expressed by equation 2.1

$$\text{Magnetic Force} = qvB \quad (2.1)$$

and the centrifugal force outward by equation 2.2.

$$\text{Centrifugal Force} = mv^2/r \quad (2.2)$$

where  $q$  is the charge,  $m$  is the mass,  $v$  is the velocity, and  $r$  is the radius of orbit of the ion. In the absence of collisions the cyclotron motion of the ion will be a stable circular orbit. This motion is stable due to the balance of the two forces exerted on the ion, magnetic and centrifugal. If the forces are equated, equation 2.3 is obtained.

$$qvB = mv^2/r \quad (2.3)$$

Cancelling a  $v$  from both sides and rearranging gives equation 2.4.

$$qB/m = v/r = \omega_c \quad (2.4)$$

Where  $\omega_c$  is cyclotron frequency and  $\omega_c = 2\pi f_c$ . Equation (2.4) can be rearranged to give Equation 2.5.

$$f_C = qB/2\pi m \quad (2.5)$$

Usually cyclotron frequencies are expressed in units of Hertz (Hz), with  $q = 1.6022 \times 10^{-19}$  C,  $B$  in the range of 1-7 Tesla and  $m$  is given in kg ( $1.6605 \times 10^{-27}$  kg is 1 Da). The magnetic force prevents an ion from escaping outward (x and y axes) in the plane perpendicular to the axis of the magnetic field. However, ions are still free to drift along the magnetic field axis (z-axis). Therefore, two plates are positioned perpendicular to the magnetic field and a DC potential (usually  $\pm 1-2$  V) is applied to prevent the ions from escaping along the z-axis. In addition to the pair of trap plates, a pair of excite and a pair of detect plates make up the FTICR analyzer cell.

Application of an electric field to prevent the ions from escaping along the z-axis creates two other types of ion motion beside the cyclotron motion ( $\omega_c$ ). The first one is due to ions approaching the trap plates along the z-axis and turning around and going back toward the center of the cell. This oscillating motion between the trapping plates, which is parallel to the magnetic field, is termed the "trapping" motion. This motion has been shown to depend on the cell geometry (114).

The second trapping induced motion is called the "magnetron" motion. This motion is actually due to a combination of trapping and cyclotron motions. This leads the

center of the cyclotron orbit along a wider path which follows the electric equipotential surface within the FTICR cell. Both the trapping and the magnetron motions are much slower than the cyclotron motion. Thus, they are usually ignored in the simplest description of the ICR processes. However, when a higher trapping voltage is used the cyclotron frequency of an ion is observed to shift downward. Thus, the m/z obtained using that cyclotron frequency will be shifted to a lower value from that of the actual m/z. In addition to the electric field produced by the trapping plates, an electric field produced by the space charge of the ion cloud, collisional damping and magnetic field inhomogeneity all shift the observed cyclotron frequency from the "actual" cyclotron frequency described by Equation 2.4.

#### Ion Excitation

After the ions are introduced into or produced in the analyzer cell, the next step is exciting them. The trapped ions are accelerated into larger cyclotron orbits by applying an external rf pulse. Usually, the rf pulse is applied to the ions through a pair of opposite plates which are termed the "excite" or "transmitter" plates. The ions are accelerated steadily provided that the applied rf frequency is same as the ion's natural cyclotron frequency. This also drives the ions into distinct ion packets and results in coherent cyclotron

motion. Under ideal conditions, ions in the mass spectral range of interest are excited to the same cyclotron orbital radius and detected without any mass discrimination.

Several different methods have been used to excite ions in a FTICR analyzer cell. Single-frequency excitation was the method used in obtaining the initial FTICR mass spectrum by Comisarow and Marshall (115). However, the amplitude profile of this frequency-domain excitation spectrum is flat only over a narrow frequency range. This method of ion excitation has been shown to be ineffective for exciting a broad range of cyclotron frequencies. According to Marshall and Roe's calculations, it would have required a 13 kV rf-burst lasting 30 nS to excite ions over a 2-MHz band width (116). Thus, this method was impractical for a broad range of frequencies. However, the method is still used in narrow band FTICR experiments to detect ions with cyclotron frequencies which are within a few kilohertz bandwidth.

Since it was impractical to use a single frequency excitation in the broadband mode, Comisarow and Marshall (117) suggested the use of a weaker power but longer duration fast frequency sweep, or "rf chirp", for accelerating the ions which are trapped in the analyzer cell. The chirp excitation signal is generated by a digitally controlled frequency synthesizer, which is usually scanned from 20 kHz to 2.66 MHz (corresponding to 17-2300 Da for 2 Tesla field) in a duration of about 1 ms. Usually, this rf chirp is applied

differentially to two opposed transmitter (excite) plates of the FTICR cell to produce an oscillating electric field perpendicular to the magnetic field. As the frequency applied approaches the cyclotron frequency of an ion, the ion absorbs energy and accelerates into an orbit of larger radius.

Chirp excitation is still the standard method of ion excitation in FTICR mass spectrometry and it was used in all the experiments described in this dissertation. One of the limitations of chirp ion excitation is its nonuniform power spectrum. Time-domain excitation waveforms of a chirp and its frequency-domain magnitude mode spectrum have been explained in several papers (116). These studies showed that even if the amplitude of the chirp signal is constant as the frequency is scanned, the ions at the edges of the time-domain excitation waveform do not receive the same excitation power as the ions in the middle of the excitation waveform. This leads to mass discrimination during the FTICR detection event. In addition, Kofel et al. (118) have shown that the z-component of the chirp excite electric field can accelerate the ions in the trapping well and cause the ions to be ejected along the z-axis. This can lead to inaccuracies in relative peak height measurements and limit the application of FTICR mass spectrometry in measurements of isotope ratios and ion-molecule reaction rate constants.

To overcome the second problem Marshall et al. (119) and Russell et al. (120) added several "guard wires" with voltage-

divided rf amplitude to allow the rf electric field to be "shimmed" to near perfect rf field within the FTICR cell. This arrangement virtually eliminated the z-axis ejections and reduced the cyclotron frequency shifts caused by the trapping potential.

To overcome the nonuniform power problem associated with rf chirps alternative excitation methods have been developed. Pseudorandom (121) and random (122) noise were used to excite the ions in the broadband mode. However, resulting power spectra were more nonuniform than the rf chirp power spectrum.

A promising new approach termed Stored Waveform Inverse Fourier Transform (SWIFT) was introduced in 1985 by Marshall et al. (123). This excitation method allowed virtually any desired excitation frequency profile to be applied to the analyzer cell. SWIFT or tailored excitation involves first specifying the desired frequency profile and assigning it as a frequency domain spectrum. This can be a square shape covering the frequency of interest, or it can cover different regions with different amplitudes. Next, an inverse Fourier transform is performed to generate the equivalent time-domain excitation waveform. This time-domain signal is then converted to an analog signal, amplified, and applied to the plates of the analyzer cell. The general types of excitation accomplished by SWIFT include flat power (more accurate peak heights for isotope ratios), flat power with windows (eject all the ions and keep an ion of interest to do further

studies), and flat power at selected m/z ratios (excite the ions of interest only, or eject several selected ions, or excite the most abundant ions with higher amplitude, thus ejecting them, and excite the less abundant ions with lower amplitude, thus detecting them).

In addition, Marshall has shown that by using SWIFT ions with 23 different masses can be ejected in 17 ms. To accomplish 23 ejects with rf chirps would take at least 10 ms for each eject and a 3 ms delay between ejects. The total time would be more than 300 ms. During this 300 ms, the ions could undergo ion-molecule reactions, possibly leading to additional peaks in the mass spectrum. These studies undoubtedly show that SWIFT is the excitation method of choice for FTICR mass spectrometry (124).

Recently, McIver, et al. (125) introduced another ion excitation method for FTICR mass spectrometry and called it "impulse excitation." This method involves abrupt and simultaneous excitation of all the ions in the cell. Excitation is achieved by a high dc voltage (usually > 1000 V) which lasts for less than a microsecond. This method does not require the ions to be in resonance when excited. Details of the method have been discussed by McIver et al. (126). An advantage of impulse excitation is its simplicity compared to rf chirp and SWIFT excitations. Impulse excitation does not require a computer-controlled frequency synthesizer. As a result, one of the limitations of the method is its inability

to perform double resonance ejections without additional electronics.

In addition to different ion excitation methods, several excitation geometries for FTICR mass spectrometry have been used. These include radial dipolar (127), quadrature (128), axial dipolar (129), parametric (130), radial quadrupolar (xy) (131) and quadrupolar (xz) (132) geometries.

The standard excitation geometry used in almost all the FTICR experiments has been radial dipolar. Excitation voltages of opposite phase are applied to two opposed plates and two other opposed plates are used for image current detection. This geometry was used in all the experiments presented in this dissertation. These excitation geometries have been compared by Schweikhard and Marshall (133) in great detail. Both xy and xz quadrupolar excitation modes have been shown to be promising by Marshall et al. (134) for dual cells and Amster et. al (135) for single region cells. The xy mode of quadrupolar excitation involves interconversion of ion magnetron and cyclotron motion. This is achieved by applying one phase of the excitation signal to the pair of plates that function as the excite (transmitter) plates in the normal dipolar mode and the opposite phase with equal amplitude to the detect (receive) plates. Higher mass resolution and increased sensitivity were demonstrated by both Marshall et al. and Amster et al. The xz mode of quadrupolar excitation was performed by applying an excitation voltage of opposite

phase equally to both segmented trap plates and segmented side electrodes. This mode allowed the coupling of trapping (axial) motion to cyclotron and magnetron (radial) ion motions.

#### Ion Detection

Ion detection follows ion excitation. To obtain a spectrum without any mass discrimination, all ions should be accelerated to the same cyclotron radius. The cyclotron orbital radius can be expressed using equation (2.6).

$$r_c = Et/2B \quad (2.6)$$

where  $E$  is excitation electric field,  $t$  is the duration of the excitation pulse, and  $B$  is the magnetic field. As the ion circulates in its cyclotron orbit, an image current is induced in the upper detect plate when the ion is closer to the upper plate. Similarly, when it is closer to lower detect plate, an image current is induced in the lower plate. The result is an alternating image current corresponding to the cyclotron frequency of the ion. As shown in Equation 2.7, the image current ( $I$ ) is dependent on the number of ions ( $N$ ), the distance between the electrodes ( $d$ ), the charge on the ion ( $q$ ) and the velocity ( $v$ ) of the ion (136).

$$I = Nqv/d \quad (2.7)$$

Different detection methods have been used with ICR experiments. These detectors include marginal oscillators (137), capacitance bridge detectors (138), Q meters (139) and electrometers (136). These methods have been compared by Kemper and Bowers (136).

Usually, the oscillating image current induced on the detect plates is passed through an impedance and converted to an oscillating voltage and then amplified and digitized to give a 'time-domain' signal. The time-domain signal contains periodic signals due to the characteristic cyclotron frequencies of the various ions, each with an amplitude proportional to the number of ions of different types in the cell. The resulting time-domain signal (transient) is amplified and digitized. Such a time-domain signal, obtained using the internal electrospray source (chapters 1 and 3) for  $\text{Ru}(\text{bpy})_3(\text{PF}_6)_2$  (where bpy is 2,2'-bipyridyl), is shown in Figure 2.1. This transient is due to isolated  $[\text{Ru}(\text{bpy})_3]^{2+}$ . The decay in signal is mainly caused by the loss of coherent motion of the ions in the cell due to ion-molecule reactions. Another contribution to the decay of the transient is the loss of ions from the cell. This transient was acquired at a pressure of  $3.5 \times 10^{-8}$  Torr. If the pressure were maintained

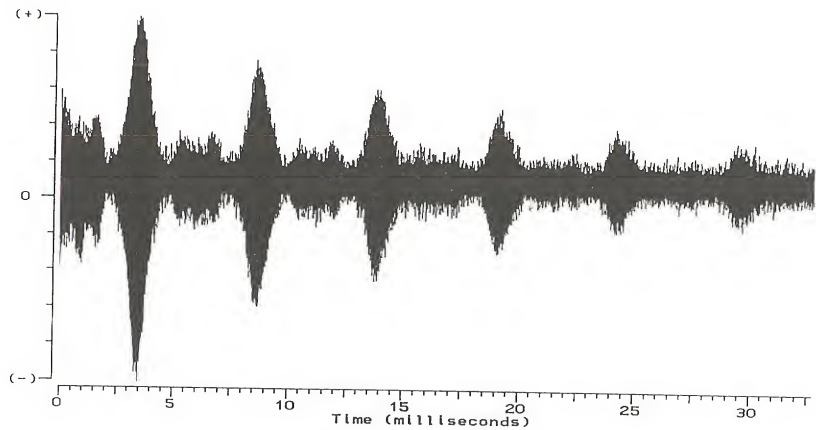
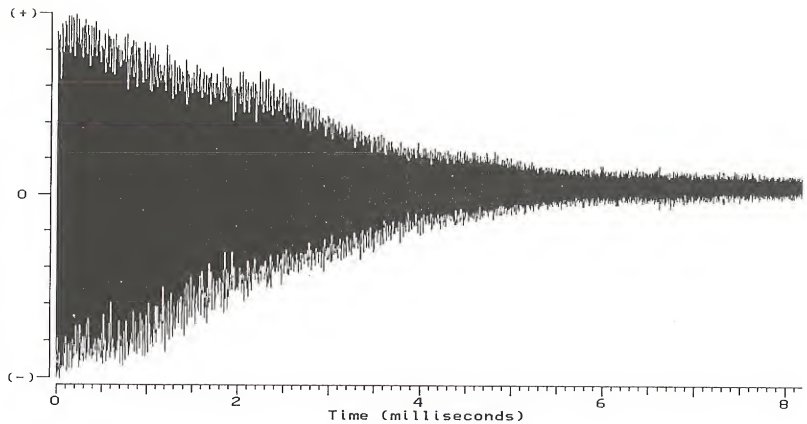


Figure 2.1      Digitized time domain signal due to  $[\text{Ru}(\text{bpy})_3]^{2+}$  produced by the internal source ESI/FTICR mass spectrometer ( $1 \times 10^{-5}$  M  $[\text{Ru}(\text{bpy})_3](\text{PF}_6)_2$  in 49/49/2 methanol/water/acetonitrile solution).

at less than  $3.5 \times 10^{-8}$  Torr, the frequency of ion-molecule collisions would be reduced and the coherent ion motion would last longer. The time domain-signal obtained following CO<sub>2</sub> laser desorption of a graphite plug is shown in Figure 2.2. This transient is due to the presence of C<sub>4</sub><sup>-</sup> - C<sub>10</sub><sup>-</sup> in the FTICR cell. Comparison of these transients indicates that the signal obtained with ESI of [Ru(bpy)<sub>3</sub>]<sup>2+</sup> has equally spaced "beats". The beat patterns in ESI/FTICR mass spectrometry have been studied in detail by Smith et al. (140). This type of beat pattern is usually observed when there are closely spaced isotopic ions in the FTICR cell. The time domain signal between these beats does not provide any frequency domain information (140). Since the isotopic ions are closely spaced in cyclotron frequencies no net signal is produced on the differentially amplified detection electrodes. Smith's group called this pattern an "isotopic beat". In addition, their study revealed that a minimum of two beats are required to mass resolve isotopic peaks present within a charge state.

The Fast Fourier Transform (FFT) algorithm then converts these time-domain signals into a frequency-domain spectrum. This frequency-domain spectrum is then converted to a m/z spectrum via Equation (2.4) (if the magnetic field strength is known or can be obtained by calibration). Mass spectra obtained using the time-domain signals shown in Figures 2.1 and 2.2 are shown in Figures 2.3 and 2.4, respectively.



38

Figure 2.2      Digitized time domain signal due to  $C_2^- - C_{10}^-$  produced by laser desorption from a graphite plug.

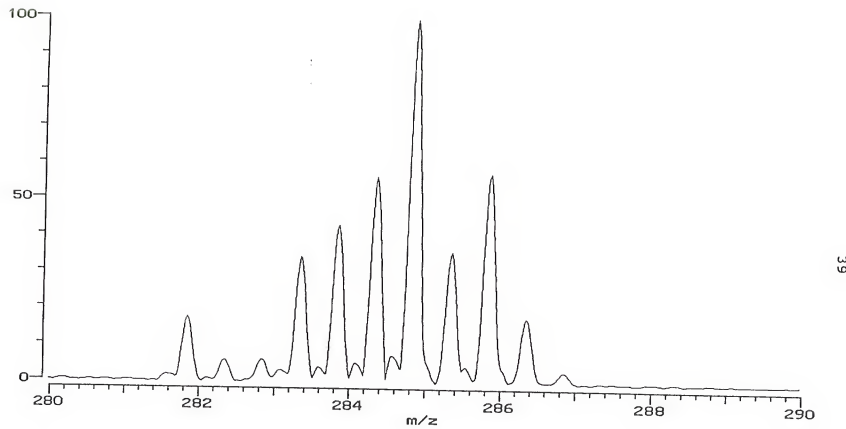


Figure 2.3 Mass spectrum of  $[\text{Ru}(\text{bpy})_3]^{2+}$  resulting from Fourier transformation of the transient observed in Figure 2.1.

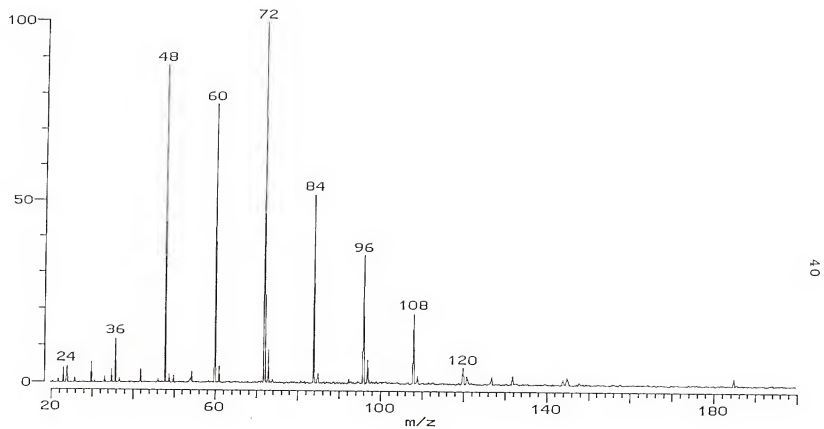


Figure 2.4 Mass spectrum of  $C_2^- - C_{10}^-$  resulting from Fourier transformation of the transient observed in Figure 2.2.

FTICR Analyzer Cell

The heart of a FTICR mass spectrometer is the trapped ion cell, situated in a homogeneous magnetic field (usually produced by a superconducting magnet). Requirements for a FTICR cell are the ability to (i) trap ions formed or transferred from an ion source; (ii) accelerate the ions to a larger orbit by allowing them to absorb energy when the ions are in resonance with the applied oscillating electric field; and (iii) detect the image currents of the circulating ions. Usually, these functions of the cell are carried out using three separate pairs of electrodes. Since FTICR events are separated by time, using more than one pair of electrodes is not a restriction. In fact, in the quadrupolar excitation mode both the excitation and the detection pair of electrodes are used for ion excitation. The first FTICR experiment by Comisarow and Marshall was performed using a cubic trap geometry (9). Following this, other trap geometries were explored to reduce undesirable effects experienced with the cubic trap geometry. These effects include shifting of the observed frequency as a function of the trapping voltage, space-charge effects, a limited upper mass range, and z-axis ejection of ions. The ion trap configurations demonstrated for FTICR mass spectrometry over the past few years include: cubic (141), orthorhombic (142), tetragonal (143), cylindrical

(144), hyperbolic (145), open orthorhombic (146), open cylindrical (147), multi segmented (148), "Infinity" (149) and off-center dual cell (150).

In addition to optimizing the cell geometry for reducing trapping field effects, Marshall et al. (151) have shown that placing a grounded screen in front of both trap plates of an orthorhombic cell minimizes cyclotron frequency shifts and increases the upper mass limit for FTICR mass spectrometry. All the trap geometries exhibit an approximately quadrupolar trapping potential near the center of the cell. When a 1 V trapping potential is applied to the plates, the magnitude of the field line extending to the center of the trap is ca. 0.3 V. Adding grounded screen in front of the trapping plates reduces the magnitude of the field line by a factor of ca. 15-20 (151). Thus, the shift in cyclotron frequency is reduced. Ion cyclotron frequency shifts due to applied trapping voltage for a 1 in. cubic cell, 2 in. z-axis elongated cell and 2 in. elongated cell with grounded screen plates were 227 Hz/V, 69 Hz/V and 0.67 Hz/V, respectively (151).

Both Russell et al. (152) and Marshall et al. (153) independently introduced rf shimming for FTICR analyzer cells. Shimming produced a uniform rf field in the volume within the trap and provided even excitation to the ions regardless of their initial location. In addition, it reduced z-axis excitation and ejection.

Mass Resolution

The high mass resolution capabilities of FTICR mass spectrometry have been identified as one of the significant advantages of the technique over other mass spectrometric methods. Mass resolution is important for exact mass measurements, as an aid in structural identification and for trace analysis. Since different mass spectrometers produce different mass spectral peak shapes (e.g., Lorentzian, Gaussian) it is difficult to define resolution. Resolution is usually expressed using one of three methods: (i) peak width; (ii) ratio of peak position ( $m$ ) to peak width ( $\Delta m$ ) for an isolated peak; or (iii) ratio of peak height to the minimum separation between two equally intense peaks (valley can be 1%, 10%, 50%, or 100%). In FTICR experiments the mass resolution is usually defined as the full width at half height (FWHH) or maximum (FWHM). Resolution in FTICR can be defined using equation 2.8 (154).

$$m/\Delta m = qBt/m \quad (2.8)$$

As shown in Equation (2.8), mass resolution,  $m/\Delta m$ , is directly proportional to time domain signal decay,  $t$ , and magnetic field,  $B$ . Thus, the resolution depends on the amount of time the coherent cyclotron motion of a packet of ions can be observed. The ion packet loses its coherent motion due to:

inhomogeneous electric and magnetic fields and from ion/molecule collisions with background molecules.

#### Mass Accuracy

Exact mass measurement in mass spectrometry is required for accurate and unambiguous determination of ion elemental composition. Mass accuracy can be expressed using Equation 2.9. Let actual mass = a and measured mass = b,

$$\text{Mass Accuracy (ppm)} = [(a - b)/a] \times 10^6 \quad (2.9)$$

Since FTICR mass spectrometry is based on measuring frequency, measurements with mass accuracies in the sub-ppm range are routine. Exact mass measurements involve detecting precise cyclotron resonance frequencies and relating the frequencies to mass accurately. Thus, the mathematical relationship (calibration formula) which is used to assign mass is very important for mass accuracy. The simplest calibration equation for the mass of an ion in absence of electric field is expressed in Equation (2.10) (which is a rearrangement of Equation 2.5).

$$m/z = B/2\pi f \quad (2.10)$$

Since  $B/2\pi$  is constant, Equation 2.10 can be written as

$$m/z = a/f \quad (2.11)$$

Since trapping potential is employed during calibration, the trapping potential effect has to be considered. This effect has been approximated by Ledford et al. (155) and a new calibration relationship formulated. This relationship is shown in Equation 2.12.

$$m/z = a/f + b/f^2 \quad (2.12)$$

Equation 2.12 is used in most FTICR calibrations. Other mass calibration formulas proposed for FTICR mass spectrometry have been discussed in detail (156). Usually, a known calibrant is used, mass/frequency pairs are fitted to the equation, and the constants *a* and *b* are determined. Then these constants are applied to unknown frequencies produced from samples. For calibration, if the mass limit is less than 1000 Da, perfluoro-N-tributylamine (PFTBA) is most often used as the calibrant. For all the experiments presented in this dissertation, PFTBA was used as the calibrant. Usually calibration is done once or twice a year. Since ion cyclotron frequencies shift with trapping voltage, calibration has to be performed using the same trap voltage as the experimental trap voltage. Usually, fragments peaks observed at  $m/z$  69, 119, 131, 219, 264, 414 and 502 are used in calibration. The fragmentation pattern depends on the experimental conditions

used. However, the fragmentation pattern is not crucial for calibration, but mass accuracy is. For higher mass detection, calibrants such as PEG-3350 (156), PPG-4000 (157) and  $(\text{CsI})_n \text{Cs}$  (158) have been used.

### Electrospray Ionization

#### Ion Formation Process

The phenomenon that the application of an intense electric field causes the dispersion of a liquid surface into a spray of charged droplets was explained by Bose (159) in 1745. Since then this phenomenon has been applied in paint spraying, electrostatic printing, electrostatic emulsifications, fuel atomization in combustion systems and in space vehicle propulsion systems.

When a liquid flows slowly through a capillary, if no electric field is applied, the liquid drips from the capillary at a critical volume depending on the surface tension. Applying an electric field reduces the critical volume for droplet detachment. Some of the parameters that affect the process of electrospray are (i) magnitude of the potential applied to the capillary (spray needle in this dissertation); (ii) geometry of the needle (i.d., o.d., and shape of the tip); (iii) solution flow rate; and (iv) solution physical properties such as electrical conductivity, viscosity, surface

tension and dielectric constant. These parameters can be varied in combination or independently to vary the size, mass-to-charge ratio, and velocity of the ejected droplets. These parameters have been discussed in detail by Pfeifer et al. (160) and Smith (161).

Influence of the applied voltage on the stability of the electrospray has been studied (162). As shown in Figure 2.5, electrospray occurs in air at atmospheric pressure. Usually, a potential of 3-5 kV,  $V_{needle}$ , is applied to the metal spray needle (capillary), which has a 0.150 mm i.d. and 0.4 mm o.d.. This spray needle is located 0.5 mm-3.0 cm from the counter electrode. The distance between the spray needle and the counter electrode varies from system to system and the  $V_{needle}$  depends on this separation. In electrospray mass spectrometry, the counter electrode has an orifice to allow ions to enter the mass spectrometer. The electric field produced at the spray needle,  $E_{needle}$ , can be expressed using Equation 2.13 (161).

$$E_{needle} = [2V_{needle}/r_{needle}] \ln[4d/r_{needle}] \quad (2.13)$$

where  $r_{needle}$  is the o.d./2 of the spray needle and  $d$  is the distance between the spray needle and the counter electrode. The counter electrode in our home built electrospray source is a 15 cm long and 0.585 mm i.d. stainless steel capillary. In the absence of solution, Equation 2.13 can be used to

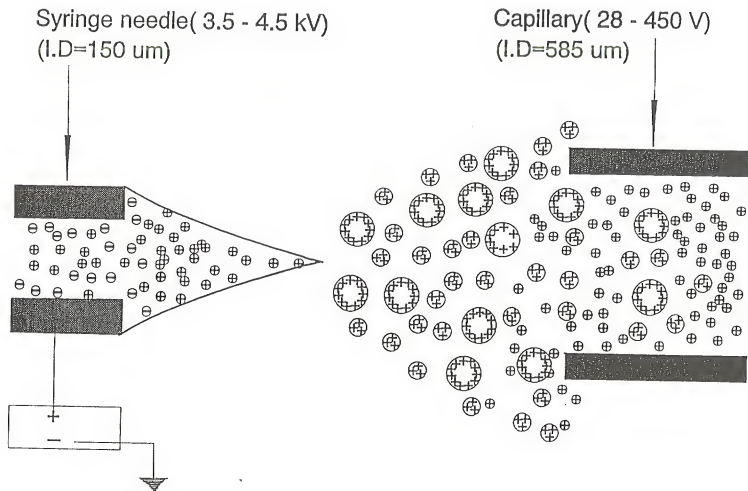


Figure 2.5 Ion formation process in electrospray.

calculate the electric field at the tip of the spray needle. For example, if we use  $d = 6$  mm,  $V_{needle} = 3.5$  kV and  $r_{needle} = 0.20$  mm in Equation 2.13, the  $E_{needle}$  is ca.  $10^6$  V/m.

In addition to providing a relationship for calculating the electric field at the needle tip, Smith (161) showed a formula for calculating the potential required for the operation of electrospray. This is given in Equation 2.14.

$$E_{onset} = [2\gamma \cos\theta_0 / \epsilon_0 r_n]^{1/2} \quad (2.14)$$

where  $\gamma$  is the surface tension of the liquid,  $\theta_0$  is the half-angle of the Taylor cone and  $r_n$  is the inner radius of the spray needle. Combining Equations 2.13 with 2.14 and substituting  $49.3^\circ$  (161) for the half-angle of the Taylor cone results in Equation 2.15 (where  $\epsilon_0 = 8.8 \times 10^{-12} \text{ J}^{-1}\text{C}^2\text{m}^{-1}$ ).

$$V_{on} = 2 \times 10^5 (\gamma r_n)^{1/2} \ln(4d/r_n) \quad (2.15)$$

Equation 2.15 can be used to approximate the voltage for electrospray onset (161). Electrospray onset voltages for several solvent systems have been investigated by Kebarle et al. (163). Their results showed  $V_{onset}$  to increase with increasing surface tension, in accordance with Equation 2.15. The surface tension of water and methanol is 0.073 and 0.023 Nm<sup>-2</sup>, respectively and the onset voltages found were 4.0 and 2.2 kV, respectively.

Charged Droplet Formation

The first step in electrospray ionization is formation of large charged droplets. When the spray needle is held at a positive potential, the positive ions will drift toward the liquid surface and the negative ions away from the liquid surface and toward the metal surface (Figure 2.5). The liquid surface becomes enriched with positive charges. Accumulation of positive charges makes the liquid surface become unstable and causes it to be drawn out from the needle tip. This leads to the formation of a liquid cone at the tip of needle. This cone, called a "Taylor cone", is named after its first observer (164).

When the Taylor cone becomes unstable due to the applied electric field, large droplets are ejected from the tip of the Taylor cone. These droplets usually have a diameter of few micrometers (163).

Gas Phase Ion Formation from Charged Droplets

The next step in electrospray ionization is ion separation from large charged droplets and conversion to gas phase ions. This process is not completely understood, but different models have been suggested. One such model was suggested by Iribarne and Thomson (165). They suggested the direct evaporation of single ions clustered with several

solvent molecules, which have radius less than 1 um and are near the Rayleigh limit. Another model was suggested by Rollgen (166). Rollgen's model suggested that the gas-phase ions are produced from solvent evaporation from very small droplets, ca. 1 nm in diameter, which contain only one ion.

Another model which has been observed by several researchers involves the ambient atmospheric air present near the spray needle. The large droplets ejected from the Taylor cone follow the electric potential toward the counter electrode. During their journey from the spray needle to the counter electrode, the ambient air provides continuous evaporation of the solvent molecules from large charged droplets. This process increases the charge to volume ratio of the droplets and makes the droplets electrohydrodynamically unstable. This happens at the Rayleigh (167) stability limit (coulomb repulsion exceeds surface tension). The unstable droplets disintegrate and daughter droplets are produced. The daughter droplets further disintegrate to produce grand-daughter droplets. This process is repeated until gas phase ions are produced (168).

#### Spray Needle Operated at High Voltage

Figure 2.6 is an illustration of the ESI source developed in our laboratory. Ionization takes place in a PEEK (polyether ether ketone) cavity (15 cm long and 1.73 cm od),

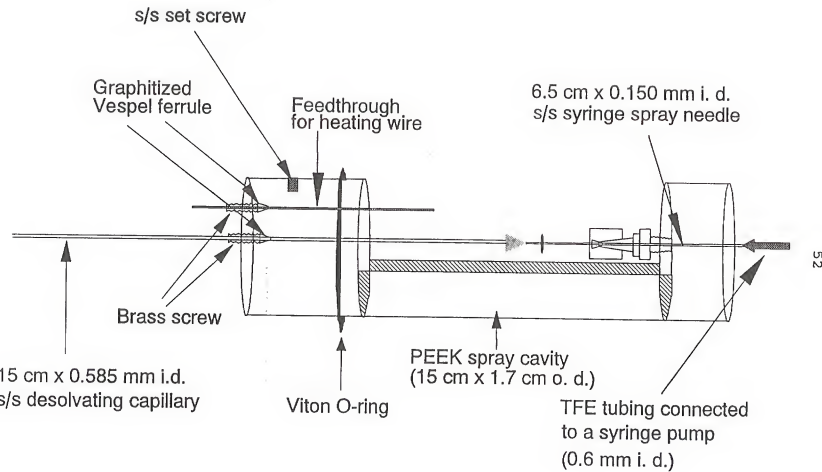


Figure 2.6 A schematic representation of the internal electrospray source used with the 2 T FTICR mass spectrometer.

which allows us to heat the capillary to a temperature >175 °C without softening or melting the spray assembly. It contains a 6.5 cm long (0.15 mm i.d. and 0.25 mm o.d.) dome tipped stainless steel spray needle and a 15 cm long (0.585 mm i.d. and 0.780 mm o.d.) desolvating capillary held 6 mm apart. The ESI source is inserted inside a 1.9 cm stainless steel probe and a vacuum seal is made with a Viton O-ring. When the probe is inserted into the strong magnetic field, the electrospray ionization process occurs 24 cm from the FTICR cell.

Large droplets produced from the spray needle further disintegrate to smaller droplets on their way from the spray needle to the capillary. The resistive heating of the capillary assists in desolvating the large droplets. Subsequently gas phase ions are produced at the end of the capillary. When the spray assembly is inserted into the 1.9 cm stainless steel probe the desolvating capillary protrudes 2 cm from the end of the probe. When the source is operational, the desolvating capillary is positioned 5 - 10 mm from a 0.2 mm orifice skimmer. Then a combination of magnetic and electric fields is used to focus and direct the ions through two conductance limits into the analyzer cell. The ESI source used in these experiments is presented with more detail in Chapters 3 and 4.

Needle Operated at Ground Potential

Experiments presented in Chapter 5 were performed using an electrospray source which used a needle operated at ground potential. In the electrospray source used in Chapters 3 and 4, the spray needle, where the high voltage is applied, is directly in contact with the solution reservoir. Thus, an inexperienced user has the potential of getting an electrical shock. To protect the user from electrical shock and isolate the liquid introduction system from high voltage, the commercial electrospray source (Anaytica of Branford) was constructed with the spray needle operating at ground potential. In this design, a dielectric capillary is used, as opposed to a stainless steel capillary. As shown in Figure 2.7, the high voltage is applied to the metalized entrance of a 20 cm long glass capillary (0.500 mm i.d.). The electric field produced by the voltage applied to the mesh cylinder assists in disintegration of large droplets to small droplets. Solvent desolvation in the spray chamber (capillary/needle region) is assisted by a counter flow of heated N<sub>2</sub> gas. In addition, the double layered spray needle (metal tubing around the spray needle) allows a gas or liquid sheath to flow along with the spray. Often SF<sub>6</sub> or O<sub>2</sub> is introduced through this outer tubing to suppress discharge when the ESI source is operated in the negative ion mode. This type of ESI source has been coupled with triple quadrupole, magnetic sector, time

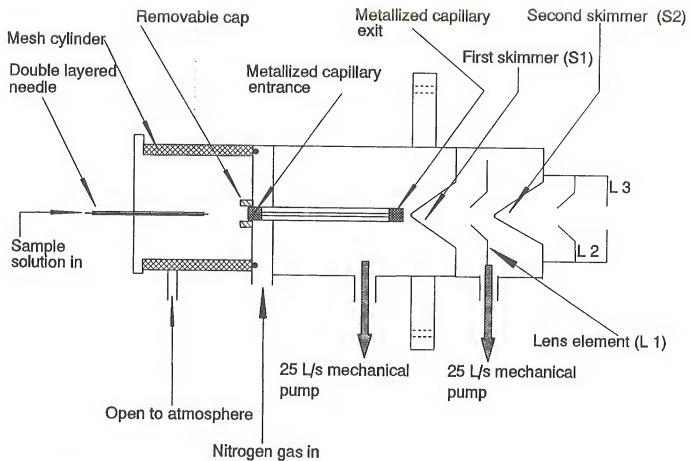


Figure 2.7

A schematic representation of the external electrospray source used with the 4.7 T FTICR mass spectrometer.

of flight and ion trap mass spectrometers. The ESI source comes with two stages of pumping. The region between the glass capillary and the first skimmer (S1) was pumped by a 25 L/s mechanical roughing pump and the pressure in this region is maintained at ca. 1-1.5 Torr. The region between the first skimmer and the second skimmer (S2) is pumped by another 25 L/s mechanical pump and the pressure is maintained in the ca.  $10^{-2}$  Torr range. L<sub>1</sub>, L<sub>2</sub> and L<sub>3</sub> are lens elements which are used for focusing the ions.

#### Instrumentation

##### Internal Source ESI/FTICR Mass Spectrometer

All experiments in chapters 3 and 4 were performed using a home-built FTICR mass spectrometer equipped with a Nicolet prototype 2 Tesla superconducting magnet. The mass spectrometer was controlled either by a Nicolet FTMS 1000 (170) or Ion Spec (171) data station. A schematic representation of the FTICR mass spectrometer used in this study is shown in Figure 2.8. The 1.9 cm o.d. probe with the PEEK spray assembly was inserted inside a 4 cm o.d. vacuum chamber which terminated with a blunt-ended 0.2 mm orifice copper skimmer. The pressure in this first pumping stage was maintained at ca. 2.3 Torr by two 25 L/s mechanical roughing pumps. The capillary and the skimmer were separated by an

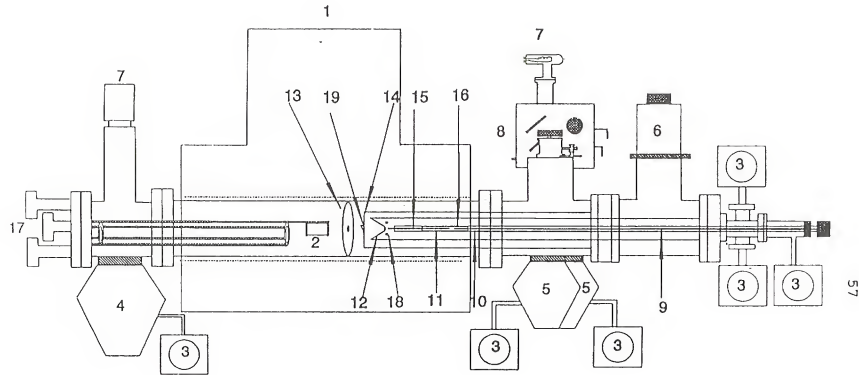


Figure 2.8 A schematic representation of the internal source electrospray ionization FTICR mass spectrometer. (1)2 Tesla superconducting magnet, (2)analyzer cell, (3)mechanical pumps, (4)700 L/s diffusion pump, (5) 300 L/s diffusion pump, (6)800 L/s cryopump, (7)ion gauges, (8)gas/liquid inlet, (9)Teflon tubing, (10)1.9 cm o.d. stainless steel tube, (11)PEEK spray cavity, (12)skimmer, (13)second conductance plate, (14)first conductance plate, (15)heated desolvating capillary, (16)syringe spray needle, (17)laser windows, (18)tube lens, and (19)shutter.

adjustable distance of 5-8 mm. The 4 cm o.d. vacuum chamber was inserted into a 10.2 cm o.d. vacuum chamber which ended with a 4 mm orifice conductance limit (1<sup>st</sup> conductance plate). The pressure in this region was maintained at  $10^{-5}$  Torr by a 800 L/s cryopump (for N<sub>2</sub>). The skimmer and the 1<sup>st</sup> conductance plate were separated by a distance of 2.5 cm. Finally, this entire assembly was inserted into a 15.2 cm o.d. vacuum chamber (the 1 meter long vacuum chamber was mounted inside the 200 mm room temperature bore of the superconducting magnet) which was separated from the FTICR cell by another 4 mm orifice conductance limit (2<sup>nd</sup> conductance plate). The ESI source side of the 2<sup>nd</sup> conductance plate was pumped by two 300 L/s diffusion pumps (10 cm diameter) and the pressure in this region was maintained at  $10^{-7}$  Torr. The cell side of the 2<sup>nd</sup> conductance plate was pumped by a 700 L/s diffusion pump (15 cm diameter) and the pressure was maintained at  $3.5 \times 10^{-8}$  Torr during electrospray operation. A distance of 2.5 cm separated the 1<sup>st</sup> conductance plate from the 2<sup>nd</sup> conductance plate and the 2<sup>nd</sup> conductance plate from the front trap plate. This system was equipped with three laser windows on the 20.3 cm cell flange.

FTICR Cell Used in Internal ESI Studies

A stainless steel cell (2.5 x 2.5 x 4.5 cm) was used in all internal ESI/FTICR studies. This FTICR cell, which is

situated in the homogeneous magnetic field of the 2 Tesla superconducting magnet, comprises six electrodes: two trapping plates, two excite plates and two detect plates. Two MACOR spacers held all six electrodes together and electrically isolated each plate. When positive or negative ions were to be trapped in the cell, the voltage on the trap plates was made positive or negative, respectively, to prevent escape of the ions along the z-axis. The combination of trapping voltage and magnetic field confined the ions for periods of milliseconds to seconds. A trapping potential of 4.0-10.0 V was used in all internal source ESI/FTICR experiments.

Trapped ions leave the cell either by ion-molecule collisions, or by a reverse-polarity quench pulse. During the later a positive voltage is applied to one of the trap plates and a negative voltage is applied to the other. Positive ions are accelerated toward the trap plate with the negative voltage and negative ions are accelerated toward the trap plate with the positive voltage, where these ions are neutralized by collisions with the respective trap plates.

The front trap plate (the trap plate facing the 2<sup>nd</sup> conductance plate) was made with a 2 cm diameter hole over which 90% transparent stainless steel mesh was spot welded to maintain the required trapping potential. A solid plate was used as the back trap plate of the cell. Ion current was measured on the back trap plate for optimizing electrospray source operating parameters. In addition, the kinetic energy

of ions entering the cell was determined by applying a dc potential to the front trap plate and measuring the ion current on the back trap plate (chapter 3). Figure 2.9 gives a three-dimensional view of the FTICR cell used for the studies discussed in Chapters 3, 4 and 6 (a laser was also used in the experiments presented in chapter 6).

#### FTICR Pulse Sequences used with Internal ESI experiments

A typical pulse sequence used for internal source ESI/FTICR mass spectrometry is shown in Figure 2.10. The pulse sequence used with the Ion Spec data station involved a quench pulse to one of the trap plates to eject any ions present in the cell, followed by a variable quench delay time. The pulsed valve was opened briefly to allow argon to enter the cell (peak pressure  $4.0 \times 10^{-4}$  Torr). Immediately after the first trigger pulse, a second trigger pulse opened the shutter (chapter 3) for 1 s. This allowed ions to enter the cell from the ESI source. After this ion injection period the shutter was closed and the shutter head was used to monitor the current due ions produced from the source. While ion current was being monitored, a 3 s delay time allowed the ions to be thermalized by ion-neutral collisions with argon. This delay time also allowed most of the thermalizing gas to be pumped out of the vacuum chamber. If ion isolation was necessary, a series of ion ejection sweeps was employed during

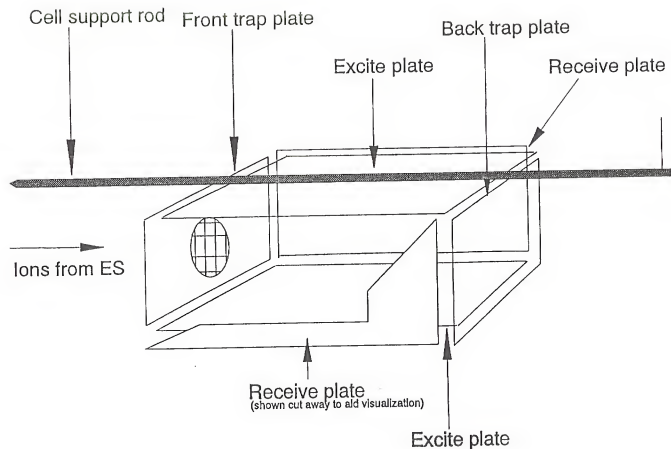


Figure 2.9

A schematic representation of the FTICR cell used with internal source ESI/FTICR mass spectrometry.

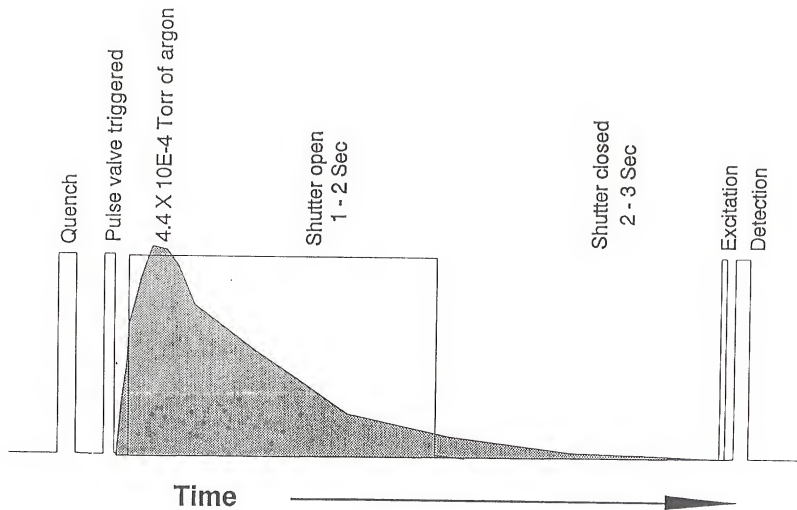


Figure 2.10 Pulse sequence used for internal source ESI/FTICR mass spectrometry.

this 3 s delay. The trapped ions were excited using standard chirp excitation in the broad-band mode and ions in the mass range of 15-2000 Da were detected. Generally, for each spectrum 16384 data points were acquired by signal averaging 50-100 time-domain transients.

The Nicolet FTMS 1000 data station's electronics had the capability of pulsing the trap plates and achieving trap voltages up to 10 V. Thus, the pulse sequence shown in Figure 2.10 was modified. After the quench pulse, during DL1 (delay time 1), the trap plate potential was raised to an optimal value between 1.5 V to 10 V. Since the kinetic energy of the ions entering the cell depends on the optimum skimmer potential (Chapter 3), the trapping plate potential was dependent on the skimmer potential. While holding both trapping plate potentials high the shutter and/or the pulse valve were opened (DL1) and then closed for 1 s during DL2 (delay time 2). Ion isolation was done while the shutter was in its closed position. Then during DL5, both trapping plates were returned to 1.5 V and immediately ions were excited using standard chirp excitation in the broad-band mode and ions in the mass range of 15-2000 Da were detected.

#### External Source ESI/FTICR Mass Spectrometer

All experiments were performed using a Bruker Bio-APEX 47e mass spectrometer (172) equipped with a 4.7 Tesla

superconducting magnet, an external ion source, and a RF-shimmed "Infinity" analyzer cell (149). Figure 2.11 shows the external source ESI/FTICR mass spectrometer. The basic features of the external ion source FTICR mass spectrometer and the operating parameters used in these experiments have been described in detail (100). The external ion source has two stages of differential pumping and the electrospray source has two additional stages of pumping. The electrostatic ion transfer region and the FTICR cell regions were pumped by separate 400 L/sec cryopumps and the pressure in the cell region was maintained at  $5 \times 10^{-9}$  Torr during the electrospray operation. A 800 L/sec cryopump maintained the external ion source region pressure at  $6 \times 10^{-5}$  Torr during electrospray operation.

#### FTICR Cell Used in External ESI Studies

A cylindrical cell termed the "Infinity" cell was used in all external ESI/FTICR studies described in Chapter 5. This type of cell was first demonstrated by Caravatti et al.(49). They referred to it as an infinity cell because the design of the cell was based on a model of the electric excitation field of an infinitely long cell. The major advantage of this type of cell is the virtual elimination of z-axis ejections compared to cubic or elongated cells. The infinity cell used in these experiments (Figure 2.12) was situated in the

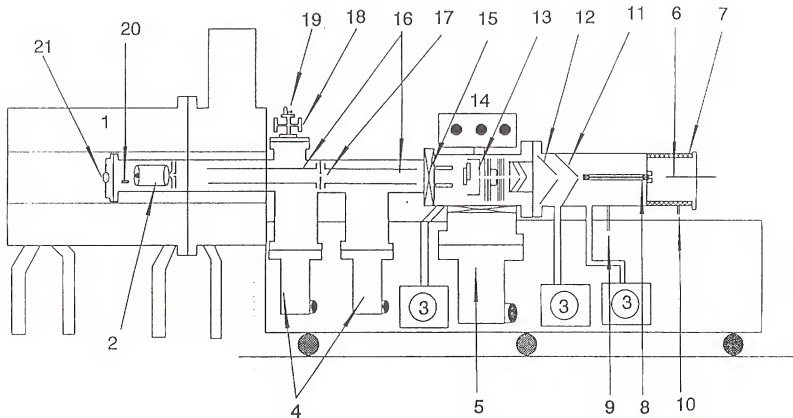


Figure 2.11 A schematic representation of the external source electrospray ionization FTICR mass spectrometer. (1)4.7 Tesla superconducting magnet, (2)Infinity analyzer cell, (3)mechanical pumps, (4)400 L/s cryopumps, (5)800 L/s cryopump, (6)grounded needle, (7)mesh cylinder, (8)500  $\mu\text{m}$  i.d. glass capillary, (9) $\text{N}_2$  gas in, (10) $\text{N}_2$  gas out, (11) skimmer #1, (12)skimmer #2, (13)ion transfer optics, (14)gas/liquid inlet, (15)gate valve, (16)electrostatic ion transfer optics, (17) conductance limit, (18)pulse valve, (19)leak valve, (20)internal filament and (21)laser window.

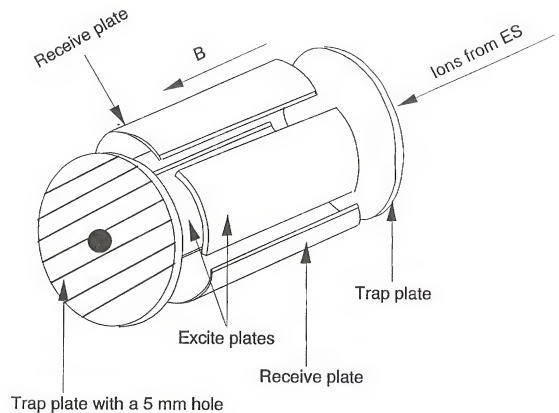


Figure 2.12 A schematic representation of the Infinity FTICR cell used with external source ESI/FTICR mass spectrometry.

homogeneous magnetic field of the 4.7 Tesla superconducting magnet (150 mm diameter room temperature bore). The titanium cylinder (6.0 cm length and 6.0 cm diameter) was divided into four isolated 90°-sector electrodes. The first pair of opposed sectors was used as receive electrodes and the second pair as the excite electrodes. Trapping plates were 6.0 cm diameter copper coated ceramic discs which were separated into eleven segments.

#### Laser Desorption FTICR Mass Spectrometer

Laser desorption experiments described in Chapter 6 were performed in a mass spectrometer equipped with a Ion Spec data station, Nicolet FT/MS 1000 vacuum assembly, 3 Tesla Oxford superconducting magnet, and a heated inlet system equipped with two precision leak valves. The high vacuum chamber (7.8 cm inside diameter) was pumped by a 300 L/s oil diffusion pump. A second diffusion pump with a pumping speed of 150 L/s was mainly used for initial pump down of the system and to pump on the inlet system. The background pressure of the system was maintained at  $5 \times 10^{-9}$  Torr during the FTICR detection period. In addition, baking the high vacuum chamber at 100 °C overnight further helped to maintain the background pressure at  $5 \times 10^{-9}$  Torr. This high vacuum chamber was mounted inside the 150 mm bore of the superconducting magnet. This system was equipped with one laser window on the 10.2 cm cell flange.

FTICR Cell Used in LD Studies

The stainless steel cell ( $2.5 \times 2.5 \times 4.5$  cm) used in all internal ESI/FTICR experiments was also used in charge transfer reaction studies, except that the solid back trap plate was replaced with a mesh trap plate. The cell trapping plates were each made with a 2 cm diameter hole over which 90% transparent stainless steel mesh was spot welded to maintain the required trapping potential. A trapping potential of -2.0 V was used in all experiments. The carbon clusters were produced by focusing (7.63 cm focal length ZnSe lens) the 10.6  $\mu\text{m}$  output from a Lumonics CO<sub>2</sub> laser through the front and back trap plates onto a graphite plug mounted behind the back trap plate of the cell. The carbon cluster ions produced by the laser desorption of the graphite plug traveled along the magnetic field and entered the cell through the back trap plate. Figure 2.9 gives a three-dimensional view of the FTICR cell.

FTICR Pulse Sequences used with LD experiments

Two different pulse sequences were used in carbon cluster charge-transfer reaction studies. The first pulse sequence involved applying a quench pulse to both trap plates to eject any ions present in the cell. The laser was then triggered and a pulsed valve was opened briefly to allow argon to enter

the cell (peak pressure  $5 \times 10^{-6}$  Torr). Next, a 2000 ms delay time allowed the ions to be thermalized by ion-neutral collisions with argon. This delay time also allowed most of the thermalizing gas to be pumped out of the vacuum chamber. A series of ion ejection sweeps was then used to isolate the cluster cation of interest. After the cluster ion was isolated, a variable reaction time allowed the charge-transfer reaction to take place. In the second pulse sequence, continuous ejection of a non-charge transfer reaction product took place during the charge-transfer reaction period. Ions were excited by the standard frequency chirp excitation method and 16K time-domain points were acquired during broad-band detection (25-400 amu). For each reaction delay time, 50 scans were averaged to enhance the signal to noise ratio. The intensities of the reacting cluster ion and product ions formed by ion-molecule reaction(s) were followed for a time period which ranged from 1 to 10 s. Integrated peak intensities for all major ions were obtained at 15 to 20 different reaction delay periods of approximately equal spacing during each experiment. Plots of relative ion intensities vs. reaction time were then made to demonstrate the occurrence or non-occurrence of charge transfer reactions.

CHAPTER 3  
DEVELOPMENT AND OPTIMIZATION OF INTERNAL  
SOURCE ELECTROSPRAY IONIZATION FTICR MASS SPECTROMETRY

Introduction

As discussed in chapter 1, electrospray ionization (ESI) sources have expanded mass spectrometric capabilities for analyses of high molecular weight compounds that were previously inaccessible by other ionization techniques. The intense interest in ESI mass spectrometry is evidenced by recent special issues of *Journal of the American Society for Mass Spectrometry* (Vols. 7 and 8, 1993). These issues are devoted exclusively to ESI mass spectrometry theory, instrumentation and applications.

Mass spectrometric methods available for the analysis of high molecular weight compounds are described in chapter 1. Electrospray ionization mass spectrometry has evolved into a routine analytical technique necessary in the study of peptides and proteins. The multiple charging phenomenon of ESI allows the determination of molecular weights of nonvolatile compounds in excess of 100,000 Da with fairly simple quadrupole mass spectrometers. Although molecular weight determination of a pure sample is attainable with quadrupoles, molecular weight information of sample mixtures

can be a difficult task. Furthermore, if the mixture contains overlapping charge-state distributions, then the analysis becomes somewhat difficult with the unit resolution available with quadrupole mass spectrometry.

To overcome the limited mass resolution available with other types of mass spectrometry, McLafferty et al. (94) coupled an ESI source with a FTICR mass spectrometer. The high mass resolution capability of ESI/FTICR mass spectrometry was demonstrated by obtaining a mass spectrum of equine cytochrome C (MW = 12,358 Da) with a mass resolution of 62,000. Through the detection of chicken cytochrome C (MW = 12,236 Da) with a mass accuracy of  $\pm 0.48$  Da (95), this group further demonstrated the high mass accuracy capability of ESI/FTICR mass spectrometry.

Although high mass resolution and mass accuracy were demonstrated by McLafferty et al. (94-95), sensitivity problems associated with their ESI/FTICR mass spectrometer limited it from routine applications. The most common type of mass analyzer used with ESI is the quadrupole mass spectrometer. Electrospray ionization/quadrupole interfaces deliver between 20 to 50 pA of ion current to the mass analyzer (173). In contrast, ESI/FTICR mass spectrometer demonstrated by McLafferty et al. delivered between 1 to 2 pA of ion current to the FTICR analyzer cell. The inefficient transfer of ions from the ESI source to the FTICR cell was due to the positioning of the ESI source more than a meter away

from the analyzer cell (external source ESI). In the McLafferty design, ions were transferred from the ESI source to the FTICR cell by three sets of quadrupole rods. Ion losses during the transfer and the broad kinetic energy distribution of the ions limited the performance of the external source ESI/FTICR mass spectrometer.

With the intention of increasing the sensitivity, Hofstadler and Laude (85) recently demonstrated a new approach to external source ESI/FTICR. In this new approach, an electrospray ionization source was positioned in the high magnetic field of a 3 Tesla superconducting magnet (internal source ESI). The confining nature of the magnetic field focussed the ions radially and delivered them more efficiently into the analyzer cell. In addition, positioning the ESI source much closer to the FTICR analyzer cell minimized ion losses during transfer from the source to the analyzer cell.

The differential pumping capabilities of the internal source instrument were limited due to placing the ESI source inside the magnetic field ca. 25 cm from the analyzer cell. To achieve the required lower pressure for the FTICR detection event, it was necessary for Laude et al. (85) to use four concentric vacuum chambers and a dual FTICR analyzer cell. Unlike the external source ESI/FTICR, where a virtually unlimited number of differential pumping stages are possible, with internal source ESI/FTICR the differential pumping is limited by the distance between the ESI source and the FTICR analyzer cell.

Following Laude's demonstration, we modified our 2 Tesla FTICR mass spectrometer to accommodate an internal ESI source (174). Although Laude and Hofstadler demonstrated this interface in 1992, several limitations were attached with their internal ESI/FTICR mass spectrometer. The primary limitation was inadequate differential pumping. This required their detection to occur at  $2.0 \times 10^{-7}$  Torr rather than in the low  $10^{-8}$  Torr range. In this chapter, development and optimization of the internal source ESI/FTICR mass spectrometer will be discussed, and the steps necessary to circumvent most of the problems associated with this technique will be addresssed.

#### Concentric Tube Vacuum Chamber Assembly

The concentric tube vacuum chamber assembly was constructed in an effort to couple the atmospheric pressure ESI source with a low pressure FTICR mass spectrometer. The design of the concentric vacuum assembly encompassed spatially separated stainless steel tubes, each terminating with a conductance limiting orifice. The differential pumping arrangement allowed us to position the high-pressure ionization source within the high magnetic field of the FTICR mass spectrometer. The mass spectrometer utilized a 2 Tesla Nicolet prototype superconducting magnet with a 58 cm long and 20.3 cm diameter warm bore. The concentric tube vacuum

chamber assembly was constructed within this bore. The magnet bore housed a 15.2 cm o.d. x 14.6 cm i.d. stainless steel tube which terminated with a 20.3 cm flange at both ends. As shown in Figure 2.8, the front 20.3 cm flange was connected to a six-way cross, which supported a 700 L/s diffusion pump, along with the front ionization gauge, cell support flange, pulsed valve and the variable leak valve assembly. The back 20.3 cm flange was connected to a four-way cross (20.3 cm flange) which supported two 300 L/s diffusion pumps, a 20.3 cm flange welded to 10.2 cm o.d. stainless steel tubing (second differentially pumped vacuum chamber) and a 20.3 cm flange tee. The tee supported a 800 L/s (for nitrogen and 2900 L/s for water) cryo pump and a 20.3 cm flange welded to a 4.1 cm o.d. stainless steel tube (first differentially pumped vacuum chamber).

#### First Differentially Pumped Vacuum Chamber

The first differentially pumped region was created by the 4.1 cm o.d. x 1 m long stainless steel tube which terminated with a skimmer. One end of the 4.1 cm o.d. tubing was welded to a 7 cm flange and the other end was modified by welding the stainless steel piece shown in Figure 3.1 (inset) to accommodate a Delrin skimmer holder. A 20.3 cm flange was welded on the 4.1 cm o.d. stainless steel tubing, approximately 3.5 cm from the 7 cm flange to support tubing on

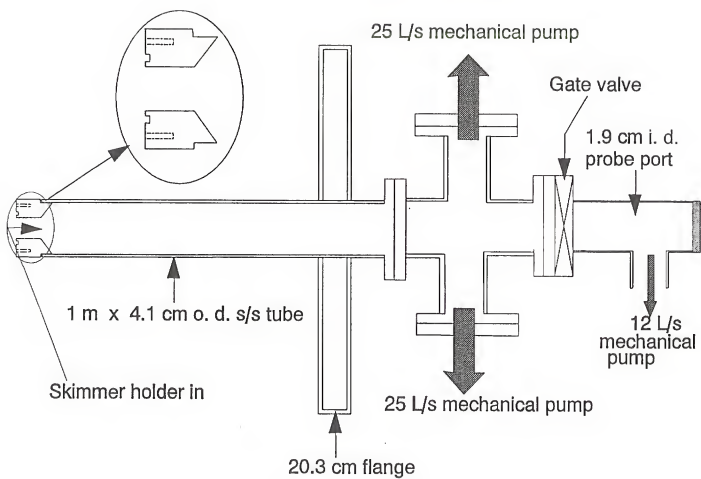
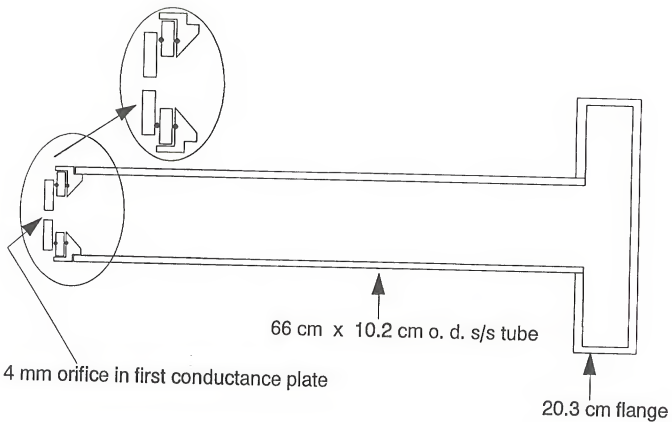


Figure 3.1 A schematic representation of the first differentially pumped vacuum chamber and its components.

a three-way cross (20.3 cm flange). Two high-voltage feedthroughs were welded on this 20.3 cm flange for supplying the dc potentials required for the skimmer and the lens element. As shown in Figure 3.1, a four-way cross (7 cm flange) was attached to the 7 cm flange in order to support a 1.9 cm vacuum interlock probe port and two 25 L/s mechanical pumps. These two mechanical pumps maintained the pressure in this region between 2 to 10 Torr during the operation of the ESI source. This vacuum chamber terminated with a 1.6 mm thick copper skimmer. For system optimization and high mass resolution experiments, a 0.35 mm and a 0.2 mm orifice skimmer were used, respectively. The skimmer was positioned in the 1.78 Tesla region of the 2 Tesla magnet (175).

#### Second Differentially Pumped Vacuum Chamber

A 10.2 cm o.d. x 9.8 cm i.d. stainless steel tube with a length of 66 cm was used as the second differentially pumped region (Figure 3.2). One end of the tube was welded into a 20.3 cm flange which was supported in between a three-way cross ( 20.3 cm flange) and a four-way cross (20.3 cm flange) as shown in Figure 3.3. Four high-voltage feedthroughs were welded into this 20.3 cm flange to provide the dc potentials required for both conductance plates and the shutter (*vide infra*). The other end of the 10.6 cm o.d. tubing was modified by welding the stainless steel piece shown in Figure 3.2



2

2

Figure 3.2

A schematic representation of the second differentially pumped vacuum chamber and its components.

(inset). A 9.8 cm o.d. x 9.5 mm thick Teflon insulating piece with a 7.1 cm orifice was attached to the stainless steel piece to electrically isolate the conductance limiting plate. The vacuum chamber terminated with a 4 mm conductance limiting orifice (first conductance plate), which was fabricated from a 8.9 mm o.d. and 1.6 mm thick stainless steel plate. When the 10.2 cm o.d. vacuum chamber is positioned inside the magnetic field, a distance of 2.5 cm separated the first conductance limiting orifice from the skimmer orifice. Magnetic field strength measurements along the z-axis suggest that the first conductance limiting orifice is positioned in a field strength of 1.88 Tesla (175). As shown in Figure 3.3, a 800 L/s cryo pump attached to the three-way cross allowed the pressure in this region to be maintained at ca.  $1\text{--}5 \times 10^{-5}$  Torr during the operation of the ESI source.

#### Third and Fourth Differentially Pumped Vacuum Chambers

Separating the 15.2 cm o.d. x 14.6 cm i.d. stainless steel tubing which was positioned inside the bore of the 2 Tesla magnet allowed us to create the third and fourth differentially pumped regions. As shown in Figure 3.3, a 14.6 o.d. x 9.5 mm thick Delrin disc with a 2.5 cm orifice was attached to the second differentially pumped chamber with eight 3.8 mm o.d. x 1.6 cm long aluminum standoffs. The 2.5 cm Delrin orifice was covered with a 4.5 cm diameter x 1.6 mm

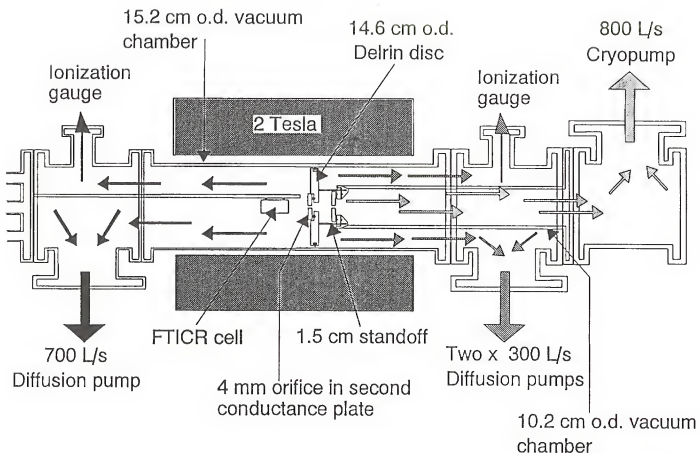


Figure 3.3 A schematic representation of the third and the fourth differentially pumped vacuum chambers.

thick stainless plate with a 4 mm orifice, which functioned as the second conductance limiting orifice (second conductance plate). The Delrin disk with the second conductance limiting orifice was positioned 1.6 cm from both the front trap plate of the FTICR analyzer cell and the first conductance limiting orifice. A distance of 2.5 cm separated both conductance plates. The Delrin disc was positioned in the 2 Tesla field region of the superconducting magnet utilized with the FTICR mass spectrometer. The ESI source side, or the third differentially pumped region, was pumped by two 300 L/s oil diffusion pumps and the pressure was maintained at  $5 \times 10^{-6}$  and  $4 \times 10^{-7}$  Torr when operated without and with the shutter (0.2 mm skimmer), respectively. The cell side, or the fourth differentially pumped region, was pumped by a 700 L/s oil diffusion pump and pressure was maintained at  $2 \times 10^{-7}$  and  $3.5 \times 10^{-8}$  Torr when operated without and with the shutter (0.2 mm skimmer and 2.3 Torr in the capillary-skimmer region), respectively. Using a 0.35 mm orifice skimmer increased the pressure in the cell region to  $5.7 \times 10^{-7}$  and  $1.3 \times 10^{-7}$  Torr when operated without and with the shutter, respectively.

Figure 3.4 shows the completed concentric tube vacuum assembly positioned inside the 2 Tesla FTICR mass spectrometer. Construction of the concentric tube vacuum chamber was followed by the optimization of the following: the ESI source design, spray needle-desolvating capillary distance, desolvating capillary-skimmer distance, sample

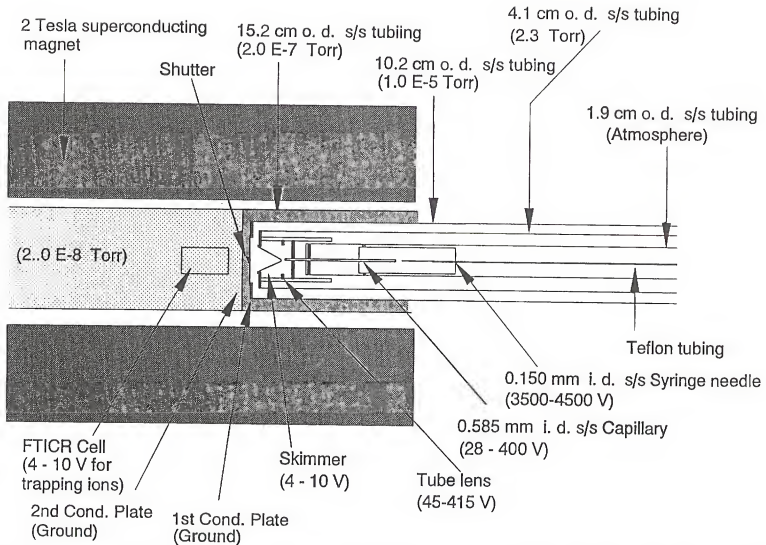


Figure 3.4 Concentric tube vacuum chamber assembly positioned inside the bore of the 2 Tesla FTICR mass spectrometer.

solution flow rate, skimmer holder design, skimmer and trapping plate potentials. In addition, installation of a shutter to open only during the ion transfer event and a tube lens between the skimmer and the capillary increased the performance of the internal source ESI/FTICR mass spectrometer.

#### Optimization of the ESI Source

Four different ESI source designs were tried in our laboratory. The first design was designated as "ESI Source I". As shown in Figure 3.5, the spray cavity was fabricated from a 1.7 cm outside diameter (o.d.) x 15 cm long Delrin rod. Most of the Delrin, except for a 1.5 cm region in the front and a 2.5 cm region in the back which were not machined, was machined away for creating a spray cavity. In the center of both unmachined Delrin regions, a 6.4 mm hole was placed to accommodate a Swagelok fitting. A 1.6 mm Swagelok fitting with a graphitized Vespel ferrule was threaded into both 6.4 mm holes. Swagelok fittings helped to position a stainless steel desolvating capillary (0.585 mm i.d. and 15 cm long, optimization described below) and a stainless steel spray needle (blunt-ended 0.15 mm i.d. x 6.5 cm long, dimensions of the spray needle used by Laude et al. (85)) with a separation of 6 mm. Five holes were machined around the back Swagelok fitting to accommodate two heating wires (2 mm o.d.), two

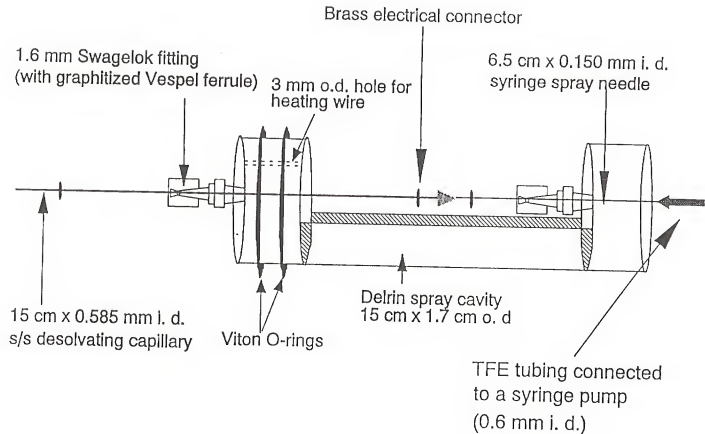


Figure 3.5 A schematic representation of the first design adopted in constructing the internal ESI source.

thermocouple wires (2 mm o.d.) and a high voltage wire (3.6 mm o.d.). One hole was machined around the front end Swagelok to accommodate the front heating wire. The Swagelok fitting in the back made a seal between the Teflon (TFE) tubing (providing the sample solution) and the spray needle. This allowed the sample solution to flow only through the spray needle (prevented the sample solution from leaking and initiating a discharge). The second Swagelok prevented atmospheric air from entering around the capillary into the capillary/skimmer region. The delrin ESI source was inserted inside a 1.9 cm o.d. x 1.7 cm i.d. stainless steel (s/s) tube whose total length was 180 cm. As shown in Figure 3.6, a vacuum seal was made with two Viton O-rings (1.4 cm i.d., 1.7 cm o.d. and 1.8 mm width) and the capillary extended 9.5 cm beyond the end of the 1.9 cm probe.

This design posed several problems: (i) even though the vacuum seal was made with both o-rings, the friction between the o-rings and the probe wall was not sufficient to withstand the high pumping speed (two 25 L/s mechanical pumps). This allowed the ESI source to be pulled out from the 1.9 cm probe and the vacuum chamber was often vented. (ii) Heating the desolvating capillary above 100 °C softened the Delrin spray cavity. The area around the front Swagelok fitting softened faster than any other area and atmospheric air started to leak into the vacuum chamber. (iii) The long (9.5 cm) extension of the capillary beyond the 1.9 cm probe made the probe difficult to insert as well as pull out from the vacuum chamber. (iv)

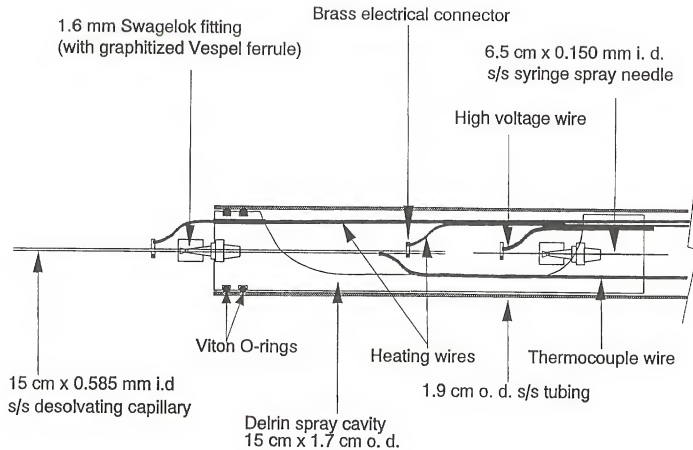
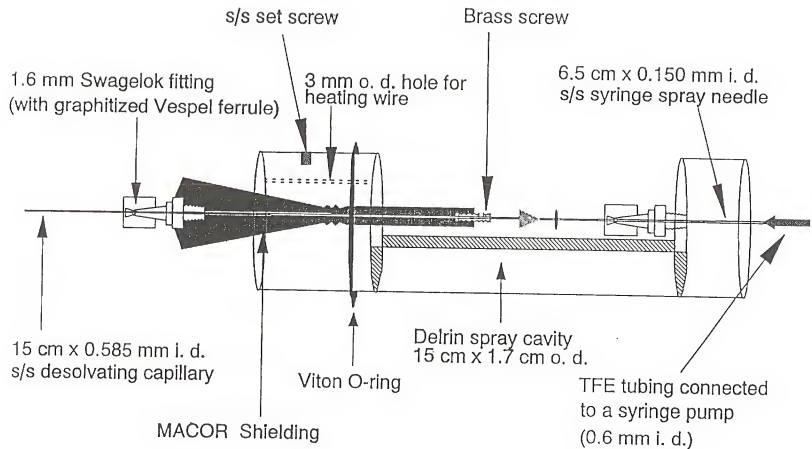


Figure 3.6

A schematic representation of the "ESI source I" positioned inside the 1.9 cm od stainless steel probe.

Since the design did not have any clear stopping point for the capillary inside the skimmer holder (*vide infra*), the capillary posed the potential of coming in contact with the skimmer and damaging it.

To alleviate the problems encountered with the first design, a second design called "ESI Source II" was fabricated from Delrin and MACOR. As shown in Figure 3.7, a 1.7 cm o.d. x 15 cm long Delrin rod was machined to accommodate the syringe spray needle (0.150 i.d. x 6.5 cm long) and a 8.9 cm long MACOR rod. A 1.3 cm o.d. MACOR cylinder was machined to have three different od's to accommodate the front Swagelok, tapering threads to seal against the Delrin, and the desolvating capillary. To prevent any leak between the MACOR/Delrin seal, TFE Teflon tape was utilized around the tapering threads on the MACOR. As illustrated in Figure 3.8, to prevent the source from being pulled into the high vacuum region, the front Viton O-ring was eliminated and a set screw was used to fasten the Delrin spray cavity to the 1.9 cm o.d. probe. To protect the capillary from bending and the skimmer from any damage, the ESI source was positioned farther inside the 1.9 cm probe and the capillary was allowed to extend only 2 cm from the end of the probe (this required the modification of the skimmer holder, which is explained below). In addition, a 1.7 cm o.d. x 6.4 mm thick MACOR disc was placed at end of the 1.9 cm probe to center the capillary. This arrangement helped with the alignment of the capillary and the skimmer along the z-axis.



7.7

Figure 3.7 A schematic representation of the second design adopted in constructing the internal ESI source.

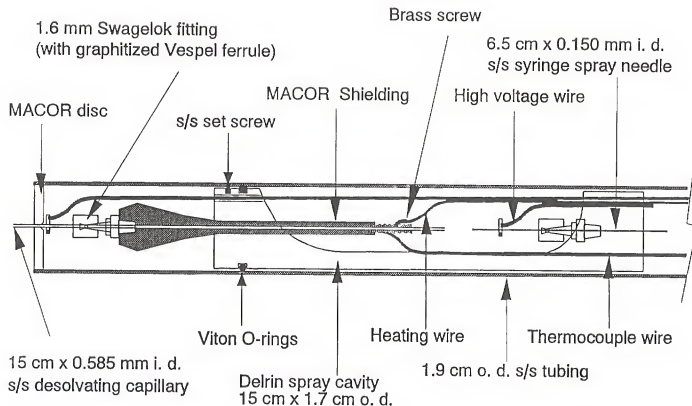
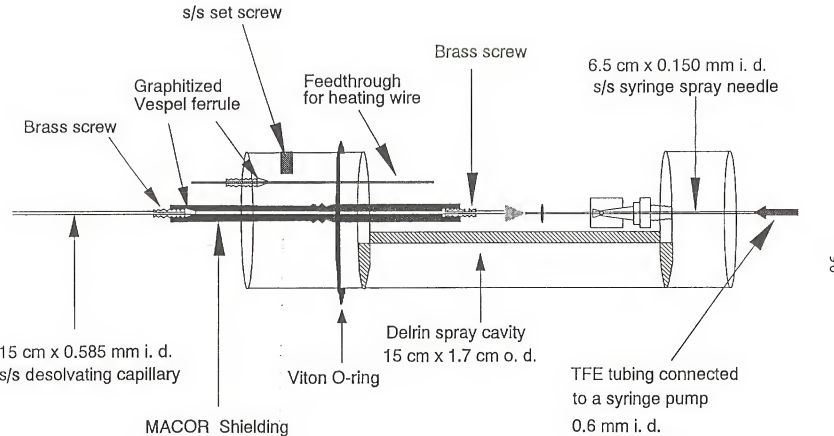


Figure 3.8 A schematic representation of the "ESI source II" positioned inside the 1.9 cm od stainless steel probe.

The addition of MACOR shielding allowed us to heat the capillary to a desired temperature. Usually, the temperature was maintained above 100 °C to achieve desolvation of the methanol and water sample solution. Allowing the capillary to protrude only 2 cm from the end of the 1.9 cm probe and redesigning the skimmer holder (*vide infra*) allowed the capillary to stop at a 4 mm (minimum separation from our capillary/skimmer optimization study) distance from the skimmer orifice. Although this design worked much better than the first design, the brittle nature of the MACOR material caused it to break several times. Another problem was the front Swagelok fitting; the bulkier fitting got hot faster than the desolvating capillary and developed a leak around the MACOR/Swagelok fitting region. In addition, after 3 to 4 hours operation the vacuum seal between the MACOR and Delrin started to leak and caused the pressure in the capillary/skimmer region to increase. Another atmospheric air leak was found around the front heating wire. Often these leaks were prevented by using Torr seal. However, the use of Torr seal was limited due to its low maximum operational temperature, which was less than 120 °C.

A schematic representation of the third ESI source designed in our laboratory is shown in Figure 3.9. Elimination of the front Swagelok fitting required less MACOR material and reduced the cost for building the ESI source as well as circumvented the problem of leaking around the



**Figure 3.9** A schematic representation of the third design adopted in constructing the internal ESI source.

MACOR/Swagelok area and around the front heating wire. In this design both ends of the desolvating capillary were held in place by a graphitized Vespel ferrule with a brass screw. Reduction of the MACOR material provided more area for the addition of a feedthrough for the front heating wire. These graphitized Vespel ferrule/brass screw vacuum seals prevented most of the atmospheric air leak and achieved lower pressure in the capillary/skimmer region. Although this design had fewer problems than both previous designs, operation of the source for 3 to 4 hours resulted in atmospheric air leak around the MACOR/Delrin seal.

The final ESI source design, which eliminated all the problems encountered with previous designs, is shown in Figure 3.10. In this design, we removed both the Delrin and the MACOR material and fabricated the ESI spray cavity with Polyether ether ketone (PEEK). The PEEK material allowed us to heat the desolvating capillary above 175 °C without softening or melting the spray assembly. The graphitized Vespel ferrule/brass screw assembly was used to make a vacuum seal around the front heating wire feedthrough and the desolvating capillary. This design allowed us to achieve much lower pressure in the capillary/skimmer region compared to the first and second designs. Also, the use of PEEK material in fabricating the internal ESI source allowed us reduce the cost from \$ 180 for a 30 cm x 1.3 cm o.d. MACOR rod to \$ 35 for a 30 cm x 1.9 cm o.d. PEEK rod.

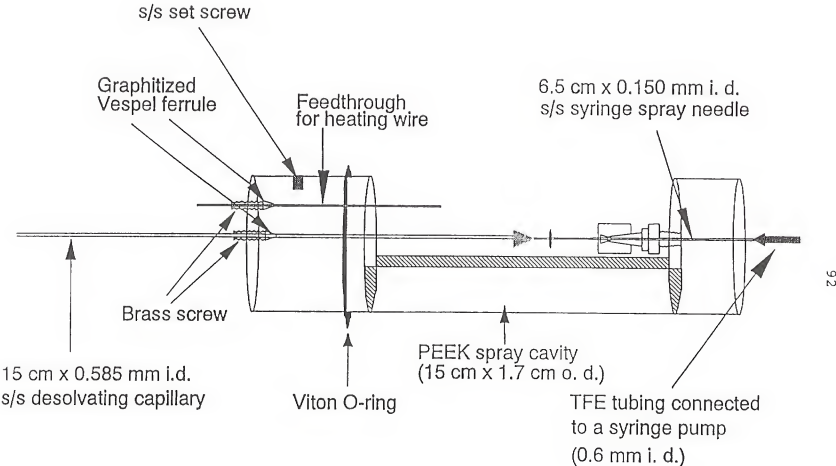


Figure 3.10 A schematic representation of the fourth design adopted in constructing the internal ESI source.

Optimization of the Spray Needle-Capillary Distance, Spray Needle Potential and the Sample Solution Flow Rate

An equation relating the spray needle potential and the distance between the spray needle and the counter electrode (capillary) was obtained by Smith (161). As shown in Equation 3.1, the electric field ( $E_{needle}$ ) at the tip of the spray needle depends on the outer wall radius of the spray needle ( $r_{needle} = 0.2$  mm), the distance between the spray needle and the capillary ( $d = 6$  mm) and the potential applied to the spray needle ( $V_{needle}$ ).

$$E_{needle} = [2V_{needle}/r_{needle}] \ln[4d/r_{needle}] \quad (3.1)$$

In addition to providing a relationship for calculating the electric field at the needle tip, Smith (161) has shown that the onset of instability of the liquid cone leading to electrospray can be expressed using Equation 3.2.

$$E_{onset} = [2\gamma \cos\theta_0 / \epsilon_0 r_n]^{1/2} \quad (3.2)$$

where  $\gamma$  is the surface tension of the liquid,  $\theta_0$  is the half-angle of the Taylor cone,  $r_n$  is the outer radius of the spray needle and  $\epsilon_0$  is permittivity of vacuum. Combining Equations 3.1 and 3.2 and substituting  $49.3^\circ$  for the half-angle of the Taylor cone (164) and  $\epsilon_0 = 8.8 \times 10^{-12} \text{ J}^{-1}\text{C}^2\text{m}^{-1}$  result in Equation 3.3. Experimental verification of Equation 3.1 has

been provided by Smith (161) and Kerbale et al. (176-177).

$$V_{on} = 2 \times 10^5 (\gamma r_n)^{\frac{1}{2}} \ln(4d/r_n) \quad (3.3)$$

The spray needle current,  $I$ , which results from charged droplets leaving the spray needle, is important because it provides information about the ions produced by the ESI processes. In 1968 Pfeifer and Hendricks (160) developed a theoretical relationship showing the parameters which can effect the ESI processes. Equation 3.4 gives the expression proposed by Pfeifer and Hendricks (160) for total ion current,  $I$ :

$$I = (S_C) (F_r)^v (E)^{\epsilon} (\sigma)^n \quad (3.4)$$

where  $S_C$  is a constant which depends on the dielectric constant and the surface tension of the solvent (160), the electric field at the capillary tip is  $E$ , the flow rate (volume/time) is  $F_r$ , and the conductivity of the solution is  $\sigma$ . The conductivity of the solution can be expressed in terms of the equivalent molar conductivity of the electrolyte,  $\lambda_m^o$ , and the concentration,  $C$ , of the electrolyte (160). This expression is shown as Equation 3.5.

$$\sigma = \lambda_m^o \times C \quad (3.5)$$

The exponents in equation 3.4 were predicted theoretically by Pfeifer and Hendricks (160) and experimentally determined by Kebarle et al. (178) ( $\nu = 0.57$  and 0.5;  $\epsilon = 0.43$  and 0.5; and  $n = 0.43$  and 0.2-0.3 theoretical (160) and experimental (178) values, respectively). Since the exponents are small, the change in total ion current with respect to change in the flow rate, applied spray needle electric field and the concentration of the sample are very small. This current is usually in the range of 0.1 to 1  $\mu\text{A}$ . Higher currents generally result from an electric discharge (178).

To evaluate the ES onset values for the ESI source developed in our laboratory,  $V_{on}$  for several methanol/water solvent systems was calculated using Equation 3.3. Values obtained were compared with experimental  $V_{on}$  obtained by electrospraying various methanol/water compositions. Table 3.1 lists the theoretical and the experimental values obtained along with surface tension for each solvent system. To obtain the experimental  $V_{on}$  values a Helium-Neon (He-Ne) laser was focused on the tip of the spray needle and the spray was visually observed. In addition to visual observation of the spray, ion current was measured at the desolvating capillary. As shown in Figure 3.11, ion current at the desolvating capillary was measured as a function of the voltage applied to the spray needle, until a stable reading is observed. A Keithly model 610C electrometer was used in all ion current

Table 3.1 Comparison of calculated and experimental  $V_{on}$  values.

methanol/water (V/V)	Surface tension <sup>1</sup> , $\gamma$ (N/m)	Calculated $V_{on}$ (kV)	Experimental $V_{on}$ (kV)
100/0	0.0727	3.651	4.415
75/25	0.0464	2.917	3.755
50/50	0.0353	2.544	3.230
20/80	0.0273	2.237	2.945
100	0.0226	2.036	2.680

1. *Handbook of Chemistry and Physics* 64<sup>th</sup> ed.; CRC Press: Boca Raton, FL, 1984, Page F-33.

In Column 3,  $V_{on}$  values were calculated using Equation 3.3 and the parameters:  $r_c = 2.0 \times 10^{-4}$  m,  $d = 6.0 \times 10^{-3}$  m and  $\epsilon_0 = 8.8 \times 10^{-12} \text{ } \mu\text{C}^2\text{m}^{-1}$

measurements. The spray needle potential, which gave a stable ion current measurement and a stable spray was assigned as the experimental  $V_{on}$ . These results indicated that a stable electrospray required 600 - 800 V above the  $V_{on}$  calculated using Equation 3.4. From the  $V_{on}$  values given in Table 3.1, one would predict that with methanol a stable electrospray should be obtainable before an electric discharge takes place, but for pure water this will not be the case. This observation is further supported by the studies of Hayati et al. (179). They suggested that a stable electrospray could only be obtained when the conductivity of the solution is between  $10^{-8}$  to  $10^{-10}\Omega^{-1}m^{-1}$ . The conductivity of distilled water is ca.  $6 \times 10^{-4}\Omega^{-1}m^{-1}$ , which is higher than the required conductivity for a stable spray.

The requirements of sample solubility and electrospray stability limit the range of solvent systems that can be used in ESI/MS experiments. Several studies have investigated the performance of electrospray ionization with respect to the sample concentration (179-181) and solution composition (182-183). Results from these earlier studies indicate that a concentration of  $10^{-5}$  M or less leads to optimal performance of an ESI source. In addition to the values listed in Table 3.1, results from Kebarle et al. (178) and Guevremont et al. (182-183) suggest that a 50/50 methanol/water solution works best for many ESI experiments. When a sample is less soluble in water or methanol, methanol can be maintained at 50%

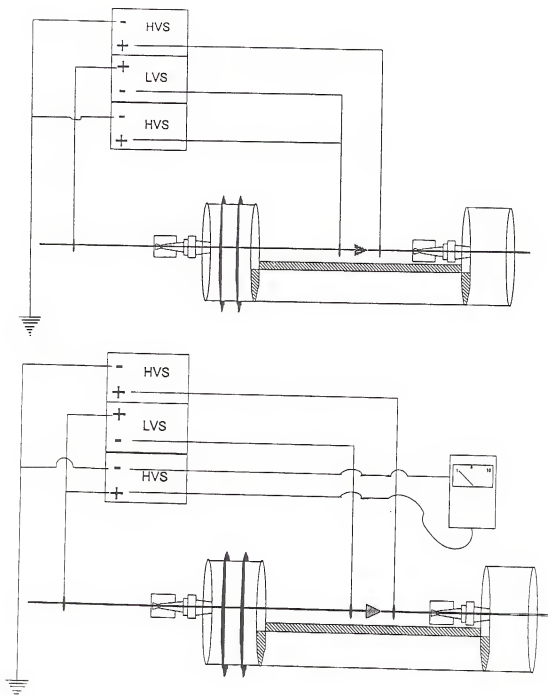


Figure 3.11 A schematic representation of the electrical connections to the spray needle and the desolvating capillary during (top) ESI/FTICR experiments or detection of ion beam current on the skimmer and (bottom) detection of ion current on desolvating capillary away from the magnetic field.

composition and the composition of the water reduced below 50% with addition of an organic solvent (toluene, methylene chloride, or acetonitrile) which can dissolve the sample. We used 50/50 methanol/water solution and ca.  $1 \times 10^{-5}$  M sample concentration in all internal ESI experiments discussed in this dissertation.

The sample solution flow rate, the potential applied to the spray needle, and the distance between the spray needle and the desolvating capillary were optimized by electrospraying a 50/50 methanol/water solution of  $1.0 \times 10^{-5}$  M Rhodamine 6G perchlorate. Internal ESI experiments discussed in this dissertation involved sample solution delivery to the spray needle through 2.5 m long (1 mm o.d. and 0.6 mm i.d.) Teflon tubing. The Teflon tubing was connected to a 5 ml Hamilton Gastight series Lur-Lok syringe. Continuous infusion of the sample to the spray needle was achieved by a Harvard Apparatus Model 22 syringe pump. The total ion current was measured as shown in Figure 3.11. Visual observation of the spray produced by the dye solution was much easier than the spray produced by the pure methanol/water solution. Several series of experiments were performed as a function of the distance between the spray needle and the desolvating capillary. In each series, total ion currents were measured varying the solution flow rate and the potential applied to the spray needle. For example,

results obtained with separations of 5, 6, 7 and 10 mm are shown in Figures 3.12 - 3.15, respectively. As shown in these plots, for separations less than 7 mm, a stable electrospray was observed when the spray needle potential was maintained between 3.25 and 5.5 kV. At potentials above 5.75 kV an electric discharge began which disrupted the electrospray process. When the distance separating the spray needle and the desolvating capillary was greater than 7 mm, stable electrospray operation required a potential greater than 4 kV on the tip of spray needle. Separations greater than 7 mm allowed the spray needle potential to be raised as high as 8 kV. In addition, separations greater than 7 mm required higher solution flow rates to achieve a stable electrospray. Visual observation of the spray indicated that increasing the spray needle potential (above 5.25 kV) increased the Taylor cone angle and decreased the length of the spray. This resulted in a wider spray which did not reach the entrance of the capillary. Usually, an electric discharge began following a pulsating spray emission. These pulsating sprays emitted larger droplets than the steady sprays. These results also indicated that a separation of 6 mm between the spray needle and the capillary and a flow rate of 4  $\mu\text{L}/\text{min}$  were the optimum parameters for the internal ESI source constructed in our laboratory.

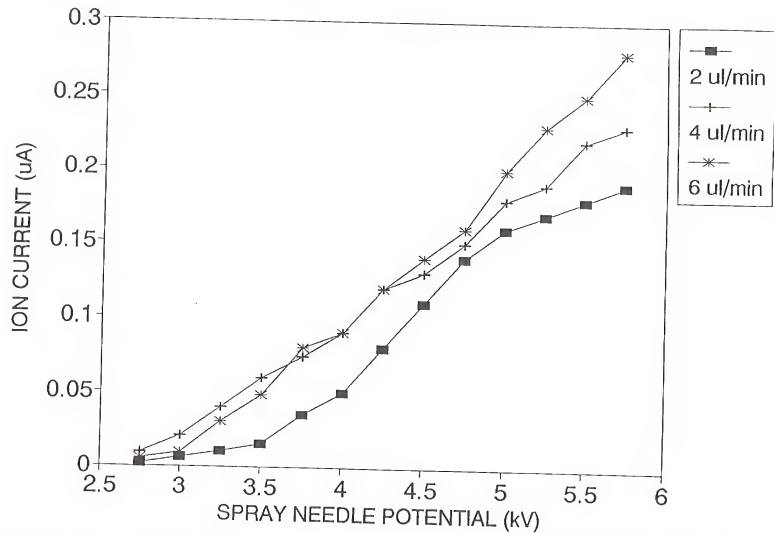


Figure 3.12

A plot of ion beam current detected at the desolvating capillary vs. the spray needle potential with respect to sample solution flow rate corresponding to a distance of 5 mm between the spray needle and the desolvating capillary.

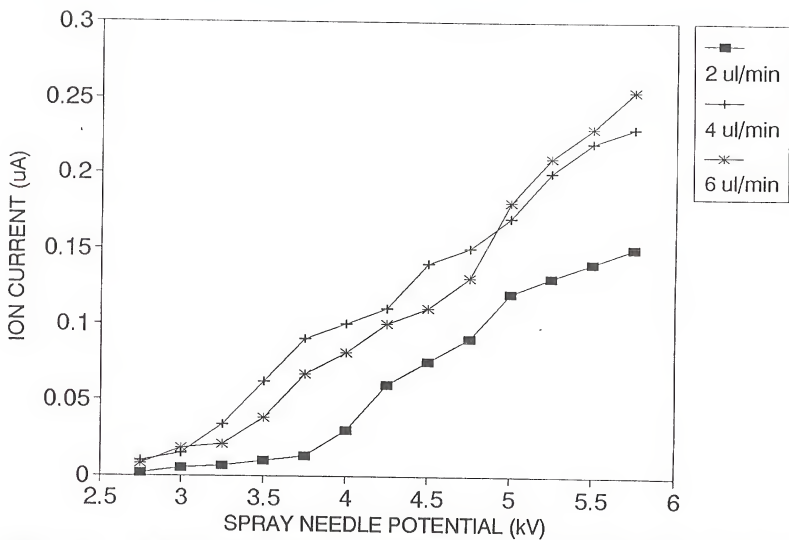


Figure 3.13

A plot of ion beam current detected at the desolvating capillary vs. the spray needle potential with respect to sample solution flow rate corresponding to a distance of 6 mm between the spray needle and the desolvating capillary.

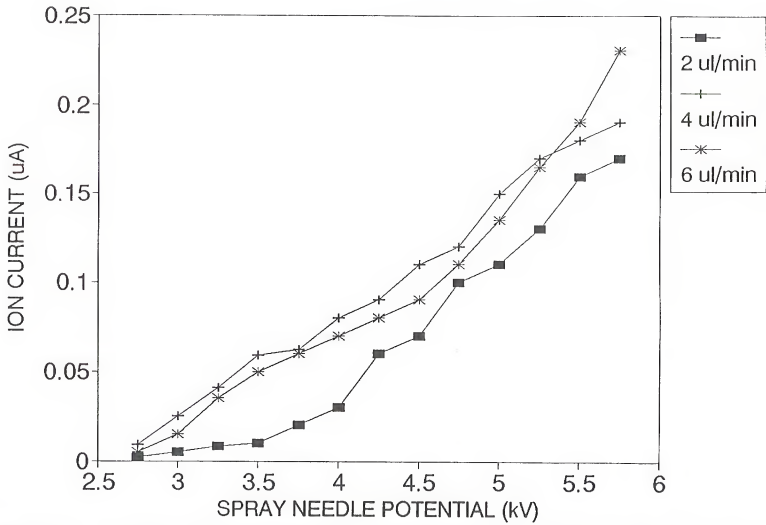


Figure 3.14

A plot of ion beam current detected at the desolvating capillary vs. the spray needle potential with respect to sample solution flow rate corresponding to a distance of 7 mm between the spray needle and the desolvating capillary.

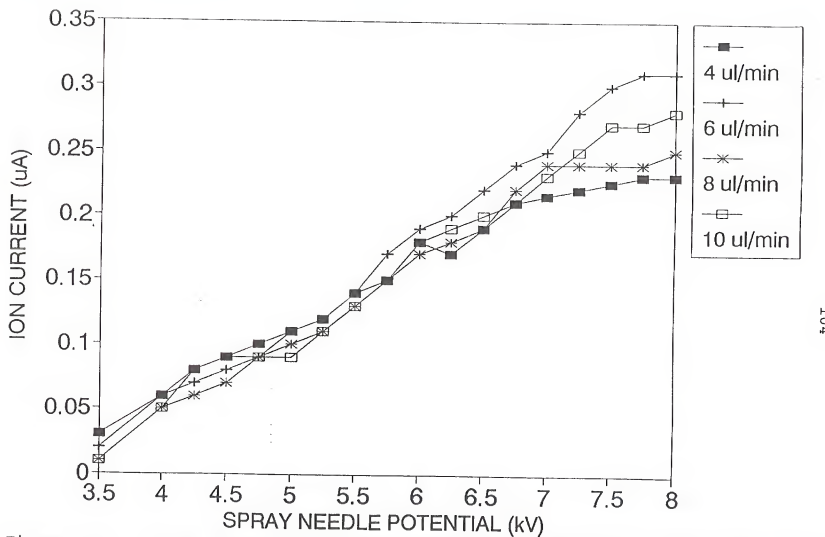


Figure 3.15

A plot of ion beam current detected at the desolvating capillary vs. the spray needle potential with respect to sample solution flow rate corresponding to a distance of 10 mm between the spray needle and the desolvating capillary.

Optimization of the Desolvating Capillary

The capillary plays a major role in the production of gas phase electrosprayed ions. Solvent evaporation from the charged droplets depends on heat transfer to the droplet from the high pressure gases in capillary and collisions with the capillary wall. First, the performance of the electrospray source was evaluated away from the magnetic field in a test chamber. As shown in Figure 3.16, a four-way cross with 7 cm flanges was used as the vacuum chamber. Two 25 L/s mechanical pumps were connected to opposite ports of the four-way cross and the pressure in the capillary exit region was maintained at ca. 3-10 Torr. The 1.9 cm o.d. x 1.7 cm i.d. electrospray probe (total length was 180 cm) and a 1.3 cm o.d. x 1.1 cm i.d. (total length 15 cm) tube in which a feedthrough was welded for ion current measurements were introduced from the other two opposing ports. A 1.2 cm diameter x 0.5 mm thick brass disc was attached to the 1.3 cm o.d. probe's feedthrough to monitor the ion current produced by the beam exiting the capillary. The 1.3 cm o.d. probe and the electrospray probe were inserted through 1.3 cm and 1.9 cm diameter vacuum interlock probe ports, respectively. This allowed us to manipulate both probes along the z-axis and obtain the optimum separation between the capillary exit and the brass disc.

As shown in Table 3.2, ion current, pressure in the capillary exit region, current required to resistively heat

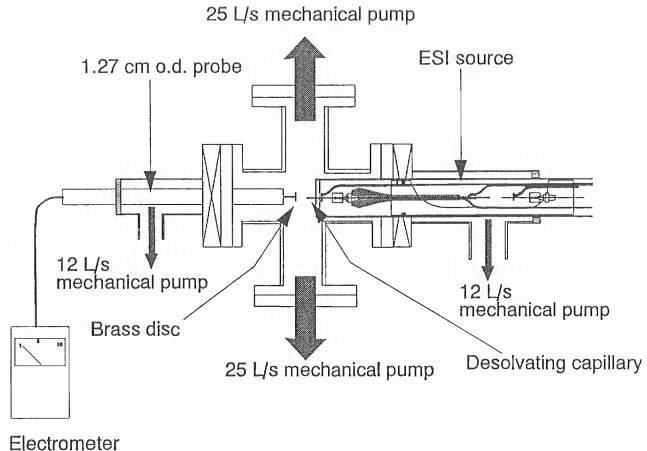


Figure 3.16 A schematic representation of the vacuum chamber used in detecting the ion beam current exiting the capillary without the magnetic field

Table 3.2 Results from optimization of the desolvating capillary.

I.d. of the 15 cm long desolvating stainless steel capillary (mm)	Ion current due to ions exiting the capillary (nA)	Pressure in the capillary exit region (Torr)	Current required to resistively heat the capillary to 100 °C (A)	Ion current due to ions exiting the 0.35 mm orifice skimmer (pA)
0.350	1.0	1.2	1.8	8
0.500	1.0	2.1	2.2	10
0.580	1.0	2.8	3.1	15
0.687	1.0	4.1	4.0	18
0.840	1.2	5.5	4.5	12
1.000	2.5	8.4	5.5	10

the capillary to 100 °C and the profile of the ion beam exiting the capillary were monitored with respect to capillary radius. Initial experiments varying the desolvating capillary length suggested that a capillary with a length of 15 cm or greater was required for complete desolvation of the droplets at 100 °C. Since the capillary must be positioned within the high magnetic field of the FTICR mass spectrometer in order to use the magnetic field to assist in focusing the ions exiting the capillary, use of capillaries longer than 15 cm was not possible. A 15 cm long desolvating capillary allowed us to position it in the 0.5 to 1.8 Tesla region of the 2 Tesla magnet. Thus, all internal ESI experiments presented in this dissertation were performed with a 15 cm long desolvating capillary.

Results listed in Table 3.2 were obtained by electrospraying a 50/50 methanol/water solution of  $1.0 \times 10^{-5}$  M Rhodamine 6G perchlorate. "ESI source II" was used in this series of experiments. Even though increasing the capillary radius increased the ion current detected on the brass disc, visual observation of the stains made by the Rhodamine 6G indicated that capillaries with i.d.'s greater than 0.585 mm produced a non-uniform beam at the exit of the capillary. Capillaries with i.d.'s  $\leq 0.585$  mm produced circular stains with diameters of 0.3-0.5 mm and the capillaries with i.d.'s  $> 0.585$  mm produced stains consisting of filled circle surrounded by a second circle.

To further investigate the ions exiting the capillary, a 2.5 m long, 1.3 cm o.d. x 1.1 cm i.d. stainless steel tube with a high-voltage feedthrough welded into one end was used. A 3.5 mm o.d. x 4.5 cm long brass pin was welded to the high-voltage feedthrough. The pin was insulated using a piece of heat-shrink except for a 5 mm region at its end which was left uncovered to measure the ion current. This probe allowed us to measure the ion current along the z-axis of the FTICR mass spectrometer without breaking the vacuum and then to determine where most of the ions were lost during transfer from the ESI source to the analyzer cell. The high voltage feedthrough was connected to an electrometer to measure the ion current. As shown in Figure 3.17, the middle laser window on the 20.3 cm flange was removed and a 1.3 cm vacuum interlock probe port was mounted on the 7 cm flange. To allow the probe pin to extend within 5 mm from the entrance of a 0.35 mm orifice skimmer both trap plates were removed from the cell assembly and two delrin guides were mounted on the 20.3 cm flange to position the 1.3 cm o.d. probe in the center of the 15 cm vacuum chamber. The probe extended through both cell MACOR spacers and up to the second conductance plate. The insulated brass pin extended through both 4 mm conductance plate orifices and to a final position 5 mm from the skimmer entrance. Ion currents due to ion beam exiting the skimmer were measured for all the capillaries listed in column one of Table 3.2, and the results are listed in column five. Results

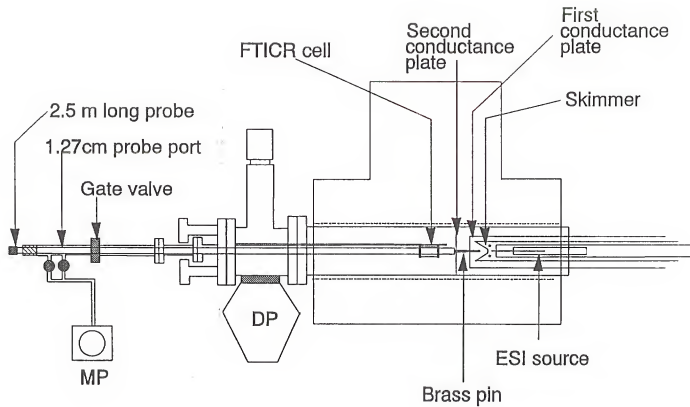


Figure 3.17 A schematic representation of the internal ESI/FTICR mass spectrometer modified to accommodate the 2.5 m long probe which was used in monitoring the ion beam current along the z-axis.

indicate that the 0.687 mm i.d. capillary would be the ideal choice. However, this size capillary required more than 4 A of current for resistive heating to 100 °C and the pressure in the capillary/skimmer region was ca. 4.1 Torr. Presence of high pressure in the capillary/skimmer region increased the pressure in the cell region to  $5.0 \times 10^{-6}$  Torr and hampered the FTICR detection process. Even though using a capillary with an i.d. of 0.585 mm reduced the ion current from 18 to 15 pA, we were able to achieve ca.  $4.7 \times 10^{-7}$  Torr in the cell region. In addition, replacing the 0.35 mm orifice skimmer with a 0.2 mm skimmer allowed us to maintain the pressure in the cell region at ca.  $2.0 \times 10^{-7}$  Torr.

To optimize the potential applied on the desolvating capillary, initial experiments were performed using the values suggested by Laude et al. (85) for their internal electrospray source. Their results suggested that the desolvating capillary should be biased as high as 330 V for optimum operation of the internal ESI source. Although initial experiments were performed biasing the desolvating capillary between 100 to 500 V, careful optimization of our internal ESI source allowed us to bias the desolvating capillary between 1-28 V and transfer ions into the capillary - skimmer region effectively.

Optimization of the Skimmer/Lens Holder Assembly

Usually, 0.1-0.15  $\mu$ A of current was detected at the capillary entrance and only 1-1.5 nA was transported through the 0.585 mm i.d. x 15 cm long capillary and detected on the skimmer. Passing through the skimmer resulted in about 10 - 15 pA behind the skimmer. Further transport of the ions from the skimmer to the analyzer was achieved efficiently using the high magnetic field of the FTICR mass spectrometer. Typically, 70-75% of the ion current detected behind the skimmer could be transferred into the analyzer cell. Thus, the alignment of the skimmer orifice with the ESI source, focusing of the beam exiting the capillary, and the pressure in capillary exit/skimmer region are important factors which can affect ion transfer from the source to the FTICR analyzer cell.

In an effort to achieve maximum transfer from the source to the analyzer cell, three different skimmer holder designs were tried in our laboratory. As shown in Figure 3.18 the first design was built to accommodate the "ESI source I". The holder was fabricated from a 4.1 cm o.d. x 5.4 cm long delrin rod. Except for a 9.5 mm region in the front, the rest of the 5.4 cm delrin rod was machined to give a 2.5 cm o.d. x 1.8 cm i.d. cylinder. Several slots/holes were machined on the cylindrical surface to insure good pumping in the capillary/skimmer region. A 9.5 mm thick V-shaped guide with

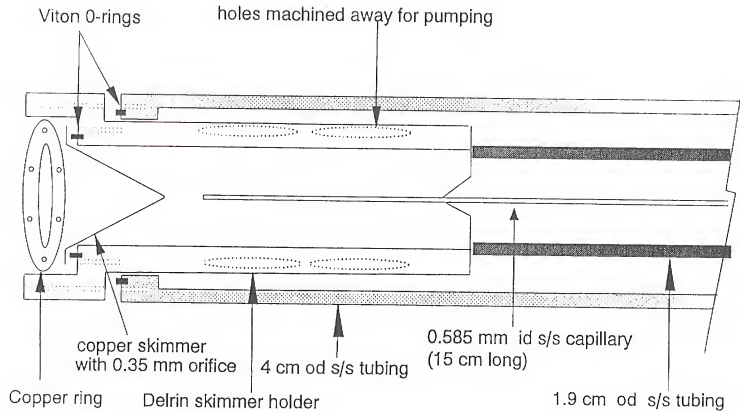


Figure 3.18 A schematic representation of the first design adopted in constructing the skimmer holder.

a 0.9 mm orifice allowed the capillary to enter the skimmer holder with less difficulty. The delrin skimmer holder was inserted into the 4.1 cm o.d. stainless steel tubing which served as the first differentially pumped region. As shown in Figure 3.18, this skimmer holder design required more than 4 cm of the 15 cm long desolvating capillary to be introduced into the assembly to align the skimmer orifice with the capillary exit orifice. Thus, this design minimized the capillary length which could be heated directly. In addition, this design did not prevent the capillary from further entering the skimmer holder and damaging the skimmer. When the capillary (25-400 V) was close (within 1-2 mm) to the skimmer orifice (4-15 V), discharge between the capillary and the skimmer was observed. A similar discharge problem between the capillary and the skimmer was reported by Turecek et al. (184). During one series of experiments, the capillary came in contact with the skimmer and allowed the current which was applied to the capillary in order to heat it to flow through the skimmer, ultimately softening and melting the skimmer holder.

To circumvent the problems experienced with the first design, a second skimmer holder was fabricated using a 4.1 cm o.d. x 7.1 cm long delrin rod. As shown in Figure 3.19, this skimmer holder was designed to accommodate "ESI source II". This design allowed the 1.9 o.d. cm probe to extend 3.0 cm inside the skimmer holder. When the capillary was protruding

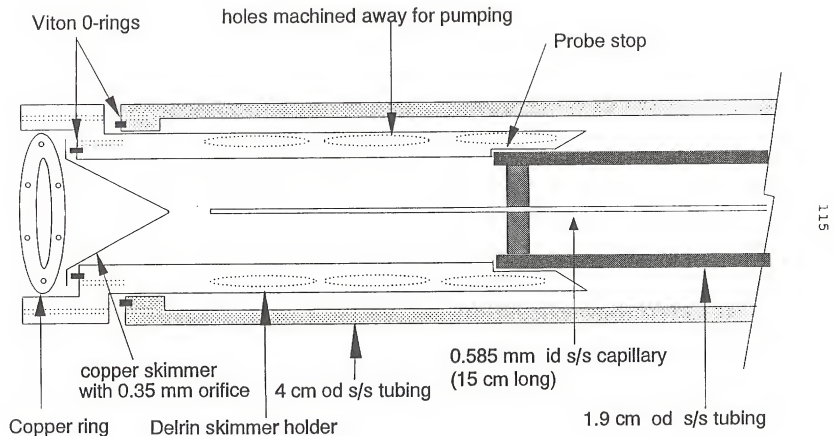


Figure 3.19 A schematic representation of the second design adopted in constructing the skimmer holder.

2.0 cm from the end of the 1.9 cm probe, a distance of 2 mm separated the capillary from the skimmer. This skimmer holder and "ESI source II" allowed us to perform most of the optimization experiments. Initial studies involved electrospraying a 50/50 methanol/water solution of  $1.0 \times 10^{-5}$  M Rhodamine 6G perchlorate. In addition to ion current measurements, visual observation of the stains made by the dye helped with alignment of each component in directions perpendicular to the z-axis. Such observations indicated that the beam exiting the capillary had a diameter greater (0.5 mm) than the skimmer orifice (0.35 mm). This prompted us to add a cylindrical electrode (tube lens) between the capillary exit and the skimmer entrance. The position of the tube lens along the z-axis was determined using the results shown in Figure 3.20. The thickness and the position along the x and y axes were optimized using SIMION ion trajectory simulations. Figures 3.21-3.22 show SIMION trajectories calculated for 10 ions with 10 eV kinetic energy and a distance of 8 mm separating the capillary and the skimmer. Figure 3.21 shows a SIMION plot of electrostatic field and ion trajectory calculations in the capillary-skimmer region without and with the tube lens. In Figure 3.22, the effect of the tube lens is minimized and the effect of the magnetic field on the ions exiting the capillary is demonstrated using SIMION trajectory calculations. These results indicated that the combination of both the magnetic field and the tube lens effectively focused the beam exiting the capillary.

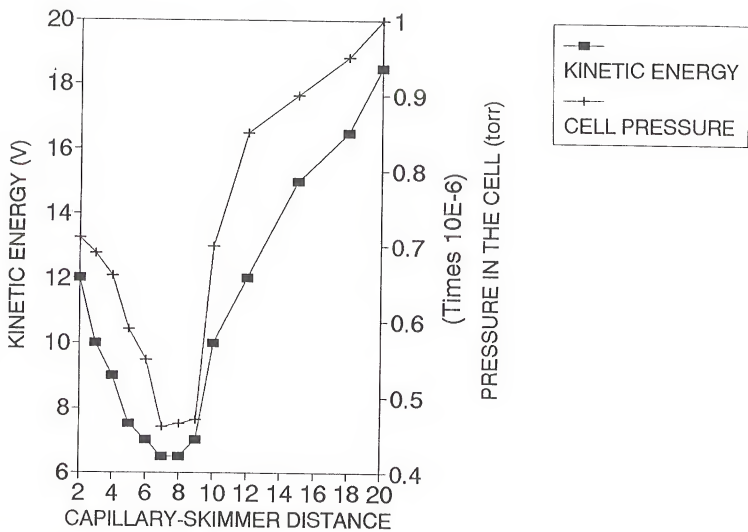
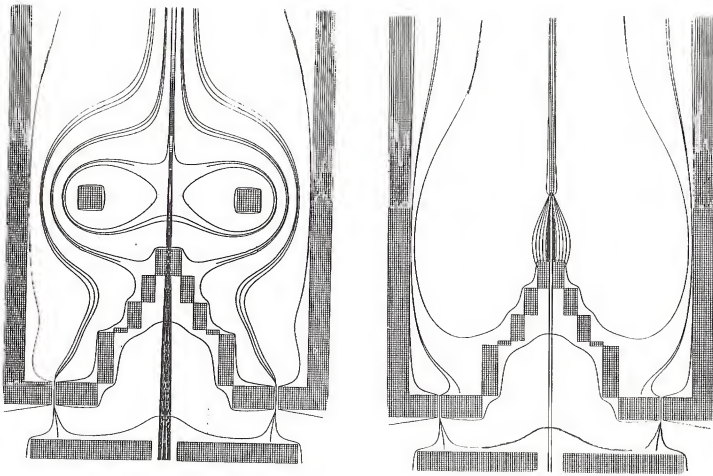
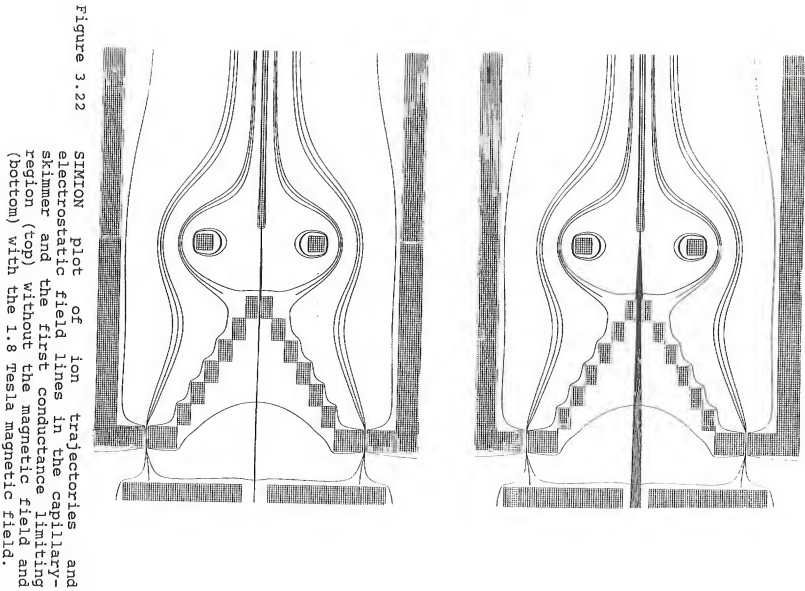


Figure 3.20 A plot of ion kinetic energy and pressure in the cell region as a function of the distance between the desolvating capillary exit orifice and the skimmer entrance.

Figure 3.21 SIMION plot of ion trajectories and electrostatic field lines in the capillary-skimmer and the first conductance limiting region: (top) without the tube lens and (bottom) with the tube lens.





**Figure 3.22** SIMION plot of ion trajectories and electrostatic field lines in the capillary-skimmer and the first conductance limiting region (top) without the magnetic field and (bottom) with the 1.8 Tesla magnetic field.

To accommodate the tube lens, a third skimmer holder was fabricated using the same dimensions as the second design. As shown in Figure 3.23, a 1.7 cm o.d. x 6.4 mm thick MACOR disc was placed in front of the tube lens to further guide the capillary. When the 1.9 cm o.d. probe was flush with the probe stop bevel (4 mm between the skimmer and the capillary) and the capillary protruded 2 cm from the end of the probe the tube lens was positioned 1.8 cm from the end of the capillary. Guided by SIMION calculations, a 2.4 mm tube lens was fabricated from stainless steel with a 1.8 cm o.d. and 1.4 cm i.d..

#### Optimization of the Capillary-Skimmer Distance

The factor found to be most important in controlling both ion kinetic energy and FTICR analyzer cell pressure is the distance between the capillary exit and the skimmer entrance. Pressure is observed to vary significantly with even a small change in the capillary-skimmer distance because changing the capillary position changes the position of the skimmer with respect to the (pseudo) supersonic expansion and changes the region that is being sampled.

When gas molecules and ions expand from an atmospheric pressure region (spray needle-desolvating capillary) through a pinhole nozzle (0.585 mm capillary) into a vacuum chamber (capillary-skimmer region), a supersonic jet is formed (18).

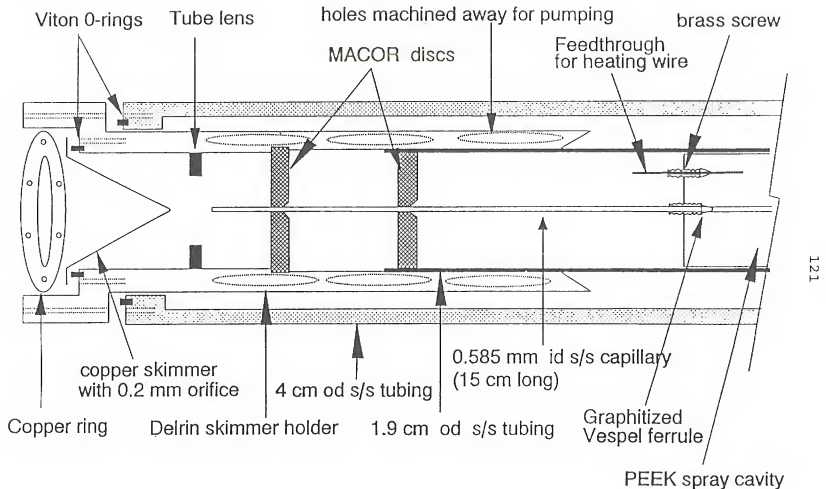


Figure 3.23    A schematic representation of the **third** design adopted in constructing the skimmer holder and the ESI source positioned inside it.

If we consider the expanding free jet in the absence of magnetic field and electric field lines, the expansion can be schematically illustrated as shown Figure 3.24. As shown in the figure, expansion into the vacuum chamber through the desolvating capillary exit is characterized by velocity equalization of background gas molecules and ions in the free jet rather than a Maxwellian velocity distribution. The equalization of velocities in the jet occurs in a region termed the "silent zone", which terminates at a certain distance from the capillary exit. This distance is usually referred as the "Mach distance" or "Mach disk" (185). The Mach distance ( $M_d$ ) can be calculated using Equation 3.6.

$$M_d = 0.67 D_{cap} (P_{cap}/P_{c-s})^{0.5} \quad 3.6$$

where  $D_{cap}$  is the i.d. of the capillary,  $P_{cap}$  is the pressure in the capillary exit region and  $P_{c-s}$  is the pressure in the capillary-skimmer region. Equation 3.6 suggests that  $M_d$  is a factor which is determined by the pumping speed available in the capillary - skimmer region. Thus, a small pump or skimmer holder with limited pumping can result in a shorter  $M_d$ . Our skimmer holder was designed with several slots for good pumping to satisfy this criteria.

Since gas flow through the capillary is too large for the vacuum pumps to handle, the central portion of the beam is sampled into the next vacuum region by using a skimmer (186)

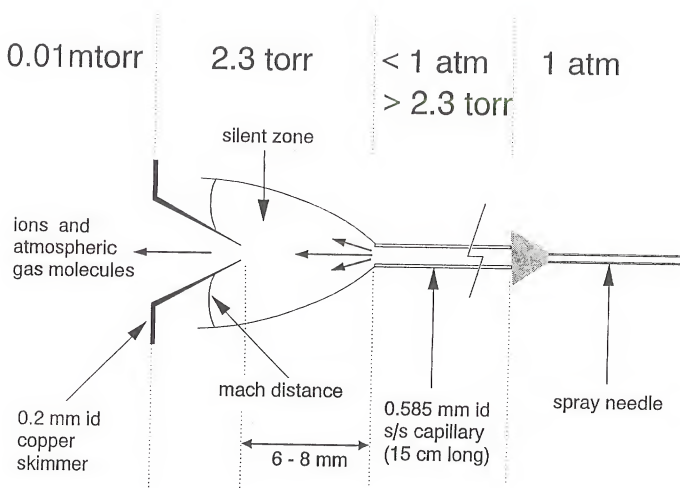


Figure 3.24

A schematic representation showing the expansion of molecules and ions at near atmospheric pressure from the desolvating capillary into the capillary-skimmer region. Sampling of molecules and ions with the skimmer orifice positioned at the mach distance and within the silent zone (magnetic and electrostatic fields are absent).

as shown in Figures 3.24-3.26. As shown in Figure 3.24, when the expanding beam is sampled from the silent zone and closer to the mach distance, the ions and gas molecules continue their movement in a straight line through the skimmer. The directional effect of the molecular beam makes the gas flow through the skimmer efficient. Thus, extraction and focusing of the beam sampled in this region can be achieved with minimum ion loss. On the other hand, if the skimmer is placed farther from the mach disk, outside the silent zone (pulling the 1.9 cm probe out, Figure 3.25) or inside the silent zone (probe pushed closer to the skimmer, Figure 3.26), ions and background gas molecules can undergo extensive scattering and make the focusing of the ions more difficult.

In one series of experiments the distance between capillary exit and the skimmer entrance was varied between 2 and 20 mm and the pressure in the analyzer cell and the kinetic energy of the ions transmitted to the cell were determined. Kinetic energy of the ions was determined by measuring the ion beam current on the back trap plate using an electrometer while applying a dc potential to the front trap plate. The potential required to drop the ion beam current to zero was assigned as the (maximum) kinetic energy of the ions entering the FTICR cell. Figure 3.20 illustrates the effect of the kinetic energy of the ions and the pressure in the cell region with respect capillary-skimmer distance. These results indicate that optimum distance between the capillary and the

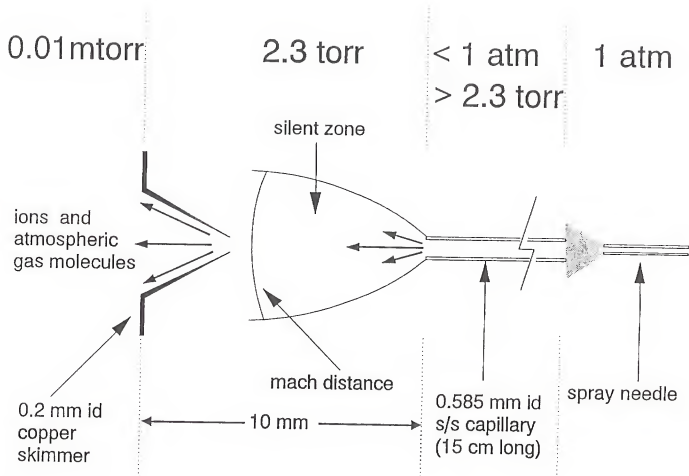


Figure 3.25

A schematic representation showing the expansion of molecules and ions at near atmospheric pressure from the desolvating capillary into the capillary-skimmer region. Sampling of molecules and ions with the skimmer orifice positioned away from the mach distance and outside the silent zone (magnetic and electrostatic fields are absent).

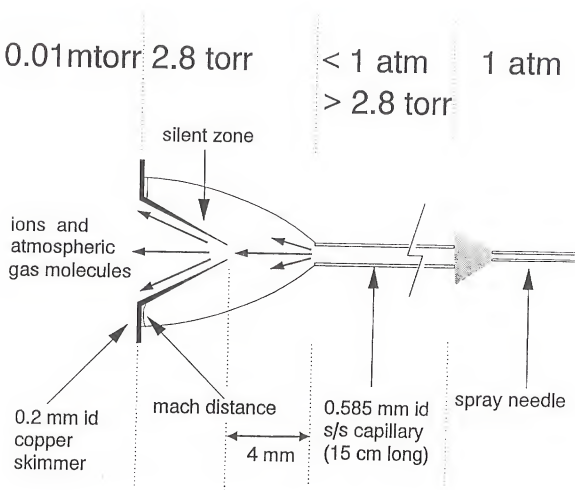


Figure 3.26

A schematic representation showing the expansion of molecules and ions at near atmospheric pressure from the desolvating capillary into the capillary-skimmer region. Sampling of molecules and ions with the skimmer orifice positioned away from the mach distance and within the silent zone (magnetic and electrostatic fields are absent).

skimmer is in the range of 6-8 mm and a separation of 7 mm gave the absolute pressure minimum in the analyzer cell ( $M_d$  calculated using equation 3.6 is ca. 7.1 mm). Similar experiments varying the distance between the capillary and skimmer were performed by Hofstadler et al. (182). In their ESI/FTICR mass spectrometer the pressure minimum in the analyzer cell corresponded to a distance of 3 to 5 mm between the skimmer and the capillary.

Our results further indicated that the skimmer potential may play a role in determining the kinetic energy of the ions reaching the cell. When the optimum distance between the capillary and the skimmer is used, the potential required to stop the ion current reaching the front trap closely matched the skimmer potential. A series of experiments was performed to further investigate the dependence of the trapping potential on the skimmer potential and the results are described below. Kinetic energy experiments were performed by detecting the ion current on the front trap plate (stainless steel plate covering the mesh) while varying the potential applied to the second conductance limiting orifice. As shown in Figures 3.27-3.29, the results suggested that the kinetic energy of the ions is strongly dependent on the skimmer potential.

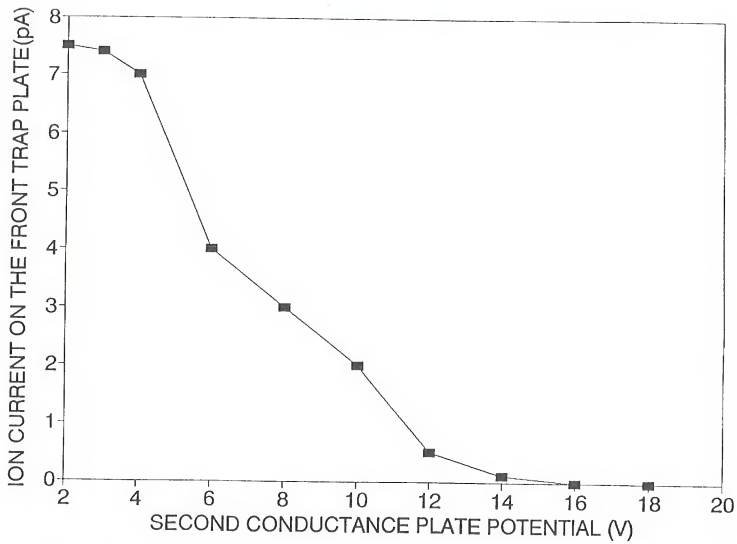


Figure 3.27 A plot of ion beam current detected on the front trap plate as a function of the potential applied to the second conductance plate obtained with skimmer biased at 10 V.

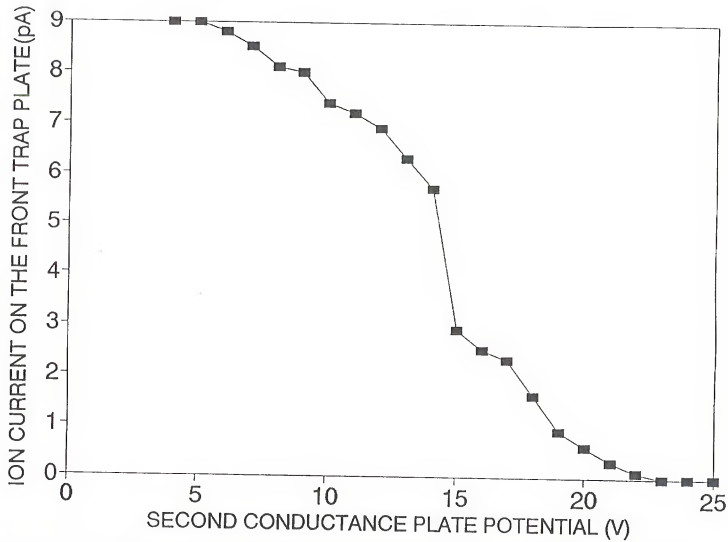


Figure 3.28

A plot of ion beam current detected on the front trap plate as a function of the potential applied to the second conductance plate obtained with skimmer biased at 15 V.

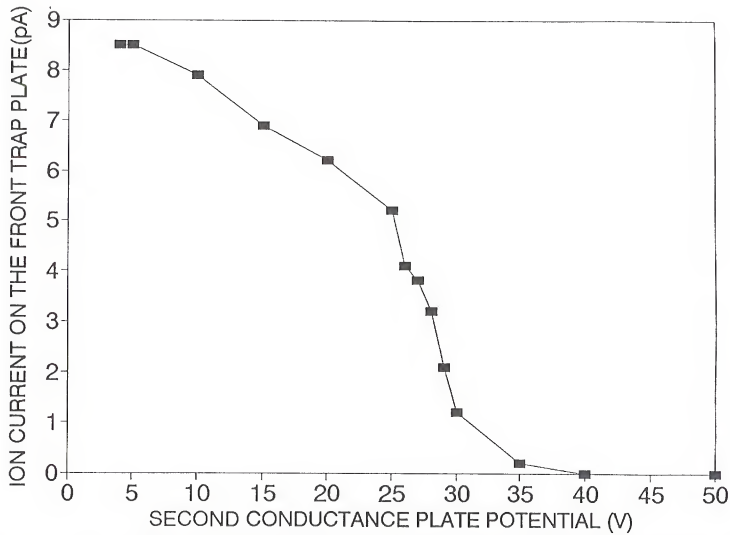


Figure 3.29

A plot of ion beam current detected on the front trap plate as a function of the potential applied to the second conductance plate obtained with skimmer biased at 30 V.

Optimization of the Trapping Versus Skimmer Potentials

With the capillary-skimmer distance optimized for the lowest pressure in the cell ( $4.7 \times 10^{-7}$  and  $3.5 \times 10^{-8}$  Torr without and with the shutter, respectively, when using the 0.2 mm orifice skimmer), typically 7 mm, the skimmer potential became the controlling factor for the ion's kinetic energy. Thus, the skimmer potential determined the trapping potential required to trap the ions in the FTICR analyzer cell.

To optimize the trapping potential with respect to skimmer potential, a series of experiments were performed by electrospraying a  $1.0 \times 10^{-5}$  M sample of  $\text{Ru}(\text{bpy})_3(\text{PF}_6)_2$  in 49/49/2 water/methanol/acetonitrile solution. Since a majority of the work described in this dissertation involves organometallic complexes, one of these was chosen for this series of experiments. The capillary-skimmer distance was optimized for the lowest pressure in the analyzer cell and an experiment was performed varying the skimmer potential. For each skimmer potential the total ion intensities of the molecular and fragment ions were monitored with respect to trapping potential and the results are shown in Figures 3.30 - 3.32 (where m/z 715, 285, 207 and 157 corresponds to  $[\text{Ru}(\text{bpy})_3(\text{PF}_6)]^+$ ,  $[\text{Ru}(\text{bpy})_3]^{2+}$ ,  $[\text{Ru}(\text{bpy})_2]^{2+}$ , and  $[(\text{bpy})+\text{H}]^+$ , respectively). These figures demonstrate the ability of this interface to change the skimmer potential to trap electrosprayed ions at any desired trapping potential. Our

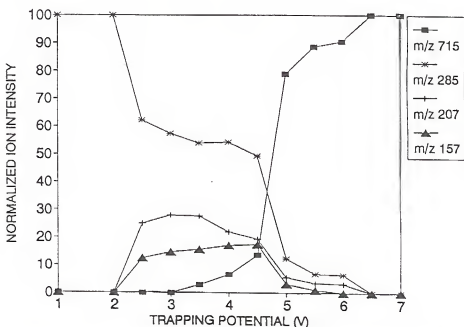
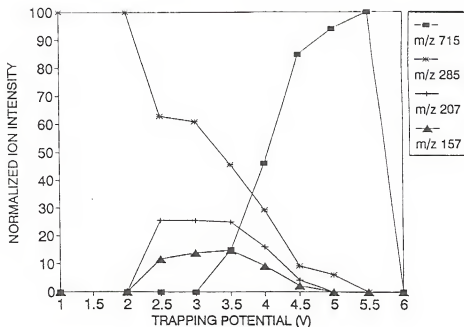


Figure 3.30 Trapping profile of electrospray ions produced from  $1 \times 10^{-5}$  M  $\text{Ru}(\text{bpy})_3(\text{PF}_6)_2$  in 48/48/2 methanol/water/acetonitrile solution corresponding to a skimmer potential of (top) 3 V and (bottom) 4 V.

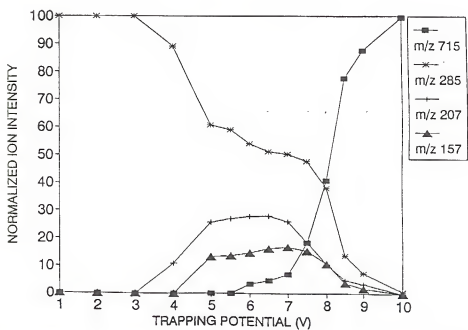
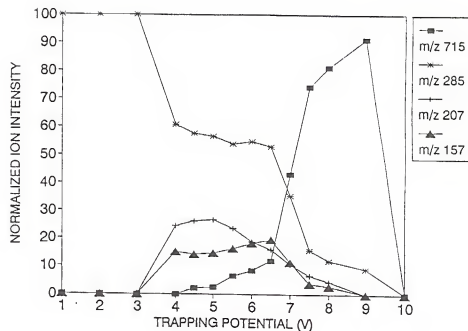


Figure 3.31 Trapping profile of electrospray ions produced from  $1 \times 10^{-5}$  M  $\text{Ru}(\text{bpy})_3(\text{PF}_6)_2$  in 48/48/2 methanol/water/acetonitrile solution corresponding to a skimmer potential of (top) 6 V and (bottom) 7 V.

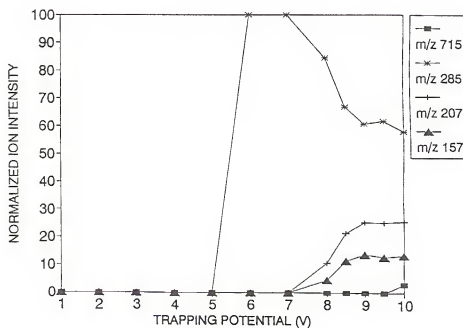
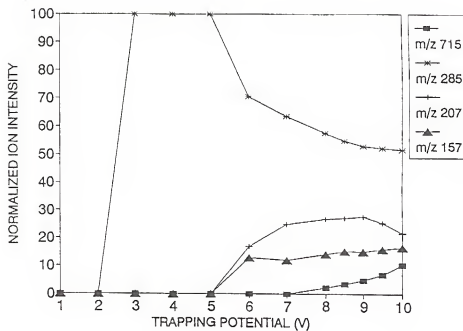


Figure 3.32 Trapping profile of electrospray ions produced from  $1 \times 10^{-5}$  M Ru(bpy)<sub>3</sub>(PF<sub>6</sub>)<sub>2</sub> in 48/48/2 methanol/water/acetonitrile solution corresponding to a skimmer potential of (top) 10 V and (bottom) 12 V.

results indicated that the optimum potential for trapping all the ions including parent and daughter ions is equal to the skimmer potential. However, maximum trapping of the doubly charged parent ion is achieved when the trap plates are held at 1/2-1/3 of the skimmer potential. Our trapping profile results for ESI-generated doubly charged ions agree with the results obtained by Laude et al. (86). However, their study failed to provide any information on trapping the CID fragments produced in the capillary - skimmer region.

#### Unstable Spray Due To Heat Transfer

When experiments were carried out for more than four to six hours, ion beam current measured on the back trap plate was observed to be unstable. In addition, detecting the ion beam current on the skimmer and the capillary further confirmed this observation. Careful optimization and cleaning the spray needle and the desolvating capillary did not help to produce a steady ion beam current. However, flowing the sample solution at 15 to 20  $\mu\text{L}/\text{min}$  produced a steady ion beam current. This indicated that the pulsation was due to a sample solution delivery problem to the spray needle. When intermittent spray was observed, the electrospray probe was removed from the vacuum chamber and the spray was observed away from the magnetic field on a table. Observations indicated that the sample solution in the Teflon tubing was

being heated before being delivered to the spray needle. This may have been due to heat transfer from the desolvating capillary to the 1.9 cm o.d. probe and subsequent heat transfer to the Teflon tube and the sample solution. To circumvent this problem a 3.2 cm o.d. copper tube was coiled inside the 1.9 cm o.d. probe and positioned behind the spray assembly. This allowed us to flow water around the Teflon tubing which carried the sample solution and keep it at room temperature. Thus, a steady flow of sample solution was delivered to the spray needle, which allowed us to operate at 4  $\mu\text{L}/\text{min}$ .

#### High Magnetic Field Shutter

Several problems were encountered during the coupling of internal ESI source with the FTICR mass spectrometer. Perhaps the most serious was the inability of this design to attain required low pressures for FTICR excitation and detection events. To circumvent the problems with high pressures, we installed a shutter on the first conductance plate.

The shutter and the electronics to control it are shown in Figures 3.33-3.34. The shutter consists of a wedge shaped shutter head (Delrin), two brass rods, two stainless steel screws and an "L" shaped Delrin support. The combined length of the brass rods and the shutter head was kept less than 2.5 cm (the distance separating the first and second conductance

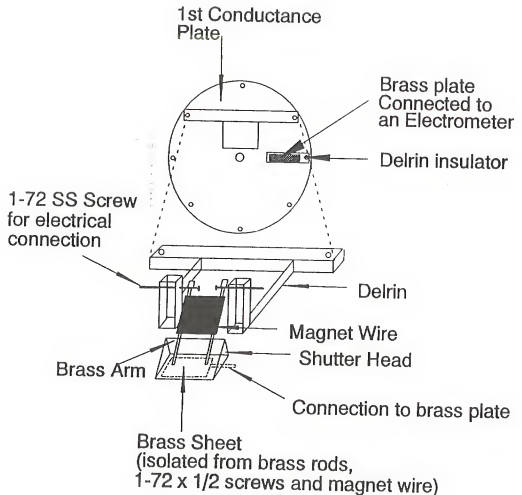


Figure 3.33 A schematic representation of the high magnetic field shutter used with the internal source ESI/FTICR mass spectrometer.

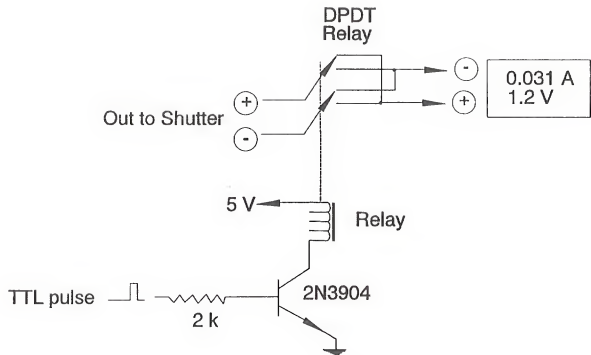


Figure 3.34 A schematic representation of the electrical circuit used to control the high magnetic field shutter.

limit), so the shutter could function without physical interference by the second conductance limit. A brass sheet was recessed into the front side of the shutter head to measure the ion current. The brass rods were pivoted on the "L" shaped delrin support by the stainless steel screws, which served as the electrical connection points for the magnet wire.

The solenoid was created by winding 13.8 m x 0.127 mm polyurethane coated magnet wire around the two brass rods as shown in Figure 3.33. The length and thickness of the magnet wire was determined by trial and error. The amount of current needed to create the electromagnetic field necessary to open the shutter, clearing the conductance limit, was kept at a minimum by increasing the number of windings. Using fewer windings or a thicker magnet wire required more current to open the shutter completely and caused the delrin shutter head to soften or melt due to heating of the magnet wire. Using the same principle, a shutter with one brass rod was tried but too many windings around a small area caused the magnet wire to break due to over-heating.

When current was not applied to the solenoid the shutter stayed in the closed position due to gravity, but it did not make a tight seal against the first conductance plate. Pressure in the cell region was still reduced to  $8.5 \times 10^{-8}$  Torr, which was lower than the pressure attained without the shutter ( $2.0 \times 10^{-7}$  Torr). Applying a current (0.031 A and

1.2 V) in one direction created a magnetic field with the same polarity as the 2 Tesla superconducting magnet. Thus, the solenoid attempted to align against the 2 T field and sealed against the first conductance plate. This mode of shutter closure reduced the pressure in the cell region to  $3.5 \times 10^{-8}$  Torr. A TTL pulse from the data station through the electronic circuit allowed the direction of the current applied from the power supply to be reversed for the duration of the pulse. Reverse flow of current allowed the shutter to be open for ion injection from the ESI source for the duration of the reverse current pulse (pressure rose to ca.  $2.0 \times 10^{-7}$  Torr).

In addition to reducing the pressure, the ability to measure the ion current passing through the 1<sup>st</sup> conductance limit on the closed shutter head allowed us to optimize the electrospray source conditions for maximum ion current. To demonstrate the improvement in performance of our 2 Tesla ESI/FTICR mass spectrometer, mass spectra of Ru(bpy)<sub>3</sub>(PF<sub>6</sub>)<sub>2</sub> ( $1.0 \times 10^{-5}$  M 49/49/2 methanol/water/acetonitrile solution) obtained with and without the shutter are shown in Figure 3.35 and 3.36, respectively.

#### Conclusions

This chapter described the successful development of a concentric tube vacuum assembly, which allowed an ESI source

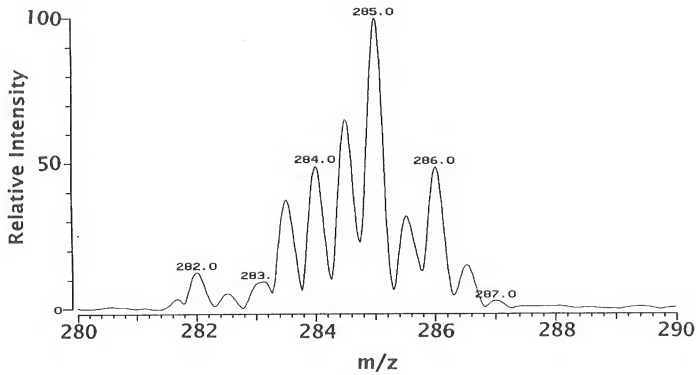


Figure 3.35 ESI/FTICR mass spectrum of  $\text{Ru}(\text{bpy})_3(\text{PF}_6)_2$  obtained without the shutter using  $1 \times 10^{-5}$  M 49/49/2 methanol/water/acetonitrile solution and detected using the broadband mode (15–1000 Da).

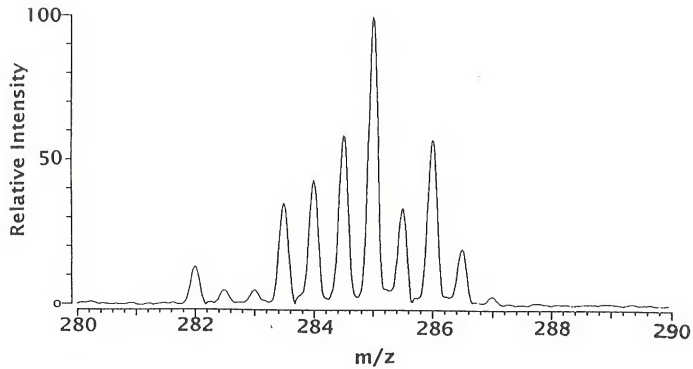


Figure 3.36 ESI/FTICR mass spectrum of  $\text{Ru}(\text{bpy})_3(\text{PF}_6)_2$  obtained with the shutter using  $1 \times 10^{-5}$  M 49/49/2 methanol/water/acetonitrile solution and detected using the broadband mode (15–1000 Da).

to be placed 24 cm from the FTICR analyzer cell. Initial studies involved electrospraying Rhodamine 6G perchlorate, which allowed us to perform ion current measurements along the z-axis as well as visual observation of the stains made by the dye. The latter helped with alignment of each component in directions perpendicular to z-axis. Experiments varying the sample solution flow rate indicated that a flow rate of 4  $\mu\text{l}/\text{min}$  is sufficient for 6 mm separation between the spray needle and capillary. Experiments performed to optimize the spray needle potential suggested that a stable spray was obtained when the onset voltage was maintained 600 to 800 V higher than the calculated onset potential (Equation 3.3)

Comparison of the ESI source designs indicated that "ESI source IV" could be used routinely without any difficulties for producing gas phase ions from less volatile samples. This design allowed us to heat the desolvating capillary to above 175 °C without melting or softening the spray assembly. In addition, this design allowed us to achieve much lower pressure in the capillary-skimmer region than the previous designs and minimized the collision induced dissociation in this region (chapter 4). Distances of 6 and 7 mm between the spray needle-capillary and the capillary-skimmer, respectively, were optimum for most of the experiments.

A third design for the skimmer holder with a tube lens between the skimmer and the desolvating capillary helped in focusing the ion beam exiting the capillary. In addition, a

MACOR disc in the skimmer holder greatly helped in aligning the capillary exit orifice with the skimmer orifice.

We also demonstrated that the ions produced from this ESI source could be trapped efficiently by carefully matching the z-axis kinetic energy of the ion beam with the trapping potential. Usually a trapping potential equal to the skimmer potential trapped all the ions exiting the skimmer and a maximum trapping of the doubly charged ion was achieved with 1/3 the skimmer potential.

The shutter mounted on the first conductance plate reduced the pressure in the cell region to  $3.5 \times 10^{-8}$  Torr and improved the mass resolution. In addition, the ability of the shutter to measure the ion beam current transmitted through the first conductance limiting orifice allowed us to optimize the source conditions while the source was operational.

Optimal conditions for the efficient formation and trapping of ESI ions included application of 3.5-4 kV on the spray needle, a 25 V (variable between 15-400 depending on the product ions desired) potential on the desolvating capillary which is heated resistively to above 150 °C by 3.2 A of current, a 28 V potential on the tube lens (usually 3 V above the capillary), a variable potential of 4 to 10 V on the skimmer, grounded first and second conductance limiting plates and both trapping plate potentials matching the skimmer potential.

CHAPTER 4  
APPLICATIONS OF THE INTERNAL SOURCE ELECTROSPRAY  
IONIZATION FTICR MASS SPECTROMETER

Introduction

Mass spectrometry is a useful analytical technique which can be used in determining both molecular mass and structural information for molecules. The increased use of mass spectrometry for such studies can be attributed to the development of ionization techniques (chapter 1) which allowed intact gas-phase ions to be produced from less volatile molecules. Although several ionization techniques are capable of producing molecular ions from these compounds, electrospray ionization (ESI) has been used widely in recent years. The popularity of ESI can be traced to its multiple charging process and ability to transfer ions that are preformed in solution into the gas phase. Using ESI, mass spectra for molecules as large as  $5 \times 10^6$  Da have been recorded with a relatively simple quadrupole instrument (188).

The major focus for the application of electrospray ionization mass spectrometry has been the analysis of high molecular weight proteins and oligonucleotides (188-189). This may be due to the fact that other ionization techniques available (LD and FAB) are capable of producing ions from

moderate mass molecules. Another reason for the intense use of electrospray to study peptides and proteins is the ability to couple electrospray with any of several separations techniques, including HPLC (190) and capillary-zone electrophoresis (191), so that on-line separation and mass analysis of a protein or peptide mixture is possible.

In addition to studies involving large biological molecules, experiments by Chait et al. (192), Kebarle et al. (193-194), Guevremont et al. (195), Turecek et al. (196) and Van Berkel et al. (197-198) have suggested that in the future significant new activities in the areas of organic and inorganic electrospray mass spectrometry will be seen. These studies have shown that gas phase ion chemistry is not limited to singly charged positive or negative ions and that electrospray ionization is well suited for studying several classes of low molecular weight species that are less volatile and difficult to ionize intact by other methods. Although electrospray ionization has been applied to several types of low molecular weight molecules, progress in this area has been very slow compared to the application to peptides and proteins.

Coupling of an electrospray source with a mass spectrometer further benefits from collision induced dissociation (CID) in the region between the desolvating capillary and the skimmer (capillary/skimmer CID). The high electric field (15 - 500 V) and the high pressure (1-10 Torr)

in this region allow ions exiting the capillary to undergo many energetic collisions with the atmospheric gases present in the capillary/skimmer region. The potential applied to the capillary can be readily adjusted to provide a fine control over the level of collisional activation. Molecular ions and/or the fragments enter the mass analyzer through the orifice of the skimmer. Since the potential applied to the skimmer defines the energy of the ions entering the mass analyzer, the CID energy is taken as the potential difference between the desolvating capillary and the skimmer,  $\Delta V$  (199).

This chapter reports studies of an organic dye, a peptide and several organometallic complexes using the internal source ESI/FTICR mass spectrometer, whose development and optimization were described in chapter 3. In addition, capillary/skimmer CID was used to obtain fragmentation pathways of these ions.

#### Experimental

All experiments were performed using the 2 Tesla FTICR mass spectrometer equipped with either a Nicolet FTMS 1000 data station or an Ion Spec data station. Detailed description of this instrument is given in chapter 2. The electrospray ionization source and the concentric vacuum chamber assembly discussed in chapter 3 were utilized to obtain the results presented in this chapter.

Solution in a syringe was pumped to the syringe spray needle through 0.6 mm i.d. x 244 cm long Teflon tubing by a Harvard Apparatus syringe pump. The syringe pump was operated with a flow rate of 4  $\mu\text{L}/\text{min}$ . All the samples were  $1 \times 10^{-5}$  M in 50/50 methanol/water solution (with 1-2 drops of acetic acid or acetonitrile for peptides or organometallic complexes, respectively).

Operating parameters used with the internal source ESI/FTICR experiments were as follows: Syringe needle at 3.5-4.5 kV, Desolvating capillary at 15-500 V and resistively heated above 150  $^{\circ}\text{C}$  by a current of 3.2 to 4 A, skimmer at 10 -40 V and 6-10 V for ESI source II and IV, respectively, first conductance plate at 5-8 V and ground for ESI source II and IV, respectively, second conductance plate at 3-5 V and ground for ESI source II and IV, respectively, trap plates at 1.5 to 10 V during ion injection, 1.5 V during excitation and detection. Pulse sequences used in these experiments have been explained in chapter 2.

#### Results and Discussion

#### Application To Organic Molecules

As explained in chapter 3, it was necessary to measure ion current along the z-axis to determine where most of the ions were lost during the transfer from the source to the

cell. Rhodamine 6G perchlorate was electrosprayed both to obtain ion current information and to visually observe the stains made by the dye, which helped with alignment of each component in directions perpendicular to z-axis. Since all optimal parameters were determined using Rhodamine 6G methanol/water solution, it was necessary to evaluate how the internal ESI parameters corresponded with FTICR trapping and detection capabilities. In addition, we were able to evaluate capillary/skimmer CID using Rhodamine 6G.

An ESI mass spectrum obtained by electrospraying  $1 \times 10^{-5}$  M Rhodamine 590 in methanol/water solution is shown in Figure 4.1. The high resolution mass spectrum with  $^{13}\text{C}$  isotopes resolved is shown in the inset of Figure 4.1. As shown in this figure the mass spectrum reflected only the presence of  $[\text{M}-\text{CH}_3]^+$ . It was necessary to bias the capillary and the skimmer at 100 and 40 V, respectively to obtain detectable ion current (2-5 pA). The requirement of higher potentials on these orifices may be due to problems with alignment. In addition, initial experiments were performed using the "ESI source II", which had problems with atmospheric air leaking between Delrin/MACOR and the front Swagelok/Delrin regions. These leaks maintained the pressure in the capillary/skimmer region at 4.5 Torr or above. We speculated that the presence of high pressure gases in the capillary/skimmer region and the high potential on the capillary may have contributed to the

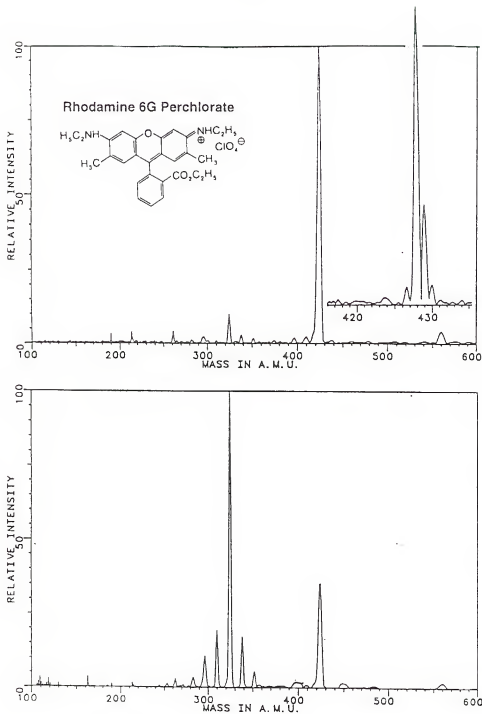


Figure 4.1 Mass spectra obtained electrospraying  $1 \times 10^{-5}$  M rhodamine 6G perchlorate in 50/50 methanol/water solution with capillary/skimmer CID energy of (top) 240 V and (bottom) 420 V. The inset shows the high resolution mass spectrum with  $^{13}\text{C}$  isotopes resolved.

loss of a  $\text{CH}_3$  group from  $M^+$ . Since the molecular ion of Rhodamine 6G at m/z 443 has been produced by laser desorption (pulsed UV light at 208 nm) and detected by FTICR methods (135), we believe that  $M^+$  can be produced using our ESI source. In fact, later experiments using the "ESI source IV" and the third skimmer holder design allowed us to detect the  $M^+$  for Rhodamine 6G at m/z 443.

As shown in Figure 4.2, capillary/skimmer CID experiments were performed on the  $[\text{M}-\text{CH}_3]^+$  ion to demonstrate the capability of the "ESI source II" to obtain structural information. When the  $\Delta V$  was 60 V (the desolvating capillary was at 100 V and the skimmer was at 40 V), collisional activation was not sufficient to dissociate  $[\text{M}-\text{CH}_3]^+$  (m/z 428). As shown in Figure 4.2, increasing  $\Delta V$  from 60 V to 420 V increases the collisional activation and produces more fragment ions. At 420 V of capillary/skimmer potential difference the most intense peak observed was due to  $[\text{M}-2\text{CH}_3-3\text{C}_2\text{H}_5]^+$  at m/z 326. Other peaks observed at 420 V of activation are shown in Figure 4.1 (bottom): m/z 355, 341, 312 and 297 correspond to  $[\text{M}-2\text{CH}_3-2\text{C}_2\text{H}_5]^+$ ,  $[\text{M}-\text{CH}_3-3\text{C}_2\text{H}_5]^+$ ,  $[\text{M}-\text{CH}_3-4\text{C}_2\text{H}_5]^+$  and  $[\text{M}-2\text{CH}_3-4\text{C}_2\text{H}_5]^+$ , respectively. These results indicate that both molecular weight and structural information can be obtained using the ESI source developed in our laboratory.

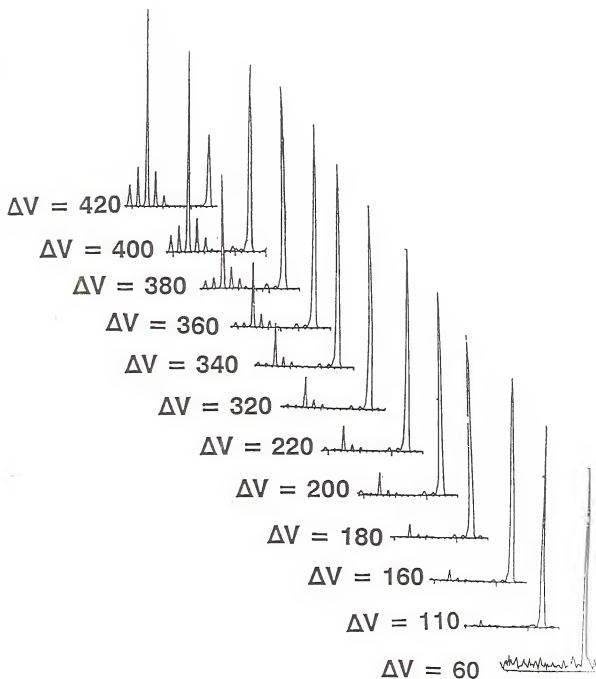


Figure 4.2 Mass spectra obtained electrospraying  $1 \times 10^{-5}$  M rhodamine 6G perchlorate in 50/50 methanol/water solution with varying capillary/skimmer CID energies.

Application To Biological Molecules

Although electrospray mass spectrometry has been used widely to study peptides and proteins, they are a most difficult and sensitive class of compounds because their ionization and charge distribution are strongly dependent on solution composition, temperature and analyte concentration (183,200). Usually, a dilute acid solution with pH between 2 to 4 is used to dissolve the protein or peptide of interest. In an acid solution, all the basic amino acid sites (arginine, lysine and histidine) on a protein sample of interest are protonated. The total charge on the protein is the difference between the number of protonated amino groups ( $-NX_2H^+$ ) and the number of ionized carboxylic groups ( $-COO^-$ ).

When an ESI source is coupled with a mass spectrometer, the multiple charging process and the ability to characterize proteins are often demonstrated using cytochrome C, albumin, myoglobin, insulin, or lysozyme. These macromolecules, with masses ranging from 5000 to 68,000 Da produce ions with charges ranging from 5 to 60, which can thus be detected in the 400 to 2000 Da range. Usually, the ability to study smaller peptides is demonstrated using either bradykinin or gramicidin S. Both peptides produce doubly and singly charged molecular ions in the 500 and 1000 Da range, respectively.

To demonstrate the capability of our source for producing multiply charged ions equine cytochrome C was electrosprayed

and detected using the FTICR mass spectrometer. A mass spectrum obtained electrospraying a  $1 \times 10^{-5}$  M equine cytochrome C (MW = 12,384) in 49.9/49.9/0.2 methanol/water/acetic acid solution is shown in Figure 4.3. This spectrum was obtained using the "ESI source II" and the third skimmer design. In 1990, McLafferty et al. (94) demonstrated that with the use of an ESI/FTICR mass spectrometer's high resolution capability, one can determine the charge state of a multiply charged molecular ion by measuring the spacing between the  $^{13}\text{C}$  isotope peaks. The inverse of the spacing corresponds to the charge state of the molecular ion. The molecular weight of an analyte of interest can be determined by multiplying the charge state by the measured mass and subtracting the mass of attached cations (usually  $\text{H}^+$ ,  $\text{Na}^+$  or  $\text{K}^+$ ). The inset in Figure 4.3 shows the high resolution spectrum obtained for the  $[\text{M}+16\text{H}]^{16+}$  state at  $5 \times 10^{-7}$  Torr (before the shutter was installed). This mass spectrum indicates that the resolution under these conditions is not sufficient to separate the  $^{13}\text{C}$  isotopes. To separate the peak at 775 from 775.0625 Da would required a mass resolution of 15,000 or better. The only way we could achieve the required resolution was by reducing the analyzer cell pressure or by increasing the magnetic field strength. In this particular case, the molecular weight of the sample is known, so the charge state can be calculated by dividing the molecular weight by the measured mass. As shown in Figure 4.3,

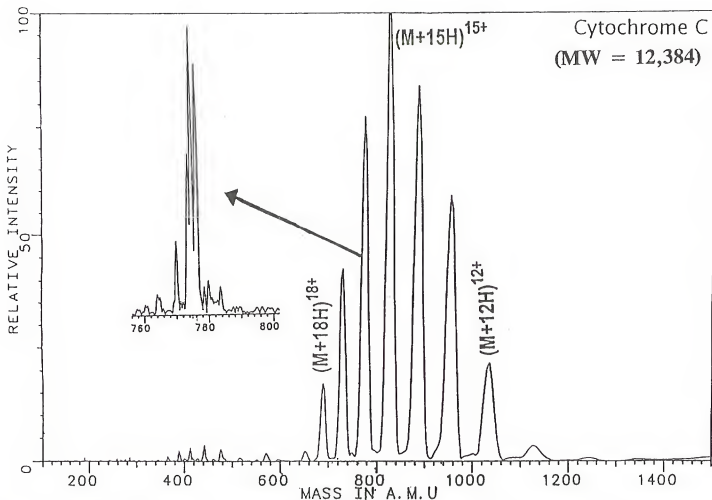


Figure 4.3 Mass spectrum obtained electrospraying  $1 \times 10^{-5}$  M cytochrome C in 49.9/49.9/0.2 methanol/water/acetic acid solution. The inset shows the high resolution mass spectrum of the charge state 16.

cytochrome C (12,384 Da) molecular ions with 11 through 19 charges were detected in mass range of 600 to 1100 Da. The distribution can be changed easily by changing the concentration of the sample or the pH of the solution (200). As discussed in chapter 3, the charge state distribution detected was very sensitive to the trapping and the skimmer potentials and the capillary/skimmer region pressure.

#### Application To Organometallic Complexes

Ruthenium complexes have been the focus of several studies owing to their relevance in photochemical molecular devices (201). In addition, ruthenium complexes have been used as shape-selective probes of nucleic acid structure (202). An important class of such compounds is that based on 2,2'-bipyridine (bpy) and 1,10-phenanthroline (phen) as bridging ligand. In addition, there is considerable interest in the design of linear polypeptides that can have stable and well-defined solution conformations. These systems are used as models for studying early events in protein folding as well as in designing peptide-based therapeutic agents (203-204). Such metallopeptides are usually designed using  $[Ru(NH_3)_6]^{X_2}$  (where X can be  $Cl^-$  or any other counter ion) complexes. For an example, a recent study by Meier et al. (205), cytochrome c molecules attached to  $Ru(NH_3)_5$  complexes were investigated for electron transfer processes.

Fast atom bombardment (FAB) mass spectrometry has been widely used for characterization of ruthenium complexes (206-207). The FAB technique usually results in singly charged ion for most metal compounds. However, there exist one or two isolated reports of doubly charged ruthenium complexes. These studies involved careful selection of an appropriate matrix or combination of matrices to produce doubly charged ions in good yield (208). Although FAB ionization has been used widely to study organometallic complexes, complicated side reactions with the matrix limited yield of multiply charged complexes and fragmentation involving loss of ligand complicate structural characterization.

To demonstrate that the internal ESI/FTICR is a powerful tool for identification and structural characterization of ruthenium complexes, we selected Ru(bpy)<sub>3</sub>(PF<sub>6</sub>)<sub>2</sub> (where bpy is C<sub>10</sub>H<sub>8</sub>N<sub>2</sub>), Ru(phen)<sub>3</sub>(PF<sub>6</sub>)<sub>2</sub> (where phen = C<sub>12</sub>H<sub>8</sub>N<sub>2</sub>) and Ru(NH<sub>3</sub>)<sub>5</sub>(C<sub>4</sub>N<sub>2</sub>H<sub>4</sub>)(PF<sub>6</sub>)<sub>2</sub>. Since these experiments were performed after installing the shutter (chapter 3), pressure in the cell region could be maintained at ca. 3.5 × 10<sup>-8</sup> Torr during FTICR ion excitation and detection events. The use of ESI source IV and the third skimmer holder design reduced the pressure in the capillary/skimmer region and enhanced the alignment between the components. This lower pressure and enhanced alignment allowed us to operate at lower capillary and skimmer potentials and minimized ion fragmentation.

Mass spectra obtained with a capillary and skimmer biased at 28 and 6 V, respectively produced minimum fragmentation. Such mass spectra obtained for  $\text{Ru}(\text{bpy})_3(\text{PF}_6)_2$  and  $\text{Ru}(\text{phen})_3(\text{PF}_6)_2$  are shown in Figures 4.4 and 4.5, respectively.

For both complexes a peak due to loss of a  $\text{PF}_6^-$  unit was observed. In addition, the doubly charged ion,  $[\text{Ru}(\text{L})_3]^{2+}$  (where L is either bpy or phen) was observed as the most intense peak for capillary voltages below 100 V (skimmer maintained at 6 V). As explained earlier, the peaks in Figures 4.6 and 4.7 occurring with half mass unit spaces as opposed to every mass unit, clearly indicate that these ions are doubly charged. To confirm this, high resolution experiments were performed and the resulting spectra were compared with theoretically simulated spectra. Such comparison for  $[\text{Ru}(\text{bpy})_3]^{2+}$  and  $[\text{Ru}(\text{phen})_3]^{2+}$  are shown in Figures 4.6 and 4.7, respectively.

The mass spectrum obtained for  $\text{Ru}(\text{NH}_3)_5(\text{C}_4\text{N}_2\text{H}_4)(\text{PF}_6)_2$  at lower capillary voltages suggested a different behavior. At lower capillary voltages, the doubly charged ion  $[\text{Ru}(\text{NH}_3)_5(\text{C}_4\text{N}_2\text{H}_4)]^{2+}$  (M) was absent from the mass spectrum and mostly complexes solvated by acetonitrile and water were observed (Figure 4.8). As shown in Figure 4.9a, it was necessary to bias the capillary to 110 V to observe any  $[\text{Ru}(\text{NH}_3)_5(\text{C}_4\text{N}_2\text{H}_4)]^{2+}$ . Increasing the capillary potential to 160 V enhanced the intensity of  $[\text{Ru}(\text{NH}_3)_5(\text{C}_4\text{N}_2\text{H}_4)]^{2+}$  (Figure

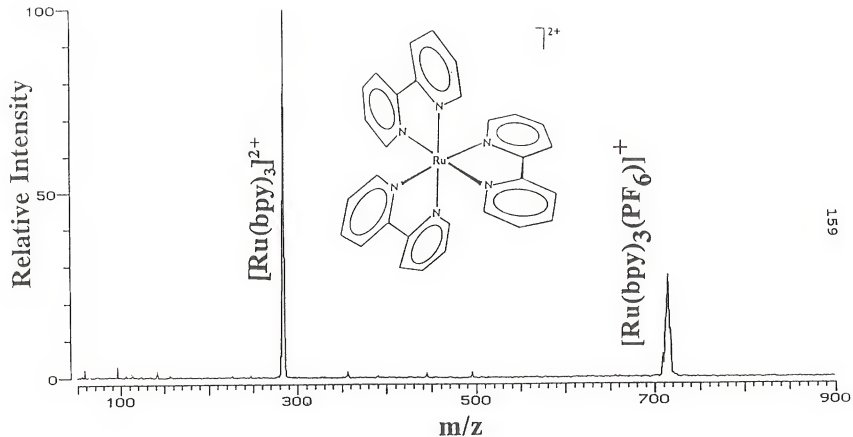


Figure 4.4 Mass spectrum obtained electrospraying  $1 \times 10^{-5}$  M  $Ru(bpy)_3(PF_6)_2$  in 49/49/2 methanol/water/acetonitrile solution (capillary/skimmer CID energy of 22 V).

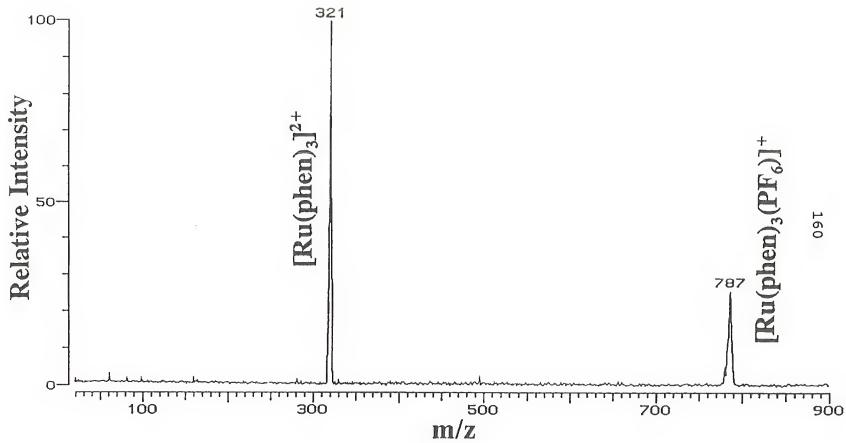


Figure 4.5 Mass spectrum obtained electrospraying  $1 \times 10^{-5}$  M  $\text{Ru}(\text{phen})_3(\text{PF}_6)_2$  in 49/49/2 methanol/water/acetonitrile solution (capillary/skimmer CID energy of 22 V).

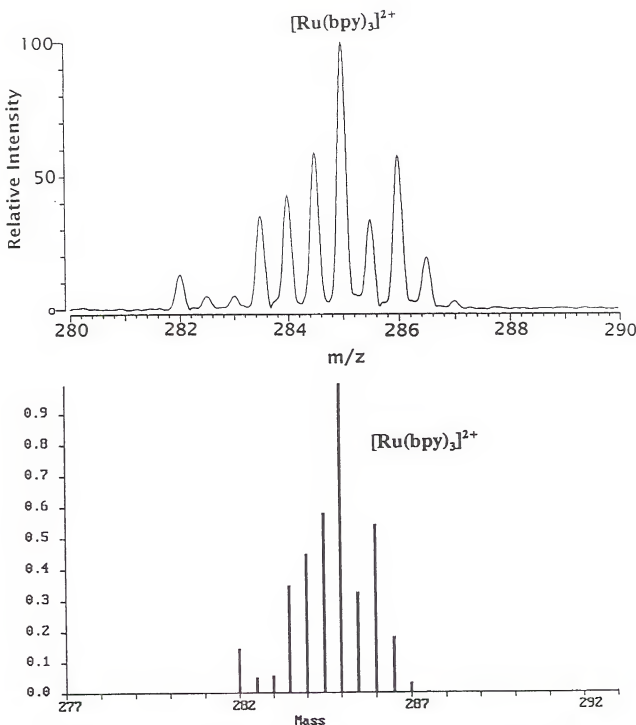


Figure 4.6 Comparison of theoretically simulated mass spectrum with experimentally obtained mass spectrum of  $[\text{Ru}(\text{bpy})_3]^{2+}$ .

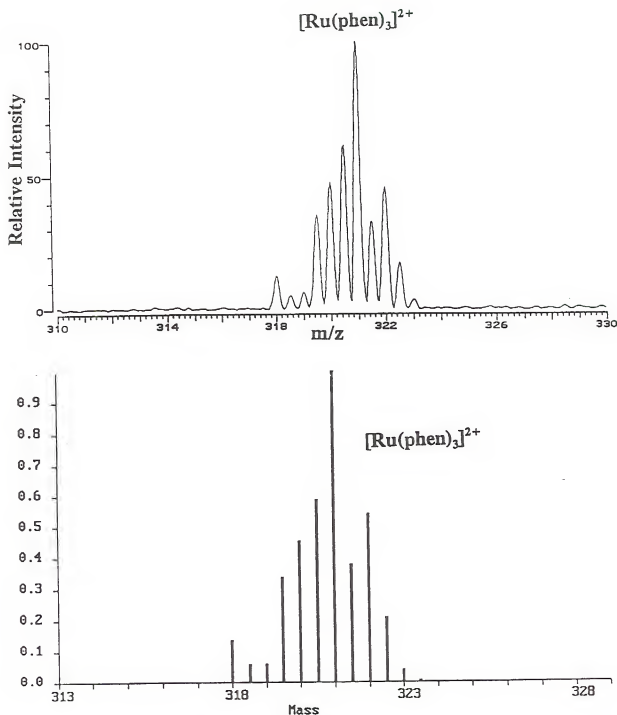


Figure 4.7 Comparison of theoretically simulated mass spectrum with experimentally obtained mass spectrum of  $[\text{Ru}(\text{phen})_3]^{2+}$ .

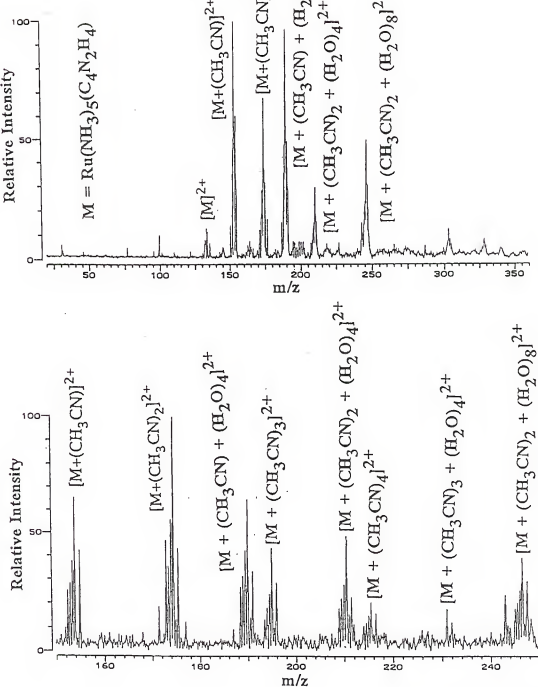


Figure 4.8

Mass spectra obtained electrospraying  $1 \times 10^{-5}$  M  $[Ru(NH_3)_5(C_4N_2H_4)](PF_6)_2$  in 49/49/2 methanol/water/acetonitrile solution with capillary/skimmer CID energy of (top) 28 V (bottom) 60 V.

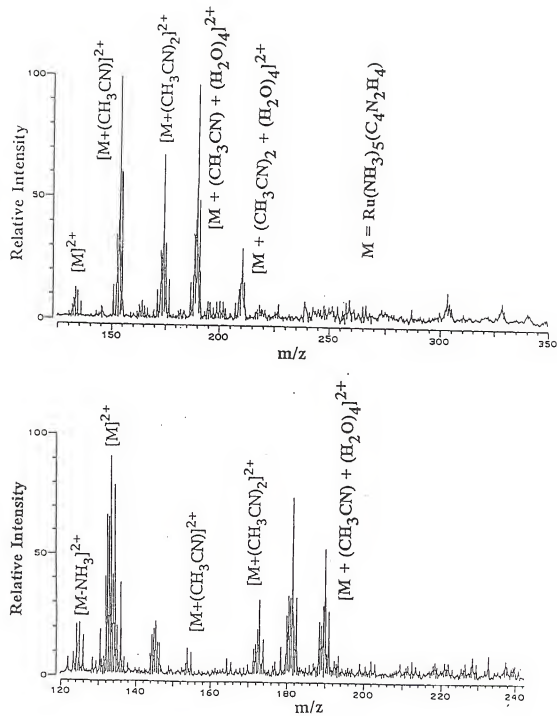


Figure 4.9 Mass spectra obtained electrospraying  $1 \times 10^{-5}$  M  $[Ru(NH_3)_5(C_4N_2H_4)](PF_6)_2$  in 49/49/2 methanol/water/acetonitrile solution with capillary/skimmer CID energy of (top) 104 V and (bottom) 154 V.

4.9b). To confirm that these ions were doubly charged, the isotope distribution pattern of  $[M+CH_3CN]^{2+}$  was compared with a simulated spectrum and the comparison is shown in Figure 4.10.

To demonstrate that capillary/skimmer CID can be used to obtain fragmentation pathways, different degrees of collisionally induced dissociation of  $[Ru(bpy)_3]^{2+}$  ( $m/z$  285) were performed and the mass spectra are shown in Figures 4.11 - 4.13. A significant benefit of this dissociation method is its simplicity and speed. Once the optimum conditions have been achieved, the entire fragmentation information can be obtained within 30 minutes. Similar capillary/skimmer CID experiments were carried out for  $Ru(phen)_3(PF_6)_2$  and the mass spectra from these capillary/skimmer CID are shown in Figures 4.14 - 4.15. The significance of these fragmentation pathways will be discussed in chapter 5.

### Conclusions

The potential of the internal source ESI/FTICR mass spectrometer has been demonstrated through its application to study of several classes of compounds. The multiple charging process in our internal ESI was demonstrated by electrospraying cytochrome c and detecting ions with 11 through 19 charges in the mass range between 600 and 1100 Da. In addition, we have demonstrated that capillary/skimmer CID can be used efficiently to remove solvent molecules from solvated ions as well as to obtain structural information through ion fragmentation pathways.

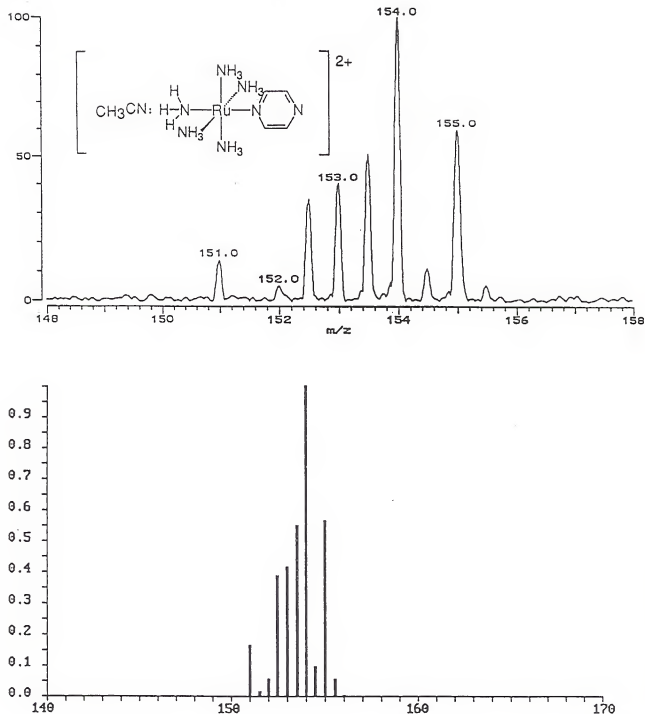


Figure 4.10 Comparison of theoretically simulated mass spectrum with experimentally obtained mass spectrum of  $[\text{Ru}(\text{NH}_3)_5(\text{C}_4\text{N}_2\text{H}_4)\text{CH}_3\text{CN}]^{2+}$ .

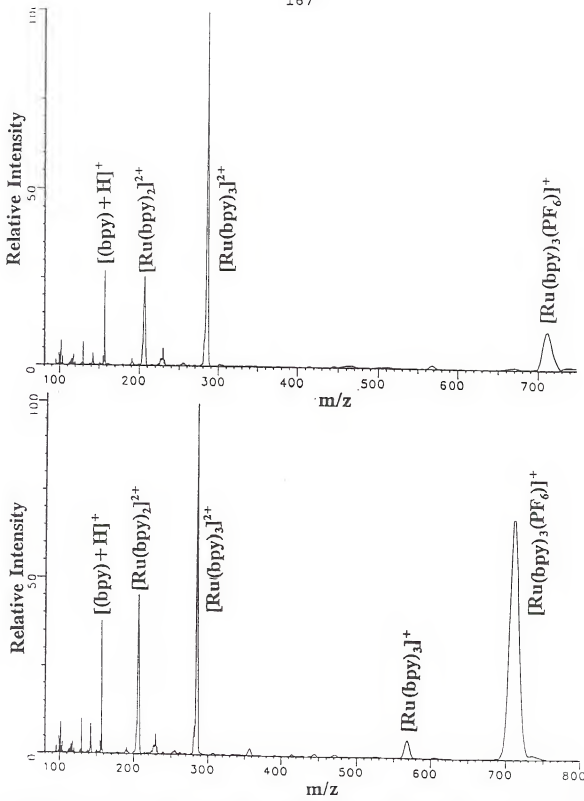


Figure 4.11 Mass spectra obtained electrospraying  $1 \times 10^{-5}$  M  $\text{Ru}(\text{bpy})_3(\text{PF}_6)_2$  in 49/49/2 methanol/water/acetonitrile solution with capillary/skimmer CID energy of (top) 94 V and (bottom) 144 V.

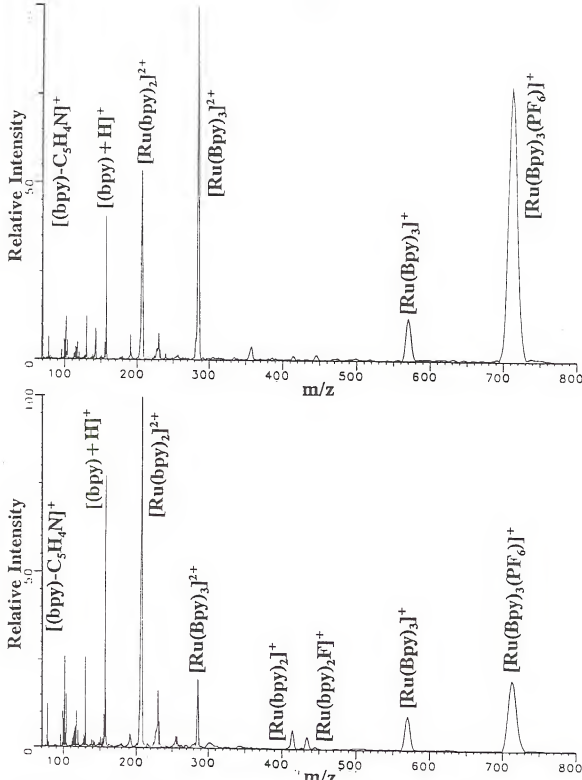


Figure 4.12 Mass spectra obtained electrospraying  $1 \times 10^{-5}$  M  $Ru(bpy)_3(PF_6)_2$  in 49/49/2 methanol/water/acetonitrile solution with capillary/skimmer CID energy of (top) 194 V and (bottom) 244 V.

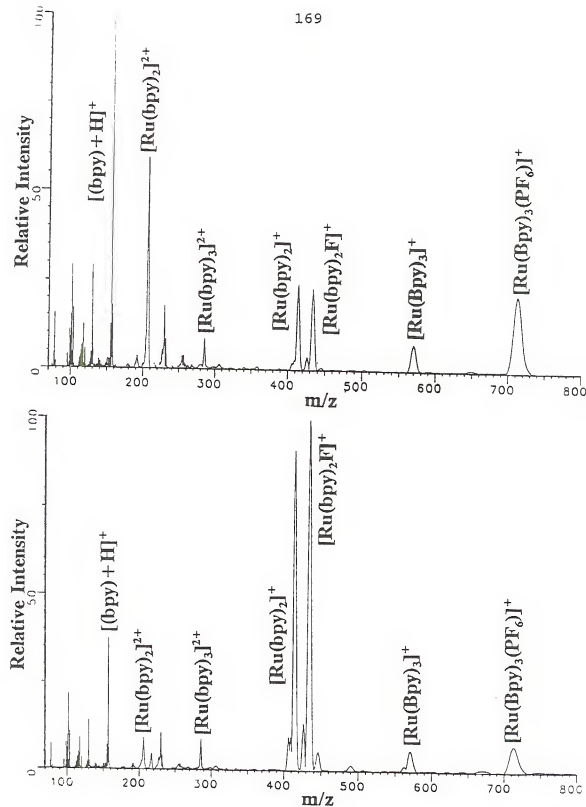


Figure 4.13 Mass spectra obtained electrospraying  $1 \times 10^{-5}$  M  $\text{Ru}(\text{bpy})_3(\text{PF}_6)_2$  in 49/49/2 methanol/water/acetonitrile solution with capillary/skimmer CID energy of (top) 294 V and (bottom) 344 V.

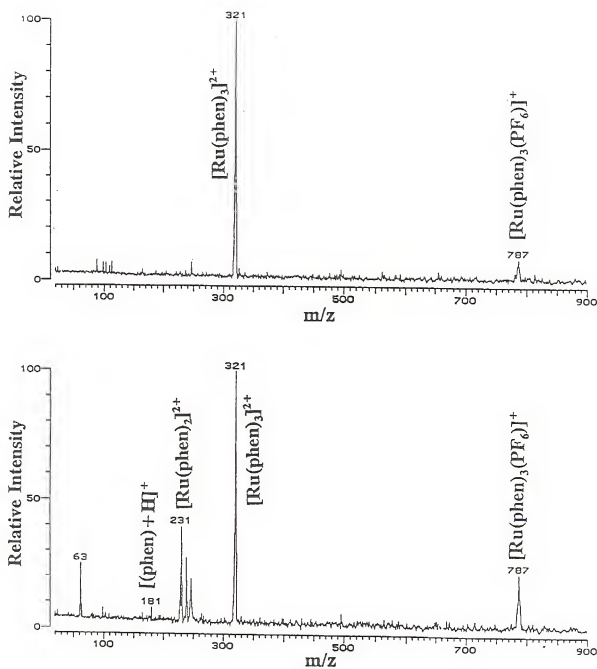


Figure 4.14 Mass spectra obtained electrospraying  $1 \times 10^{-5}$  M  $\text{Ru}(\text{phen})_3(\text{PF}_6)_2$  in 49/49/2 methanol/water/acetonitrile solution with capillary/skimmer CID energy of (top) 94 V and (bottom) 154 V.

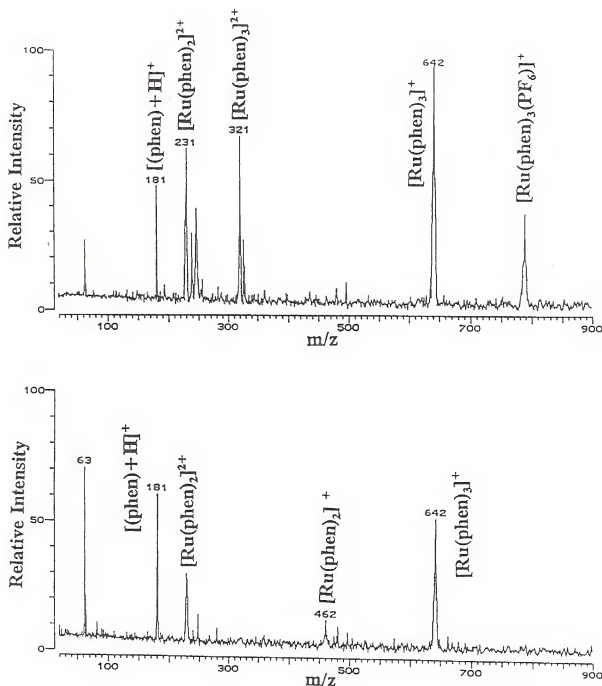


Figure 4.15 Mass spectra obtained electrospraying  $1 \times 10^{-5}$  M  $\text{Ru}(\text{phen})_3(\text{PF}_6)_2$  in 49/49/2 methanol/water/acetonitrile solution with capillary/skimmer CID energy of (top) .224 V and (bottom) 254 V.

CHAPTER 5  
APPLICATION OF THE EXTERNAL SOURCE ELECTROSPRAY IONIZATION  
FTICR MASS SPECTROMETER TO ORGANOMETALLIC COMPLEXES

Introduction

Multiple charging processes in the ESI source allow conventional mass spectrometers with  $m/z$  500 to 2000 mass ranges to detect molecular masses up to 1,000,000 daltons (209). Because electrospray ionization occurs directly from solution at atmospheric pressure, the ions formed in the gas-phase provide information on the ions in solution (210-212). Kebarle and coworkers (213) have shown that ESI/MS can provide information on ion/solvent and ion/ligand interactions of alkaline earth and transition metal ions.

We have used electron ionization (EI) routinely to form gaseous ions from organometallic complexes in our laboratories at the University of Florida. Volatile samples are introduced into the mass spectrometer through precision leak valves and less volatile samples by heating on a solids probe (214). Since fragmentation and ligand loss are common in EI, the molecular ion of interest may not be produced with this form of sample ionization (215). In addition, heating of the sample to vaporize it often leads to thermal degradation.

During the last 10-15 years, various desorption and ionization methods, such as field desorption (FD) (216), fast atom bombardment (FAB) (217), secondary ion (SI) (218), plasma desorption (PD) (219), electrohydrodynamic (EH) (220), laser desorption multiphoton ionization (221) and laser desorption (LD) (222) have been used to investigate larger, less volatile, organometallic complexes. These techniques have been compared by Hoffman et al. (LD versus FAB) (217a), Bjarnason et al. (LD versus EI) (222a), Bursey et al. (FAB versus FD) (217c) and Benninghoven et al. (SI versus PD) (218a). When using these ionization techniques, usually only singly charged species have been observed, even though the sample of interest can exist as a multiply charged ion in solution. These studies have shown that the ionization techniques employed produce quasimolecular ions ( $[M+H]^+$ ,  $[M+Na]^+$  and  $[M+K]^+$ ), can cause significant fragmentation, and produce low yields of molecular ions.

By contrast, electrospray ionization mass spectrometry (ESI/MS) produces ions directly from solution and has been shown to be an extremely soft ionization process (223). Studies by Chait et al. (210) and Kebarle et al. (213) have shown that ESI/MS can be used to generate intact parent ions of less volatile organometallic complexes. In addition, these studies have also shown that solution chemistry can be studied in the gas phase using ESI/MS. The mechanism of ion formation in the ESI source has been discussed by several researchers

(161, 224-225). They agree that the charging of the droplets occurs by an electrophoretic mechanism, but the mechanism of gas-phase ion production from charged droplets remains uncertain. The gas-phase ion production process was first proposed and investigated by Dole et al. (38), and was further investigated by Fenn et al. (226), Kebarle et al. (163) and Guevremont et al. (227).

As discussed in chapter 1, electrospray ionization sources have been successfully coupled with different types of mass spectrometers. McLafferty et al. (94) demonstrated the utility of the high mass resolution of ESI/FTICR to resolve isotopes within charge states. ESI/FTICR can be based upon an external source design with electrospray ions formed outside the magnetic field and guided with quadrupole rods or electrostatic lenses into a trapped ion cell. An alternative approach has been discussed in chapters 3 and 4.

In addition to high mass accuracy and ultrahigh mass resolution, the ability to perform collision-induced dissociation (CID) (228) or laser photodissociation in a FTICR mass spectrometer enhances its utility as an analytical tool. Electrospray ionization FTICR mass spectrometry further benefits from the ability to perform CID experiments in the capillary/skimmer region and/or in the FTICR analyzer cell. The potential difference between the skimmer and the capillary causes ions exiting the capillary to undergo energetic collisions with gases present in the capillary/skimmer region.

At low values of the potential difference intact, unsolvated ions are observed. At higher values, the desolvated cations can be dissociated to give structurally informative fragment ions (97,229). An alternative and better approach to capillary/skimmer CID involves trapping the ions inside the FTICR analyzer cell followed by CID experiments on selectively isolated ions of interest (in-cell CID). During such in-cell CID experiments one ion is isolated by ejecting all the other ions from the FTICR analyzer/reaction cell using a series of rf pulses. The isolated ion is then excited by a single rf pulse and allowed to undergo collisions with the target gas (230). The kinetic energy gained by the ion is controlled by the duration of the rf pulse and/or its amplitude (230). The ability of the FTICR mass spectrometer to trap ions for several seconds also makes it a suitable instrument for studying ion-molecule reactions. The ion of interest can be isolated as in the CID experiment, and then a reagent gas (e.g. a neutral gas of known ionization potential (IP) for charge-transfer reactions) can be introduced into the analyzer/reaction cell via a pulsed valve or precision leak valve. After a reaction delay time, the reaction products are detected.

We have been studying the reactivity of organometallic complexes in the gas phase in our laboratories at the University of Florida for the past nine years (214). Since EI and LD ionization were used in these investigations, the ions

studied were limited to singly charged positive or negative ions.

Complexes of ruthenium with polypyridyl ligands have been of great interest due to their excited-state electron-transfer and energy-transfer reactions, including photoluminescence and chemiluminescence processes (231). Specifically,  $[\text{Ru}(\text{bpy})_3]^{2+}$  was studied for its ability to convert solar power into electrical energy (232). Structural information for these complexes has been obtained from spectroscopic and electrochemical studies. Complementary mass spectrometric analysis has been limited due to low volatility of the complexes. Although FAB ionization has produced doubly charged ions for related ruthenium-bipyridyl complexes, inability to select the right matrix limited its application (233). Recently, Chait et al. (211) demonstrated the application of ESI to study  $\text{Ru}(\text{bpy})_3\text{Cl}_2$ . However, limited mass resolution prevented them from obtaining detailed fragmentation pathways.

Bis-diphenylphosphino-methane (DPM) has been widely used as a bridging ligand. The bridging capability of the DPM ligand has allowed the formation several multinuclear complexes (234). Extensive studies have been made of binuclear complexes of Rh, Ir, Pt, Au and Ag with bridging ligands due to their unique photochemical properties (235-236). The only technique available for the characterization of such DPM bridged dinuclear complexes has been  $^{31}\text{P}$  NMR

(Nuclear Magnetic Resonance) spectroscopy. However, fragmentation pathways and molecular weight information are unattainable with  $^{31}\text{P}$  NMR.

In the experiments reported here an external source ESI/FTICR was used to demonstrate the applicability of this technique to study singly and doubly charged organometallic complexes. Specifically, ESI/FTICR mass spectrometry was used to study the complexes Ru(II)(bpy)<sub>3</sub>(PF<sub>6</sub>)<sub>2</sub> (where bpy = 2,2'-bipyridyl), Ag<sub>2</sub>(DPM)<sub>2</sub>(BF<sub>4</sub>)<sub>2</sub> (where DPM = bis-diphenylphosphino-methane) and Ag<sub>2</sub>(DPM)<sub>3</sub>(BF<sub>4</sub>)<sub>2</sub>. Both capillary/skimmer and in-cell CID methods were used to obtain structural information for these complexes.

#### Experimental

All experiments were performed using a Bruker Bio-APEX 47e mass spectrometer (172) equipped with a 4.7 Tesla superconducting magnet, an external ion source, and a RF-shimmed Infinity analyzer cell (149). The basic features of the external ion source FTICR mass spectrometer and the operating parameters used in these experiments have been described in detail (chapter 2 and ref. 100). Briefly, the external ion source has two stages of differential pumping and the electrospray source has two additional stages of pumping. The electrostatic ion transfer region and the FTICR cell regions were pumped by separate 400 L/s cryopumps and the

pressure in the cell region was maintained at  $4.8 \times 10^{-9}$  Torr during the electrospray operation. An 800 L/s cryopump maintained the external ion source region pressure at  $2 \times 10^{-5}$  Torr during the electrospray operation.

The ESI/FTICR system used in these experiments was equipped with an Analytica of Branford ESI source (237). This source consists of a needle operated at ground potential, a 500 um i.d. glass capillary with metallized (platinum) entrance and exit, two skimmers, three lens elements, and counter current N<sub>2</sub> drying gas. The region between the exit end of the capillary and the first skimmer was pumped by a 25 L/s mechanical pump and the pressure in this region was maintained at 1.5 Torr. The capillary/skimmer CID experiments were performed by varying the capillary exit potential between 10 and 344 V, while holding the skimmer potential at 6 V. A second 25 L/s mechanical pump was used to pump the region between the first skimmer and the second skimmer and the pressure in this region was maintained at  $4.8 \times 10^{-2}$  Torr.

All the samples studied, (Ru(bpy)<sub>3</sub>(PF<sub>6</sub>)<sub>2</sub>, Ag<sub>2</sub>(DPM)<sub>2</sub>(BF<sub>4</sub>)<sub>2</sub> and Ag<sub>2</sub>(DPM)<sub>3</sub>(BF<sub>4</sub>)<sub>2</sub>), were synthesized as previously described (236,238). The samples (10 mg) were first dissolved in 0.3 mL of acetonitrile and then diluted with 0.8 mL of methanol and 0.5 mL of water. A 100  $\mu$ L aliquot of this 19:31:50, acetonitrile:water:methanol solution was further diluted with 900  $\mu$ L of 50:50 methanol:water before spraying. A syringe pump connected to the electrospray needle via Teflon tubing

delivered the solution with a steady flow rate of 1.2  $\mu\text{L}/\text{min}$ .

The pulse sequence employed in this experiment has been explained in detail (chapter 2 and ref. 100). An initial quench pulse evacuated all ions from the cell. During the ionization time ions were formed and transferred from the external source. Next, a post-ionization time allowed the ions to be thermalized. Ions were excited by the standard frequency chirp method, and 128 time-domain transients each containing 128 K data points were acquired during broad-band detection (100-2000 amu). For CID experiments, following the post-ionization delay, the ion of interest was isolated using a series of ion ejection sweeps. Collision-induced dissociation was carried out on the isolated ion by employing an excitation pulse of a fixed amplitude (36 V<sub>p-p</sub>), but variable duration, at the cyclotron frequency of the ion. The isolated excited ion was then allowed to collide with the collision gas for 500 ms. Air (collision gas) was introduced into the vacuum chamber to a pressure of  $5 \times 10^{-7}$  Torr above the background pressure.

### Results

To obtain structural information on the three complexes  $\text{Ag}_2(\text{DPM})_2(\text{BF}_4)_2$ ,  $\text{Ag}_2(\text{DPM})_3(\text{BF}_4)_2$  and  $\text{Ru}(\text{bpy})_3(\text{PF}_6)_2$  being studied, a series of experiments was performed using CID in the region between the capillary exit and the first skimmer.

Tables 5.1, 5.2 and 5.3 give the CID results for ions formed from  $\text{Ag}_2(\text{DPM})_2(\text{BF}_4)_2$ ,  $\text{Ag}_2(\text{DPM})_3(\text{BF}_4)_2$  and  $\text{Ru}(\text{bpy})_3(\text{PF}_6)_2$ , respectively. Figures 5.1-5.6 show the ESI/FTICR mass spectra of these complexes for two of the capillary/skimmer CID energies. Mass spectra 5.1, 5.3 and 5.5 were obtained with a CID energy of 29 V (skimmer at 6 V and capillary at 35 V) and 5.2, 5.4 and 5.6 were obtained with a CID energy of 244 V (skimmer at 6 V and capillary at 250 V). Silver and ruthenium have more than one isotope, with the most abundant isotopes of mass 107 and 102 Da, respectively. For the purpose of clarity,  $^{107}\text{Ag}$  and  $^{102}\text{Ru}$  will be used when referring to the masses of various organometallic complexes. To confirm the structural information obtained using the capillary/skimmer CID, a series of in-cell CID experiments was performed on isolated ions. Tables 5.4 and 5.5 give the in-cell CID results for  $[\text{Ag}_2(\text{DPM})_2\text{CH}_3\text{COO}]^+$  and  $[\text{Ag}_2(\text{DPM})_2]^{2+}$ , respectively; the results for  $[\text{Ru}(\text{bpy})_3]^{2+}$  are presented in Table 5.6.

#### Discussion

##### Capillary/skimmer CID

The capillary/skimmer CID is a convenient method for obtaining structural information about organometallic complexes. The presence of high pressure gases in the

Table 5.1. Capillary/Skimmer CID results for  $\text{Ag}_2(\text{DPM})_2(\text{BF}_4)_2$ 

Ions Detected (m/z)	Capillary/skimmer CID energy					
	29	74	119	154	244	344
$[\text{Ag}_2(\text{DPM})_2]^{2+}$ (491)	13 <sup>a</sup>					
$[\text{Ag}_2(\text{DPM})_2\text{BF}_4]^+$ (1069)	30	3	6	1		
$[\text{Ag}_2(\text{DPM})_2\text{CH}_3\text{COO}]^+$ (1041)	100	100	58	1	1	7
$[\text{Ag}_2(\text{DPM})_2\text{Cl}]^+$ (1017)		2	2			
$[\text{Ag}_2(\text{DPM})_2]^+$ (982)		13	100	26	2	18
$[\text{Ag}(\text{DPM})_2\text{Cl}]^+$ (910)			1			
$[\text{Ag}(\text{DPM})_2]^+$ (875)		7	7	1		
$[\text{Ag}_2(\text{DPM})\text{C}_6\text{H}_5]^+$ (675)					5	7
$[\text{Ag}_2(\text{DPM})\text{CH}_3\text{COO}]^+$ (657)			59	100	8	11
$[\text{Ag}_2(\text{DPM})\text{Cl}]^+$ (633)				1		
$[\text{Ag}_2(\text{DPM})]^+$ (598)					2	
$[\text{Ag}_2(\text{DPM})_2]^{2+}/[\text{Ag}(\text{DPM})]^+$ (491)	31					
$[\text{Ag}(\text{DPM})]^+$ (491)			24	9	100	63
$[(\text{DPM})-\text{P}(\text{C}_6\text{H}_5)_2]^+$ (199)				2	25	65
$[(\text{DPM})-\text{CH}_2\text{P}(\text{C}_6\text{H}_5)_2]^+$ (185)						82
$[(\text{DPM})-\text{P}(\text{C}_6\text{H}_5)_3\text{H}]^+$ (121)					12	100

a = Relative abundance

Table 5.2. Capillary/Skimmer CID results for  $\text{Ag}_2(\text{DPM})_3(\text{BF}_4)_2$ 

Ions Detected (m/z)	Capillary/skimmer CID energy (v)					
	29	74	119	154	244	344
$[\text{Ag}_2(\text{DPM})_3]^{2+}$ (683)	100 <sup>a</sup>	19				
$[\text{Ag}_2(\text{DPM})_3\text{BF}_4]^+$ (1453)	6	2				
$[\text{Ag}_2(\text{DPM})_3\text{CH}_3\text{COO}]^+$ (1425)	5	3				
$[\text{Ag}_2(\text{DPM})_3\text{Cl}]^+$ (1401)	6	5				
$[\text{Ag}_2(\text{DPM})_2\text{BF}_4]^+$ (1069)	3	11	13	11		
$[\text{Ag}_2(\text{DPM})_2\text{CH}_3\text{COO}]^+$ (1041)	13	27	18	8	2	5
$[\text{Ag}_2(\text{DPM})_2\text{Cl}]^+$ (1017)		7	12	12		
$[\text{Ag}_2(\text{DPM})_2]^+$ (982)			8	17	12	10
$[\text{Ag}(\text{DPM})_2]^+$ (875)	2	58	37	13	7	23
$[\text{Ag}_2(\text{DPM})\text{C}_6\text{H}_5]^+$ (675)					19	
$[\text{Ag}_2(\text{DPM})\text{CH}_3\text{COO}]^+$ (657)			5	23	27	7
$[\text{Ag}_2(\text{DPM})\text{Cl}]^+$ (633)				2	25	
$[\text{Ag}(\text{DPM})]^+$ (491)			100	100	100	100
$[\text{Ag}_2(\text{DPM})_2]^{2+}/[\text{Ag}(\text{DPM})]^+$ (491)	100					
$[(\text{DPM})-\text{P}(\text{C}_6\text{H}_5)_2]^+$ (199)				7	15	95
$[(\text{DPM})-\text{CH}_2\text{P}(\text{C}_6\text{H}_5)_2]^+$ (185)						33
$[(\text{DPM})-\text{P}(\text{C}_6\text{H}_5)_3]^+$ (121)					10	70

a = Relative abundance

Table 5.3. Capillary/Skimmer CID results for Ru(bpy)<sub>3</sub>(PF<sub>6</sub>)<sub>2</sub>

Ions Detected (m/z)	Capillary/skimmer CID energy (v)					
	29	74	119	154	244	344
[Ru(bpy) <sub>3</sub> ] <sup>2+</sup> (285)	100 <sup>a</sup>	100	24	9		
[Ru(bpy) <sub>2</sub> ] <sup>2+</sup> (207)		2	67	8		
[Ru(bpy) <sub>3</sub> (PF <sub>6</sub> ) <sub>2</sub> Na] <sup>+</sup> (883)	5	5	3			
[Ru(bpy) <sub>3</sub> PF <sub>6</sub> ] <sup>+</sup> (715)	75	63	100	100	100	83
[Ru(bpy) <sub>3</sub> CH <sub>3</sub> COO] <sup>+</sup> (629)	3	3				
[Ru(bpy) <sub>3</sub> ] <sup>+</sup> (570)			7	27	38	57
[Ru(bpy) <sub>2</sub> C <sub>5</sub> H <sub>4</sub> N] <sup>+</sup> (492)				9	15	22
[Ru(bpy) <sub>2</sub> CH <sub>3</sub> COO] <sup>+</sup> (473)		3	3	4	4	3
[Ru(bpy) <sub>2</sub> F] <sup>+</sup> (433)			23	97	74	100
[Ru(bpy) <sub>2</sub> ] <sup>+</sup> (414)				26	82	54
[Ru(bpy)C <sub>5</sub> H <sub>4</sub> N] <sup>+</sup> (336)					45	19
[Ru(bpy)F] <sup>+</sup> (277)					28	7
[Ru(bpy)] <sup>+</sup> (258)		9	5		12	11
[RuC <sub>5</sub> H <sub>4</sub> N] <sup>+</sup> (180)						17
[(bpy)+H] <sup>+</sup> (157)		22	16			

a = Relative abundance

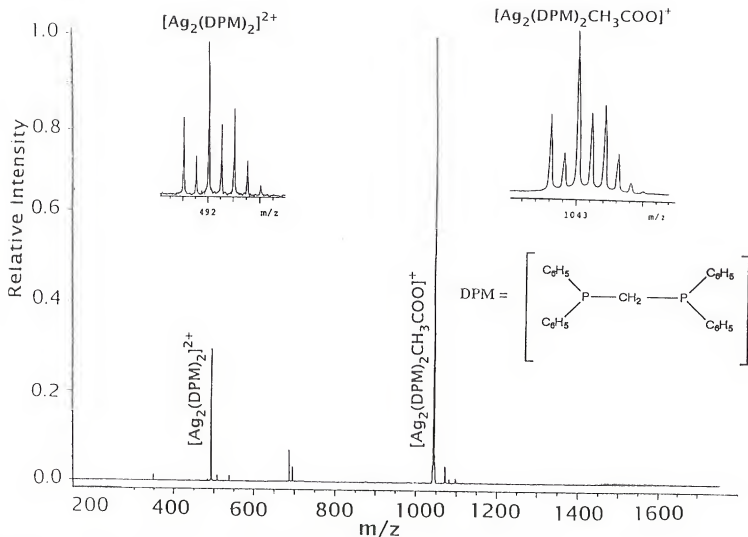
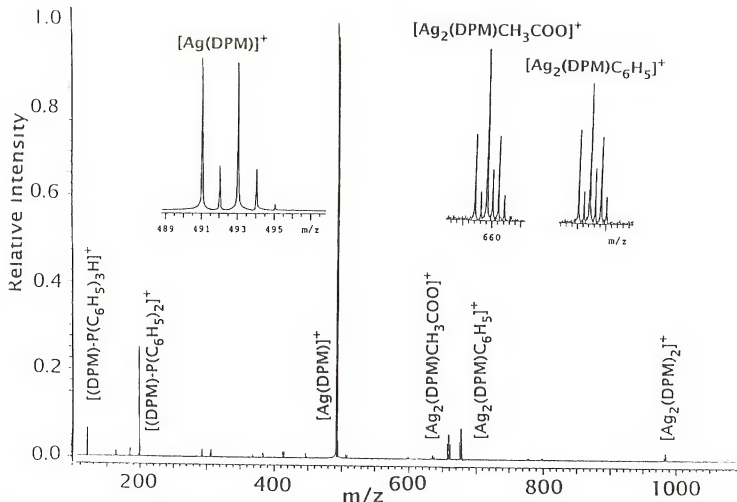


Figure 5.1. External source ESI/FTICR mass spectrum of  $[Ag_2(DPM)_2](BF_4)_2$  obtained with capillary/skimmer CID energy of 29 V.



581

Figure 5.2. External source ESI/FTICR mass spectrum of  $[\text{Ag}_2(\text{DPM})_2](\text{BF}_4)_2$  obtained with capillary/skimmer CID energy of 244 V.

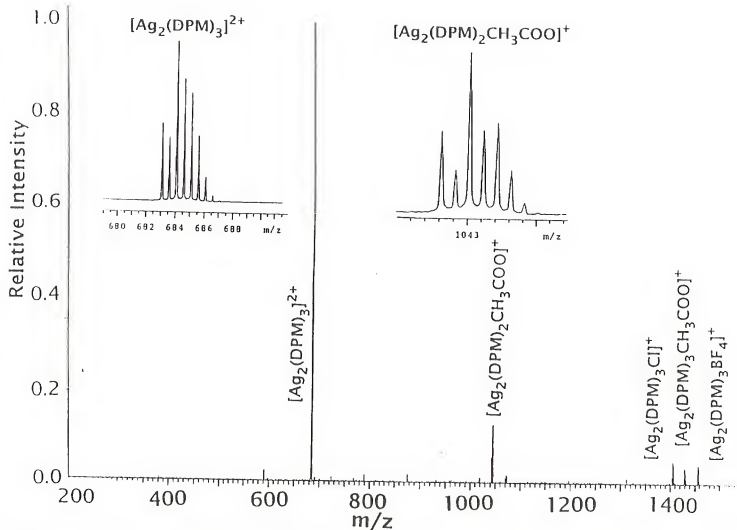


Figure 5.3. External source ESI/FTICR mass spectrum of  $[Ag_2(DPM)_3](BF_4)_2$  obtained with capillary/skimmer CID energy of 29 V.

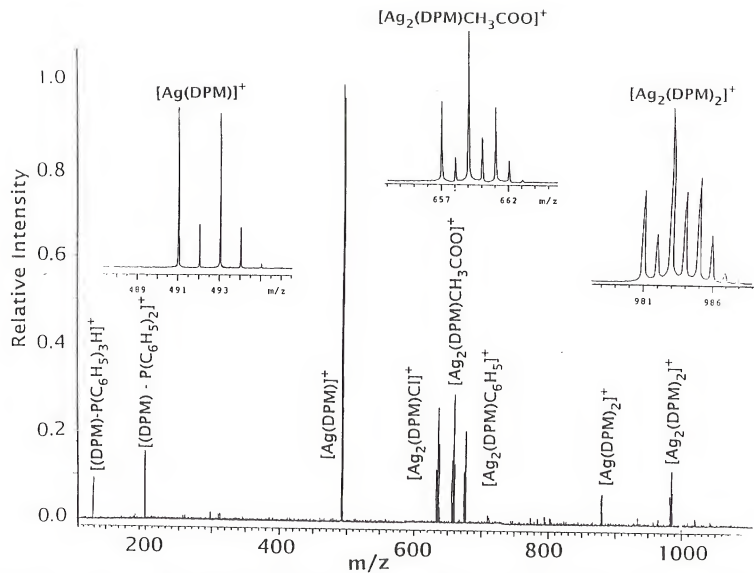


Figure 5.4. External source ESI/FTICR mass spectrum of  $[Ag_2(DPM)_3](BF_4)_2$  obtained with capillary/skimmer CID energy of 244 V.

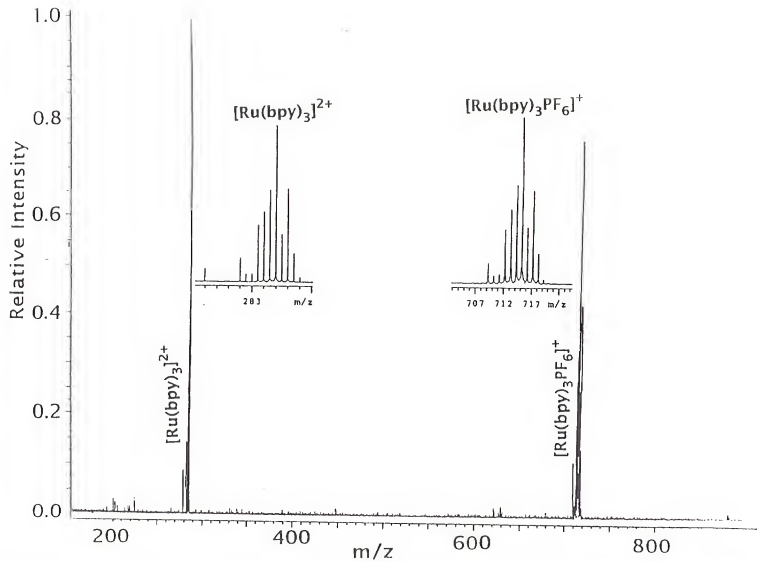


Figure 5.5. External source ESI/FTICR mass spectrum of  $[Ru(bpy)_3](PF_6)_2$  obtained with capillary/skimmer CID energy of 29 V.

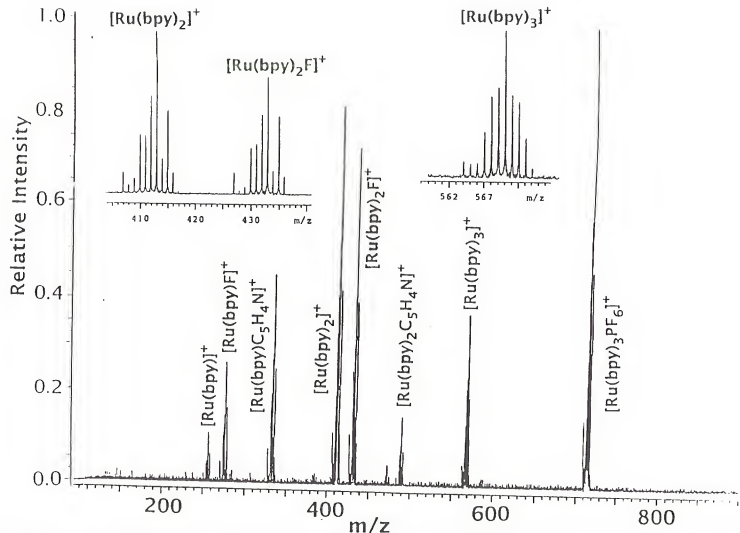


Figure 5.6. External source ESI/FTICR mass spectrum of  $[\text{Ru}(\text{bpy})_3](\text{PF}_6)_2$  obtained with capillary/skimmer CID energy of 29 V.

Table 5.4. In-cell CID of  $[\text{Ag}_2(\text{DPM})_2\text{CH}_3\text{COO}]^+$  produced from external source

Precursor ion	CID pulse width(μs)	Ions Detected (Decreasing Intensity)	(m/z)
$\text{Ag}_2(\text{DPM})_2\text{CH}_3\text{COO}]^+$	0.3	$[\text{Ag}_2(\text{DPM})_2\text{CH}_3\text{COO}]^+$	1041
	1	$[\text{Ag}_2(\text{DPM})_2]^+$	982
		$[\text{Ag}_2(\text{DPM})_2\text{CH}_3\text{COO}]^+$	1041
		$[\text{Ag}_2(\text{DPM})\text{C}_6\text{H}_5]^+$	675
		$[\text{Ag}_2(\text{DPM})\text{CH}_3\text{COO}]^+$	657
	2	$[\text{Ag}_2(\text{DPM})\text{C}_6\text{H}_5]^+$	675
		$[\text{Ag}_2(\text{DPM})_2]^+$	982
		$[\text{Ag}(\text{DPM})]^+$	491
		$[\text{Ag}_2(\text{DPM})\text{CH}_3\text{COO}]^+$	657
		$[\text{Ag}_2(\text{DPM})_2\text{CH}_3\text{COO}]^+$	1041
		$[(\text{DPM-P}(\text{C}_6\text{H}_5)_3\text{H})]^+$	121
	5	$[\text{Ag}(\text{DPM})]^+$	491
		$[\text{Ag}_2(\text{DPM})\text{C}_6\text{H}_5]^+$	675
		$[\text{Ag}_2(\text{DPM})_2]^+$	982
		$[(\text{DPM-P}(\text{C}_6\text{H}_5)_3\text{H})]^+$	121
		$[\text{Ag}_2(\text{DPM})\text{CH}_3\text{COO}]^+$	657
	10	$[(\text{DPM-P}(\text{C}_6\text{H}_5)_3\text{H})]^+$	121
		$[\text{Ag}(\text{DPM})]^+$	491

Table 5.5. In-cell CID of  $[\text{Ag}_2(\text{DPM})_2]^{2+}$  produced from external source ES]

Precursor ion	CID pulse width ( $\mu\text{s}$ )	Ions Detected (Decreasing Intensity)	(m/z)
$\text{Ag}_2(\text{DPM})_2^{2+}$	0.3	$[\text{Ag}_2(\text{DPM})_2]^{2+}$	491
	1	$[\text{Ag}_2(\text{DPM})_2]^{2+}/[\text{Ag}(\text{DPM})]^+$ $[(\text{DPM})-\text{P}(\text{C}_6\text{H}_5)_2]^+$ $[(\text{DPM})-\text{P}(\text{C}_6\text{H}_5)_3\text{H}]^+$ $[\text{DPM}]^+$	491 199 121 384
	2	$[\text{Ag}_2(\text{DPM})_2]^{2+}/[\text{Ag}(\text{DPM})]^+$ $[(\text{DPM})-\text{P}(\text{C}_6\text{H}_5)_2]^+$ $[(\text{DPM})-\text{P}(\text{C}_6\text{H}_5)_3\text{H}]^+$ $[\text{DPM}]^+$	491 199 121 384
	5	$[\text{Ag}_2(\text{DPM})_2]^{2+}/[\text{Ag}(\text{DPM})]^+$ $[(\text{DPM})-\text{P}(\text{C}_6\text{H}_5)_2]^+$ $[(\text{DPM})-\text{P}(\text{C}_6\text{H}_5)_3\text{H}]^+$ $[\text{DPM}]^+$	491 199 121 384
	10	$[\text{Ag}(\text{DPM})]^+$ $[(\text{DPM})-\text{P}(\text{C}_6\text{H}_5)_2]^+$ $[(\text{DPM})-\text{P}(\text{C}_6\text{H}_5)_3\text{H}]^+$ $[\text{DPM}]^+$	491 199 121 384

Table 5.6. In-cell CID of  $[\text{Ru}(\text{bpy})_3]^{2+}$  produced from external source ESI

Precursor ion	CID pulse width(μs)	Ions Detected (Decreasing intensity)	(m/z)
$[\text{Ru}(\text{bpy})_3]^{2+}$	0.3	$[\text{Ru}(\text{bpy})_3]^{2+}$	285
	3	$[\text{Ru}(\text{bpy})_3]^{2+}$	285
	7	$[\text{Ru}(\text{bpy})_3]^{2+}$ $[\text{Ru}(\text{bpy})_2]^{2+}$	285 207
	10	$[\text{Ru}(\text{bpy})_3]^{2+}$ $[\text{Ru}(\text{bpy})_2]^{2+}$ $[(\text{bpy})+\text{H}]^+$ $[\text{Ru}(\text{bpy})]^+$	285 207 157 258
	12	$[(\text{bpy})+\text{H}]^+$ $[\text{Ru}(\text{bpy})_2]^{2+}$ $[\text{Ru}(\text{bpy})_3]^{2+}$ $[\text{Ru}(\text{bpy})]^+$	157 207 285 258
	15	$[(\text{bpy})+\text{H}]^+$ $[\text{RuC}_{10}\text{H}_8]^+$ $[\text{Ru}(\text{bpy})]^+$ $[\text{RuC}_{10}\text{H}_8\text{N}]^+$	157 230 258 244

capillary/skimmer region (1.5 Torr) eliminates the requirement of an additional collision gas. In addition, the pulse sequence used with FTICR mass spectrometry does not have to be sophisticated with isolation, thermalization and CID excitation pulses. As shown in Table 5.1 and Figure 5.1, at a lower capillary/skimmer potential (29 V), collisional activation is low and peaks (decreasing intensity) due to  $[\text{Ag}_2(\text{DPM})_2\text{CH}_3\text{COO}]^+$  (m/z 1041),  $[\text{Ag}_2(\text{DPM})_2]^{2+}$  (m/z 491),  $[\text{Ag}_2(\text{DPM})_2(\text{BF}_4)]^+$  (m/z 1069) and  $[\text{Ag}_2(\text{DPM})_2\text{Cl}]^+$  (m/z 1017) were observed when  $[\text{Ag}_2(\text{DPM})_2(\text{BF}_4)]_2$  was electrosprayed (where DPM =  $(\text{C}_6\text{H}_5)_2\text{P}-\text{CH}_2-\text{P}(\text{C}_6\text{H}_5)_2$ ). The doubly charged ions were easily identified, since peaks occurred with half-mass separation at the expected mass/charge (m/z) range and with the expected isotopic abundances. The singly charged ions,  $[\text{Ag}_2(\text{DPM})_2\text{CH}_3\text{COO}]^+$  (m/z 1041),  $[\text{Ag}_2(\text{DPM})_2(\text{BF}_4)]^+$  (m/z 1069), and  $[\text{Ag}_2(\text{DPM})_2\text{Cl}]^+$  were presumably formed by anion ( $\text{CH}_3\text{COO}^-$ ,  $\text{BF}_4^-$  and  $\text{Cl}^-$ ) addition to the silver complex in solution. The acetate and chloride anions are present as impurities in the solution.

At 74 V capillary/skimmer potential difference, the mass spectrum showed a peak due to a mixture of  $[\text{Ag}_2(\text{DPM})_2]^{2+}$  and  $[\text{Ag}(\text{DPM})]^+$  both at m/z 491. The identity of this mixture could be verified (*vide infra*) by the shift of relative intensities of the isotope peaks from (26.9:49.9:23.2) expected for an ion containing two silver atoms to one more closely approaching that (51.8:48.2) expected for an ion

containing only one silver atom. In addition, peaks due to  $[\text{Ag}_2(\text{DPM})_2]^+$  ( $m/z$  982) and  $[\text{Ag}_2(\text{DPM})_2\text{Cl}]^+$  ( $m/z$  1017) were observed. As shown in Table 5.1, at a capillary/skimmer potential difference of 119 V all doubly charged ions dissociated to give structurally informative fragment ions, and  $[\text{Ag}_2(\text{DPM})_2]^+$  ( $m/z$  982) was observed as the most intense peak in the spectrum. In addition, ions such as  $[\text{Ag}(\text{DPM})]^+$  ( $m/z$  491),  $[\text{Ag}(\text{DPM})_2]^+$  ( $m/z$  875), and  $[\text{Ag}(\text{DPM})_2\text{Cl}]^+$  ( $m/z$  910), each containing one silver atom, were also observed in the spectrum. At a capillary/skimmer potential difference of 154 V a peak due to loss of a DPM ligand from  $[\text{Ag}_2(\text{DPM})_2\text{CH}_3\text{COO}]^+$  ( $m/z$  1041) was observed as the most intense peak in the spectrum and DPM dissociated to produce  $[\text{DPM}-\text{P}(\text{C}_6\text{H}_5)_2]^+$  at  $m/z$  199. As shown in Figure 5.2, increasing the capillary/skimmer potential difference to 244 V produced  $[\text{Ag}(\text{DPM})]^+$  ( $m/z$  491) as the intense peak, and DPM further dissociated to give structurally informative peaks such as  $[(\text{DPM})-\text{CH}_2\text{P}(\text{C}_6\text{H}_5)_2]^+$  ( $m/z$  185) and  $[(\text{DPM})-\text{P}(\text{C}_6\text{H}_5)_3\text{H}]^+$  ( $m/z$  121). At the highest capillary/skimmer potential difference used, 344 V, fragments due to dissociation of DPM appeared as most intense peaks.

The capillary/skimmer CID of  $\text{Ag}_2(\text{DPM})_3(\text{BF}_4)_2$  parallels that of the  $\text{Ag}_2(\text{DPM})_2(\text{BF}_4)_2$ . The observed dissociation pathways for this ion are listed in Table 5.2. At 29 V of capillary/skimmer potential difference, the CID processes are negligible, and  $[\text{Ag}_2(\text{DPM})_3]^{2+}$  ( $m/z$  683) was observed as the most intense peak (Figure 5.3). Other ions observed included

$[\text{Ag}_2(\text{DPM})_2\text{CH}_3\text{COO}]^+$  ( $m/z$  1041),  $[\text{Ag}_2(\text{DPM})_3\text{Cl}]^+$  ( $m/z$  1401),  $[\text{Ag}_2(\text{DPM})_3\text{BF}_4]^+$  ( $m/z$  1453),  $[\text{Ag}_2(\text{DPM})_3\text{CH}_3\text{COO}]^+$  ( $m/z$  1425),  $[\text{Ag}_2(\text{DPM})_2\text{BF}_4]^+$  ( $m/z$  1069) and  $[\text{Ag}(\text{DPM})_2]^+$  ( $m/z$  875) (due to anion adduction and/or some fragmentation). Increasing the capillary potential to 80 V promoted dissociation to form  $[\text{Ag}_2(\text{DPM})]^2+/[\text{Ag}(\text{DPM})]^+$  at  $m/z$  491. In addition, all  $[\text{Ag}_2(\text{DPM})_3\text{X}]^+$  (where  $\text{X} = \text{Cl}^-$ ,  $\text{BF}_4^-$  and  $\text{CH}_3\text{COO}^-$ ) ions dissociated to produce  $[\text{Ag}_2(\text{DPM})_2\text{X}]^+$  ions. As observed for  $\text{Ag}_2(\text{DPM})_2(\text{BF}_4)_2$  at 119 V, all doubly charged ions dissociated and ions containing a single silver atom were observed in the spectrum. At a capillary/skimmer potential difference of 154 V, DPM dissociated to give  $[(\text{DPM})-\text{P}(\text{C}_6\text{H}_5)_2]^+$  ( $m/z$  199), and ions due to loss of a DPM ligand from  $[\text{Ag}_2(\text{DPM})_2\text{X}]^+$  were observed in the spectrum ( $[\text{Ag}_2(\text{DPM})\text{CH}_3\text{COO}]^+$  ( $m/z$  657) and  $[\text{Ag}_2(\text{DPM})\text{Cl}]^+$  ( $m/z$  633)). As shown in Figure 5.4, at capillary/skimmer potential difference higher than 154 V, DPM further dissociated to give structurally informative ions such as  $[(\text{DPM})-\text{P}(\text{C}_6\text{H}_5)_3\text{H}]^+$  ( $m/z$  121),  $[(\text{DPM})-\text{P}(\text{C}_6\text{H}_5)_2]^+$  ( $m/z$  199) and  $[(\text{DPM})-\text{CH}_2\text{P}(\text{C}_6\text{H}_5)_2]^+$  ( $m/z$  185).

Presence of fragment ions containing a single silver atom and the absence of  $\text{Ag}_2^+$  in the spectrum suggest that there are no bonds between the silver atoms in  $\text{Ag}_2(\text{DPM})_2(\text{BF}_4)_2$  and  $\text{Ag}_2(\text{DPM})_3(\text{BF}_4)_2$ . This conclusion is reinforced by X-ray crystallographic studies (236) which give 3.105 Å as the Ag--Ag distance in  $\text{Ag}_2(\text{DPM})_3(\text{BF}_4)_2$ . Previous work on complexes containing two silver atoms has been inconclusive regarding

the existence of metal-metal bonds. Busch et al. (239) examined the silver salts of acetic acid, propionic acid and benzoic acid using SI and EI ionization. In that study ions such as  $\text{Ag}_2\text{X}^+$  (where X is H, O, OH,  $\text{CH}_3$ ,  $\text{CH}_3\text{COO}$ , and  $\text{CH}_3\text{COOCH}_2$ ) were formed and analyzed by tandem mass spectrometry. All of the  $\text{Ag}_2\text{X}^+$  ions except  $\text{Ag}_2\text{H}^+$  and  $\text{Ag}_2\text{OH}^+$  dissociated to give  $\text{Ag}_2^+$ . This observation led the authors to conclude that, with the exception of  $\text{Ag}_2\text{H}^+$  and  $\text{Ag}_2\text{OH}^+$ , all of the  $\text{Ag}_2\text{X}^+$  contained metal-metal bonds. These experimental findings were not supported theoretically by Dekock et al. (240), who used Hartree-Fock calculations to study  $\text{Ag}_2\text{H}^+$  and  $\text{Ag}_2\text{CH}_3^+$ . They predicted that both of these ions contain metal-metal bonds. However, a study of  $\text{Ag}_2\text{H}^+$  by Gaspar et. al (241) used a simple molecular pseudopotential method and concluded that this ion does not contain any metal-metal bonds.

Capillary/skimmer CID results for  $\text{Ru}(\text{bpy})_3(\text{PF}_6)_2$  are summarized in Table 5.3 (where bpy =  $(\text{NH}_4\text{C}_5)-(\text{C}_5\text{H}_4\text{N})$ ). As shown in Figure 5.5, at a capillary/skimmer potential difference of 29 V  $[\text{Ru}(\text{bpy})_3]^{2+}$ , m/z 285, was the most intense peak in the mass spectrum. In addition, peaks due to  $[\text{Ru}(\text{bpy})_3\text{PF}_6]^+$  (m/z 715),  $[\text{Ru}(\text{bpy})_3(\text{PF}_6)_2\text{Na}]^+$  (m/z 883) and  $[\text{Ru}(\text{bpy})_3\text{CH}_3\text{COO}]^+$  (m/z 629) were also observed. Increasing the capillary potential to 80 V produced  $[\text{Ru}(\text{bpy})_2]^{2+}$  (m/z 207) and  $[\text{Ru}(\text{bpy})_2\text{CH}_3\text{COO}]^+$  (m/z 473), corresponding to the loss of one bipyridyl ligand from  $[\text{Ru}(\text{bpy})_3]^{2+}$  (m/z 285) and

$[\text{Ru}(\text{bpy})_3\text{CH}_3\text{COO}]^+$  ( $m/z$  629), respectively. At a capillary/skimmer potential difference of 119 V dissociation of  $\text{PF}_6^-$  ( $\text{PF}_6^- \longrightarrow \text{PF}_5 + \text{F}^-$ ) is evident from the presence of  $[\text{Ru}(\text{bpy})_2\text{F}]^+$  at  $m/z$  433. At higher capillary/skimmer potential difference decaying intensity for  $[\text{Ru}(\text{bpy})_2]^{2+}$  ( $m/z$  207) and increasing intensity for  $[\text{Ru}(\text{bpy})_2\text{F}]^+$  ( $m/z$  433) indicated that  $[\text{Ru}(\text{bpy})_2\text{F}]^+$  is forming from  $[\text{Ru}(\text{bpy})_2]^{2+}$ . Structurally informative peaks corresponding to  $[(\text{bpy})+\text{H}]^+$  ( $m/z$  157),  $[\text{Ru}(\text{bpy})]^+$  ( $m/z$  258) and  $[\text{Ru}(\text{bpy})_3]^+$  ( $m/z$  570) were also observed in the mass spectrum. At a capillary/skimmer potential difference of 154 V  $[\text{Ru}(\text{bpy})_3(\text{PF}_6)_2\text{Na}]^+$  disappears, and new peaks due to  $[\text{Ru}(\text{bpy})_2\text{C}_5\text{H}_4\text{N}]^+$  ( $m/z$  492) and  $[\text{Ru}(\text{bpy})_2]^+$  ( $m/z$  414) appear in the spectrum. As shown in Figure 5.6, at 244 V of capillary/skimmer potential difference the fluoride ion is apparently retained when the loss of bipyridyl ligand occurs from  $[\text{Ru}(\text{bpy})_2\text{F}]^+$  to form  $[\text{Ru}(\text{bpy})\text{F}]^+$  at  $m/z$  277. In addition, a peak corresponding to  $[\text{Ru}(\text{bpy})\text{C}_5\text{H}_4\text{N}]^+$  at  $m/z$  336 was observed in the spectrum. Detection of ions containing the pyridyl group ( $\text{C}_5\text{H}_4\text{N}$ ), in fragments such as  $[\text{Ru}(\text{bpy})_2\text{C}_5\text{H}_4\text{N}]^+$  ( $m/z$  492),  $[\text{Ru}(\text{bpy})\text{C}_5\text{H}_4\text{N}]^+$  ( $m/z$  336) and  $[\text{RuC}_5\text{H}_4\text{N}]^+$  ( $m/z$  180) suggests that C-C bond cleavage is occurring in the bipyridyl ligand.

As to the formation of  $[(\text{bpy})+\text{H}]^+$ , we speculate it is formed from the gas phase reaction of  $[\text{Ru}(\text{bpy})_2]^{2+}$  with background water ( $[\text{Ru}(\text{bpy})_2]^{2+}$  ( $m/z$  207) +  $\text{H}_2\text{O} \longrightarrow [\text{Ru}(\text{bpy})]^+$  ( $m/z$  258) +  $[(\text{bpy})+\text{H}]^+$  ( $m/z$  157) +  $\text{OH}^-$ ). The formation of

$[(bpy)+H]^+$  from  $Fe(bpy)_3(SO_4)$  and  $Ni(bpy)_3(SO_4)$  has been studied in detail by Turecek et al. (196), using an electrospray ionization double-focusing mass spectrometer. Their results led to the conclusion that  $[(bpy)+H]^+$  is due to solution chemistry and not due to reaction of the complex ions in the gas phase. The study by Turecek et al. (196) contrasts with the CID study of Chait et al. (211) and our ESI/FTICR study on  $Ru(bpy)_3(PF_6)_2$ . Our speculation that  $[(bpy)+H]^+$  is forming from the reaction of  $[Ru(bpy)_2]^{2+}$  with background water is further confirmed using the in-cell CID method, which will be discussed in the next section.

In a study by Freas et al. (242) FAB was used to obtain structural information on  $[Ru(bpy)_2(tpy)](PF_6)_2$  and  $[Ru(bpy)_2(bdmt)](PF_6)_2$  (where typ = 2,2':6,2"-terpyridine and bdmt = 3,3':5,3"-bis(bimethylene)-2,2':6,2"-terpyridine). In that study the highest mass ions observed included  $[Ru(bpy)_2(bdmt)PF_6]^+$  ( $m/z$  844), and  $[Ru(bpy)_2(tpy)PF_6]^+$  ( $m/z$  792), corresponding to loss of a  $PF_6^-$  counterion. In addition, peaks corresponding to the doubly charged ions  $[Ru(bpy)_2(bdmt)]^{2+}$  and  $[Ru(bpy)_2(tpy)]^{2+}$  were observed. The fragmentation pathways suggested for the formation of  $[Ru(bpy)(bdmt)F]^+$ ,  $[Ru(bpy)(tpy)F]^+$  and  $[Ru(bdmt)F]^+$  resemble that of the  $[Ru(bpy)_2F]^+$  and  $[Ru(bpy)F]^+$  observed in our ESI/FTICR study. The absence of  $[Ru(bpy)_2(bdmt)F]^+$  led Freas et al. to conclude that the fluoride ion is an inner-sphere ligand, and that fluoride-containing ions arise from the gas-

phase dissociation of  $\text{PF}_6^-$  in the FAB source. These observations by Freas et al. corroborate the results obtained using ESI/FTICR ( $[\text{Ru}(\text{bpy})_3\text{F}]^+$  and  $[\text{Ru}(\text{phen})_3\text{F}]^+$  were not observed) on  $[\text{Ru}(\text{bpy})_3](\text{PF}_6)_2$  and  $[\text{Ru}(\text{phen})_3](\text{PF}_6)_2$  (243) (where phen = 1,10-phenanthroline).

#### In-Cell CID

Although numerous speculations can be made from capillary/skimmer CID data, the results are often not conclusive, because the identity of parent ions undergoing dissociation is not known. Thus, a particular fragment might arise from two or more parents, or from a different parent than appears most likely. In an attempt to obtain more detailed structural information from unambiguous fragmentation pathways, in-cell CID experiments were carried out on  $[\text{Ag}_2(\text{DPM})_2\text{CH}_3\text{COO}]^+$ ,  $[\text{Ag}_2(\text{DPM})_2]^{2+}$  and  $[\text{Ru}(\text{bpy})_3]^{2+}$ . Since the ion of interest is isolated in the FTICR analyzer cell prior to CID, this technique is more reliable for deducing structural information. Using this method allows several questions to be addressed. (1) Is the  $[\text{Ag}_2(\text{DPM})_x]^{+59}$  (where  $x = 1, 2$ , and  $3$ ) due to the addition of  $\text{CH}_3\text{COO}^-$  or to solvation with  $\text{CH}_3\text{CN}$  and  $\text{H}_2\text{O}$ ? (2) Do  $[\text{Ag}_2(\text{DPM})_2]^{2+}$  and  $[\text{Ru}(\text{bpy})_3]^{2+}$  undergo reduction to form  $[\text{Ag}_2(\text{DPM})_2]^+$  and  $[\text{Ru}(\text{bpy})_3]^+$ , respectively? (3) Is  $[\text{Ru}(\text{bpy})_x\text{F}]^+$  produced from the dissociation of  $\text{PF}_6^-$  or by some other mechanism? (4) Is

[ $(\text{bpy}+\text{H})^+$  due to CID of  $[\text{Ru}(\text{bpy})_3]^+$  in the gas phase or from some other solution chemistry?

As shown in Table 5.4, results from in-cell CID of  $[\text{Ag}_2(\text{DPM})_2+59]^+$  ( $m/z$  1041) suggest that mass 59 arises from  $\text{CH}_3\text{COO}^-$  and not from solvation with  $\text{CH}_3\text{CN}$  and  $\text{H}_2\text{O}$ . If mass 59 were due to  $\text{CH}_3\text{CN}$  and  $\text{H}_2\text{O}$ , CID of  $m/z$  1041 would have produced fragment ions at  $m/z$  1000 and/or 1023. Increasing the CID pulse width from 0.3 to 1  $\mu\text{s}$  produced  $[\text{Ag}_2(\text{DPM})_2]^+$  as a quite intense peak. Further increase in the CID energy produced a peak due to  $[\text{Ag}_2(\text{DPM})+59]^+$  and peaks corresponding to addition of  $\text{CH}_3\text{CN}$  and/or  $\text{H}_2\text{O}$  were absent from the spectrum.

Results from the in-cell CID of  $[\text{Ag}_2(\text{DPM})_2]^{2+}$  ( $m/z$  491) are shown in Table 5.5. When the CID pulse width was 0.3  $\mu\text{s}$ , the parent was still observed as the most intense peak. Increasing the CID pulse width from 0.3 to 1  $\mu\text{s}$  produced a mixture of  $[\text{Ag}_2(\text{DPM})_2]^{2+}/[\text{Ag}(\text{DPM})]^+$  at  $m/z$  491 and fragments due to dissociation of DPM ( $[(\text{DPM})-\text{P}(\text{C}_6\text{H}_5)_3\text{H}]^+$  ( $m/z$  121) and  $[(\text{DPM})-\text{P}(\text{C}_6\text{H}_5)_2]^+$  ( $m/z$  199) were observed in the spectrum. When the CID pulse width was increased to 10  $\mu\text{s}$ ,  $[\text{Ag}(\text{DPM})]^+$  ( $m/z$  491) was observed as the most intense peak. Results from these CID experiments indicate that no reduction reaction is occurring. If reduction had occurred, a peak due to  $[\text{Ag}_2(\text{DPM})_2]^+$  ( $m/z$  982) should have been observed in the results.

The high mass resolution capabilities of FTICR have long been identified as one of the analytical advantages of the

technique in comparison with other forms of mass spectrometry. In 1983, Wanczek et al. (244) used a 4.7 Tesla magnet and a background pressure of  $8 \times 10^{-11}$  mbar to achieve a resolution in excess of  $10^8$  for water. Recently, McLafferty et al. (96) and Smith et. al (98) have shown that ultrahigh resolution can be achieved with ESI/FTICR. The advantage of using a high mass resolution instrument for CID experiments is shown from the results on  $[\text{Ag}_2(\text{DPM})_2]^{2+}$  ( $m/z$  491). Since  $[\text{Ag}_2(\text{DPM})_2]^{2+}$  and  $[\text{Ag}(\text{DPM})]^+$  both occur at a nominal  $m/z$  of 491, it would be a difficult task to differentiate between  $[\text{Ag}_2(\text{DPM})_2]^{2+}$  and  $[\text{Ag}(\text{DPM})]^+$  without a routine resolution of 0.5 amu. Figure 5.7 gives further indication of the importance of the high mass resolution in the analysis of organometallic complexes. Figure 5.7a illustrates the results obtained with a minimum energy deposition (CID pulse width = 0.3  $\mu\text{s}$ ) into the parent ion ( $[\text{Ag}_2(\text{DPM})_2]^{2+}$ ). At this CID energy peaks at  $m/z$  491, 492 and 493 are due to  $[\text{^{107}Ag}^{107}\text{Ag}(\text{DPM})_2]^{2+}$ ,  $[\text{^{107}Ag}^{109}\text{Ag}(\text{DPM})_2]^{2+}$  and  $[\text{^{109}Ag}^{109}\text{Ag}(\text{DPM})_2]^{2+}$ , respectively. Peaks occurring at  $m/z$  491.5, 492.5 and 493.5 are due to the presence of carbon-13 isotopes. Increasing the CID pulse width from 0.3 to 10  $\mu\text{s}$  deposits more energy into the parent ion and produces more fragmentation. Figure 5.7e illustrates the results obtained with a CID pulse width of 10  $\mu\text{s}$ ; at this CID energy fragment ions due to  $[\text{^{107}Ag}(\text{DPM})]^+$  and  $[\text{^{109}Ag}(\text{DPM})]^+$  were observed at  $m/z$  491 and 493, respectively.

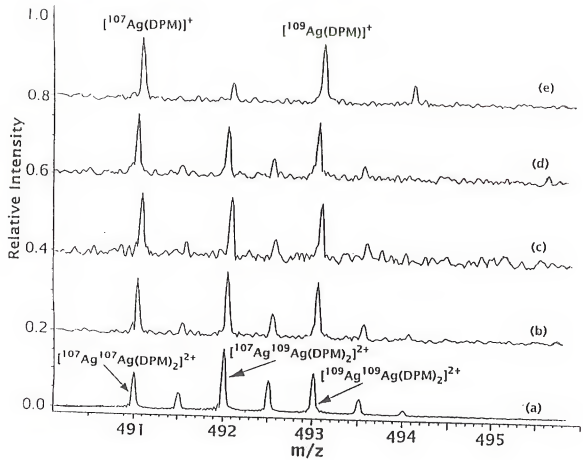


Figure 5.7. Mass spectra from in-cell CID of  $[\text{Ag}_2(\text{DPM})_2]^{2+}$ . CID pulse width was (amplitude was 36 V<sub>P-P</sub>): (a) 0.3  $\mu$ s; (b) 1  $\mu$ s; (c) 2  $\mu$ s; (d) 5  $\mu$ s; and (e) 10  $\mu$ s.

Results from in-cell CID of  $[\text{Ru}(\text{bpy})_3]^{2+}$  (*m/z* 285) are given in Table 5.6. Increasing the CID pulse width from 0.3 to 7  $\mu\text{s}$  produced  $[\text{Ru}(\text{bpy})_2]^{2+}$  (*m/z* 207) as the major fragment ion. Further increase of the CID pulse width from 7  $\mu\text{s}$  to 10  $\mu\text{s}$  produced fragment ions due to  $[\text{Ru}(\text{bpy})_2]^{2+}$  (*m/z* 207),  $[\text{Ru}(\text{bpy})]^+$  (*m/z* 258) and  $[(\text{bpy})+\text{H}]^+$  (*m/z* 157). When more energy was imparted to the  $[\text{Ru}(\text{bpy})_3]^{2+}$  ion (pulse width of 15  $\mu\text{s}$ ), all the doubly charged ions dissociated to give  $[\text{Ru}(\text{bpy})]^+$  and  $[(\text{bpy})+\text{H}]^+$ .

As described by Freas et al. (242), the loss of a bipyridyl ligand from  $[\text{Ru}(\text{bpy})_3]^{2+}$  opens one or two coordination sites in the hexacoordinated Ru(II) complex and the availability of  $\text{F}^-$  produced from the dissociation of  $\text{PF}_6^-$  then leads to the formation of  $[\text{Ru}(\text{bpy})_2\text{F}]^+$  (*m/z* 433). The question arises as to the mechanism of formation of  $[\text{Ru}(\text{bpy})\text{F}]^+$  (*m/z* 277). One possibility is the simple loss of a bipyridyl ligand from  $[\text{Ru}(\text{bpy})_2\text{F}]^+$ . Another possibility is formation of  $[\text{Ru}(\text{bpy})]^+$  followed by complexation with  $\text{F}^-$  to form  $[\text{Ru}(\text{bpy})\text{F}]^+$ . However, the latter pathway can be ruled out, because  $[\text{Ru}(\text{bpy})]^+$  was not present in the capillary/skimmer CID experiments. In addition, the results presented here indicate that there is no reduction occurring in these reactions. This observation supports the results obtained by Chait et al. (211) and Cook et al. (220) for  $[\text{Ru}(\text{bpy})_3]\text{Cl}_2$ . However, ligand exchange reactions between the  $[\text{Ru}(\text{bpy})_3]^{2+}$  and  $\text{Cl}^-$  or solvent, as reported in detail above, were not observed in the earlier studies.

In-cell CID of  $[\text{Ru}(\text{bpy})_3]^{2+}$  produces  $[(\text{bpy})+\text{H}]^+$  as one of the fragment ions. Since all other ions were ejected from the analyzer cell,  $[(\text{bpy})+\text{H}]^+$  must be formed by the reaction of  $[\text{Ru}(\text{bpy})_2]^{2+}$  with background water or water present in the collision gas. If  $[(\text{bpy})+\text{H}]^+$  were preformed in the solution as Turecek et al. (196) observed in their study, at lower capillary/skimmer CID energies, a peak due to  $[(\text{bpy})+\text{H}]^+$  should have been observed along with  $[\text{Ru}(\text{bpy})_3]^{2+}$  and  $[\text{Ru}(\text{bpy})_3\text{PF}_6]^+$ . Thus, the in-cell CID of  $[\text{Ru}(\text{bpy})_3]^{2+}$  suggests that the formation of  $[(\text{bpy})+\text{H}]^+$  is due to ion/molecule reaction of the  $[\text{Ru}(\text{bpy})_2]^{2+}$  in the gas phase. As shown in Table 5, the formation of  $[\text{Ru}(\text{bpy})]^+$  ( $m/z$  258) and  $[(\text{bpy})+\text{H}]^+$  ( $m/z$  157) and the disappearance of  $[\text{Ru}(\text{bpy})_2]^{2+}$  ( $m/z$  207) with a CID pulse width of 10  $\mu\text{s}$  suggest that the precursor for  $[(\text{bpy})+\text{H}]^+$  is  $[\text{Ru}(\text{bpy})_2]^{2+}$ .

### Conclusions

The highest mass ions observed for  $\text{Ag}_2(\text{DPM})_3(\text{BF}_4)_2$  and  $\text{Ag}_2(\text{DPM})_2(\text{BF}_4)_2$  corresponded to  $[\text{Ag}_2(\text{DPM})_n\text{BF}_4]^+$  (where  $n$  is 2 and 3). Abundant doubly charged ions ( $[\text{Ag}_2(\text{DPM})_3]^{2+}$  and  $[\text{Ag}_2(\text{DPM})_2]^{2+}$ ) were observed at lower activation energies. Predominant fragment ions were due to losses of DPM ligands. At higher activation energies products due to dissociation of DPM ligand were observed in the spectra. In-cell CID experiments on  $[\text{Ag}_2(\text{DPM})_2]^{2+}$  demonstrated the advantage of

using a high mass resolution mass spectrometer to study organometallic complexes.

The highest mass ion observed for  $\text{Ru}(\text{bpy})_3(\text{PF}_6)_2$  corresponded to  $[\text{Ru}(\text{bpy})_3\text{PF}_6]^+$  ( $m/z$  715). Abundant  $[\text{Ru}(\text{bpy})_3]^{2+}$  was observed at capillary/skimmer activation energies of 74 V or less. The predominant fragment ions in the capillary/skimmer CID spectra are due to losses of intact bipyridyl ligands and  $\text{PF}_5$ . Higher activation energies produced fragments due to C-C bond cleavage from the bipyridyl ligand.

The results of this study suggest that ESI/FTICR can be an important tool in the study of organometallic complexes. In addition, capillary/skimmer and in-cell CID methods are useful for the determination of the fragmentation pathways of organometallic complexes.

CHAPTER 6  
ELECTRON AFFINITIES OF SMALL CARBON CLUSTERS

Introduction

For many years both theoretical and experimental groups have studied carbon molecules, attempting to elucidate their physical properties and the processes leading to their formation. From its early stages to more recent times, mass spectrometry has contributed significantly to carbon cluster studies. Application of mass spectrometry to investigate carbon clusters can be traced back to experiments of Hahn et al. (245) in 1942. Much of the recent immense interest in carbon clusters can be attributed to the discovery of large spherical carbon clusters which have been termed "fullerenes". This name was mainly used to refer to C<sub>60</sub> molecules, because of their structural resemblance to the domes (consisting of hexagons and pentagons) designed by the architect Buckminster Fuller (246). Among the factors promoting interest in fullerenes are their unusually high symmetry and rigidity.

Mass spectrometry was the technique used in the discovery of C<sub>60</sub> and C<sub>70</sub> molecules produced from carbon vapor (247). Recently, these species have been produced in macroscopic quantities either by vaporization of graphite rods with

resistive heating or carbon contact-arc methods (248). In a recent paper by Greenwood (249), the role mass spectrometry has played in carbon cluster studies is reviewed in detail.

Small carbon cluster ions were investigated extensively long before the emergence of interest in the fullerenes. These studies showed that cluster configuration and reactivity differ from that of the bulk (250-251). Knowledge of chemical and the physical properties of small carbon clusters can serve as a bridge to understanding the behavior of larger carbon clusters and the bulk. In addition, small carbon clusters have been of particular interest because of their presence in interstellar space and comets (252) and their role in combustion processes (253). The first experiments on small carbon clusters were done by Chupka et al. (254) in 1953. In their study mass spectrometry was used to detect C, C<sub>2</sub> and C<sub>3</sub> present in the carbon vapor produced by sublimation of graphite. Since then many different methods have been used to generate carbon clusters, including high temperature ovens (255), laser desorption (256), ion bombardment (257) and laser desorption coupled with a molecular beam expansion (258). The technique most often used is the direct laser desorption of graphite, generating neutral clusters and cluster ions ranging in size from small diatomic clusters to clusters containing hundreds of atoms. Laser desorption of graphite, polyimide, and benzene soot has produced carbon clusters in the range of C<sub>200</sub> (259), C<sub>400</sub> (260) and C<sub>600</sub> (261), respectively.

Theoretical investigations of small carbon clusters can be traced back to pioneering *ab initio* calculations by Pitzer and Clementi (262). Their work suggested that the odd-numbered carbon clusters have enhanced stability and carbon clusters should have cumulenic linear structures until reaching the C<sub>10</sub> cluster size. Several other theoretical (263-264) and experimental (265) studies have supported the findings of Pitzer and Clementi. A review by Weltner and Van Zee summarizes the experimental and theoretical studies on carbon clusters up to November 1988 (266).

These earlier studies have mainly involved C<sub>n</sub><sup>+</sup> cations, and have followed the changes in cluster chemical and physical properties as the number of carbon atoms is increased. The cluster anions, C<sub>n</sub><sup>-</sup>, have received relatively less attention in both experimental and theoretical studies. Studies by Kroto (267) and Herbst (268) have shown that ion-molecule reactions dominate the chemistry occurring in comet tails and carbon stars. In addition, carbon clusters are found in high temperature combustion processes (253). Thus, laser-generated, energized, evaporated cluster ions are ideal for studying the chemistry occurring in these combustion processes. FTICR mass spectrometry is a versatile technique to study complicated ion-molecule reactions. In addition, this technique offers several advantages over other mass spectrometric techniques including high-mass range, high mass resolution, simultaneous detection of all ions, ion storage

capabilities, ion probing capabilities (CID and photodissociation) and rapid data acquisition. Most of these capabilities were discussed in chapters 1 and 2. The pulsed nature of the FTICR mass spectrometer makes it ideal for laser desorption of ions from nonvolatile and thermally labile compounds. Freiser et al. and Gross et al. were the first groups to use a pulsed laser with a FTICR mass spectrometer (269) for ion formation. Since then use of lasers as an ionizing source for mass spectrometric studies has increased dramatically. A wide range of compound classes has been studied by laser desorption FTICR (LDFTICR), including organic (270), inorganic (271), organometallic (272), polymers (273), clinical drugs (274) and proteins (275). Laser desorption FTICR (LDFTICR) studies of carbon cluster ion reactivity have provided information about the presence of differing isomeric forms of carbon clusters and indirect information about structures (276-278). These studies have also indicated that LDFTICR mass spectrometry is an ideal technique for studying the reactivity and the structure of cluster ions.

The electron affinity (EA) of a cluster is one of its most important physical properties. Accurate determination of the electron affinities of small carbon clusters can lead to a better understanding of their reactivity and configuration. Previously, Smalley et al. (279-280) determined the electron affinities and electronic structure of carbon clusters with 2-84 atoms using Ultraviolet Photoelectron Spectroscopy (PES).

The electron affinities determined by PES are vertical rather than adiabatic (281) and the earlier work also led to poor agreement with EA's available in the literature. In addition, PES studies do not give conclusive evidence regarding the presence or absence of isomeric carbon clusters. Smalley et al. (279-280) used the second harmonic of a Nd:YAG laser to produce the carbon clusters and a F<sub>2</sub> excimer laser for photodetachment in the throat of the supersonic nozzle. Since Smalley's initial attempt to determine the EA's of small carbon clusters, several other experimental (282-286) and theoretical (287-293) studies have contributed values for electron affinities of small carbon clusters.

The electron affinities determined by FTICR reactivity studies are much closer to adiabatic than vertical. Carbon cluster ions are formed directly in the cell by laser desorption of a graphite plug. Once the C<sub>n</sub><sup>-</sup> of interest is trapped in the cell, during a "thermalizing" period it undergoes many ion-molecule collisions ( $\geq 100$ ) with the thermalizing gas and loses most of its internal energy. In addition, using the charge-transfer bracketing technique the presence or absence of isomeric carbon cluster anions can be easily identified. If two forms of cluster anions are present with different EA's, the reaction vs. time graph of the carbon cluster anion will reflect it. Thus, the carbon cluster anion integrated peak intensity curve will not exponentially decay; instead it will exhibit more than one

rate constant. As shown in Equations 6.1 and 6.2, during the charge-transfer reaction time the occurrence (Equation 6.1) or non-occurrence (Equation 6.2) of charge-transfer from  $C_n^-$  to a neutral reference compound (A or B) of known EA is followed.



Equation 6.1 indicates that EA of  $C_n < EA$  of A



Equation 6.2 indicates that EA of  $C_n > EA$  of B. From Equations 6.1 and 6.2, EA of A > EA of  $C_n > EA$  of B.

The long lifetimes of the charge-transfer ion-molecule complex allow for geometry changes from the most stable ionic structure to the most stable neutral structure. Since the electron affinities determined by the FTICR experiments are not corrected to 0 K for the ions and neutrals involved, the electron affinities determined are not true adiabatic values, but should approach them quite closely. Ionization potentials of carbon clusters containing from 3 to 24 atoms and from 48 to 200 atoms have been bracketed with an uncertainty of few tenths of an eV using the charge-transfer bracketing technique (294-296). In addition to this, the charge-transfer bracketing technique has proven valuable in determining the ionization potentials of arsenic, phosphorus and coinage metal

clusters (297-298). Previously, we used a different laser to produce carbon cluster anions and the bracketing technique to determine the EA's of carbon clusters containing from 4 to 8 atoms, and C<sub>60</sub> and C<sub>70</sub> (299). The EA's bracketed for C<sub>60</sub> and C<sub>70</sub> were in good agreement with literature values. However, the EA's of C<sub>4</sub> - C<sub>8</sub> agreed poorly with literature values (299). In this chapter, work which determines EA's of carbon clusters containing from 4 to 9 atoms with an uncertainty of a few tenths of an eV by the charge transfer bracketing technique is reported. Electron affinities obtained were compared with several previous experimental and theoretical EA values. Several interesting reactions other than charge-transfer were observed during this study. These side-reactions are discussed, along with electron affinities of C<sub>4</sub> - C<sub>9</sub>.

#### Experimental

Laser desorption experiments described in this chapter were performed in a mass spectrometer equipped with an Ion Spec data station, Nicolet FT/MS 1000 vacuum assembly, 3 Tesla Oxford superconducting magnet, and a heated inlet system equipped with two precision leak valves. A schematic representation of the FTICR mass spectrometer used in this study is shown in Figure 2.8. The high vacuum chamber (7.8 cm inside diameter) was pumped by a 300 L/s oil diffusion pump.

A second diffusion pump with a pumping speed of 150 L/s was mainly used for initial pump down of the system and to pump on the inlet system. The background pressure of the system was maintained at  $5 \times 10^{-9}$  Torr. This high vacuum chamber was mounted inside the 150 mm bore of the superconducting magnet. This system was equipped with one ZnSe laser window on the 4 inch cell flange.

The z-axis elongated stainless steel cell (2.5 x 2.5 x 4.5 cm) used in all charge-transfer reaction studies has been described in chapter 2. Briefly, the cell consists of four 2.5 cm x 4.5 cm x 0.63 mm stainless steel plates (a pair of excite plates and a pair of detect plates) and two 2.5 cm x 2.5 cm x 0.63 mm trapping plates. These six electrodes were isolated and held together by a pair of 4.0 cm x 4.0 cm x 1.25 cm MACOR spacers. Both MACOR spacers were machined with a 2.0 cm diameter hole in the center for laser beam entrance. The trapping plates were each made with a 2 cm diameter hole over which 90% transparent stainless steel mesh was spot welded to maintain the required trapping potential. A trapping potential of -2.0 V was used in all experiments.

Carbon cluster ions were produced by focusing (7.63 cm focal length ZnSe lens) the 10.6  $\mu\text{m}$  output from a Lumonics CO<sub>2</sub> laser through the front and back trap plates onto a graphite plug mounted behind the back trap plate of the cell. The plume of carbon cluster ions, neutrals, and electrons produced by the laser desorption of the graphite plug traveled along

the magnetic field and entered the cell through the back trap plate.

Two different types of pulse sequences were used in this study and they have been described in chapter 2. Briefly, the first type involved a quench pulse applied to both trap plates to eject any ions present in the cell. The laser was then triggered and a pulsed valve was opened briefly to allow argon to enter the cell (peak pressure  $5 \times 10^{-6}$  Torr). Next, a 2000 ms delay time allowed the ions to be thermalized by ion-neutral collisions with argon. This delay time also allowed most of the thermalizing gas to be pumped out of the vacuum chamber. A series of ion ejection sweeps was then used to isolate the cluster cation of interest. After the cluster ion was isolated, a variable reaction time allowed the charge-transfer reaction to take place. In the second type of pulse sequence, continuous ejection of a side reaction product took place during the charge-transfer reaction period. Ions were excited by the standard frequency chirp excitation method and 16K time-domain points were acquired during broad-band detection (15-400 amu).

For each reaction delay time, 50 scans were averaged to enhance the signal to noise ratio. The intensities of the reacting cluster ion and product ions formed by ion-molecule reaction(s) were followed for a time period which ranged from 1 to 10 s. Integrated peak intensities for all major ions were obtained at 15 to 20 different reaction delay periods of

approximately equal spacing during each experiment. Plots of relative ion intensity vs. reaction time were then made to demonstrate the occurrence or non-occurrence of charge-transfer reactions.

The charge-transfer reagents, listed in Table 1, were introduced into the vacuum chamber usually to a pressure of  $1 - 3 \times 10^{-8}$  Torr above the background pressure. If the charge-transfer reaction was not observed at these low pressures, the neutral pressure was increased to a pressure of  $1.0 \times 10^{-7}$  Torr to further confirm the occurrence or non-occurrence of reaction. The charge-transfer reference compounds were obtained from commercial sources and used without further purification. However, liquid reference compounds were purified by several freeze-pump-thaw cycles and solid reference compounds were pumped on for 1-2 minutes before they were leaked into the vacuum chamber. Most of the EA reference compounds were less volatile solids and they were heated on the leak valve inlet using heating tape controlled by a Variac to produce sufficient vapor pressure. The presence of a reference compound in the cell region was checked by using electron ionization.

### Results

Mass spectra of carbon cluster cations formed from the graphite rod by laser desorption using the  $10.60 \mu\text{m}$  wavelength

Table 6.1 Charge-transfer reference compounds used in this chapter and their EA's.

Reference compound	Electron Affinity <sup>a</sup> (eV)
Tetracyanoethylene	3.17
Tetrachloro-1,4-benzoquinone	2.72
Tetrafluoro-1,4-benzoquinone	2.64
2,6-Dichloro-1,4-benzoquinone	2.48
2,5-Dichloro-1,4-benzoquinone	2.44
2,3-Dichloro-1,4-naphthoquinone	2.19
3,5-Dinitrobenzene	2.19
1,4-Dinitrobenzene	2.04
1,4-Benzoquinone	1.91
1,4-Naphthoquinone	1.81
3-Nitro-trifluorotoluene	1.41
1-Fluoro-3-nitrobenzene	1.23

a) Lias, S. G.; Bartmess, J. E.; Liebman, J. F.; Holmes, J. L.; Levin, R. D.; Mallard, W. G. *J. Phys. Chem. Ref. Data* 1988, 17.

output from the Lumonics pulsed CO<sub>2</sub> laser are shown in Figures 2.4 and 6.1. The cluster ion distribution can be observed to depend on the laser energy. Figure 6.1a shows the cluster distribution obtained with 500 mJ/pulse of laser energy; intense peaks (decreasing intensity) were observed for C<sub>8</sub><sup>-</sup>, C<sub>6</sub><sup>-</sup>, C<sub>7</sub><sup>-</sup>, C<sub>9</sub><sup>-</sup>, C<sub>5</sub><sup>-</sup>, C<sub>4</sub><sup>-</sup> C<sub>10</sub><sup>-</sup>, C<sub>11</sub><sup>-</sup>, C<sub>12</sub><sup>-</sup> and C<sub>3</sub><sup>-</sup>. Increasing the laser energy to 900 mJ/pulse caused the cluster distribution to shift as shown in Figure 6.1b. At this laser energy intense peaks were observed for C<sub>6</sub><sup>-</sup>, C<sub>4</sub><sup>-</sup>, C<sub>5</sub><sup>-</sup>, C<sub>8</sub><sup>-</sup>, C<sub>7</sub><sup>-</sup>, C<sub>9</sub><sup>-</sup>, C<sub>10</sub><sup>-</sup>, C<sub>3</sub><sup>-</sup>, C<sub>2</sub><sup>-</sup>, C<sub>11</sub><sup>-</sup>, C<sub>12</sub><sup>-</sup> and C<sub>13</sub><sup>-</sup>.

Results of charge-transfer reactions between C<sub>n</sub><sup>-</sup> and neutral reference compounds are listed in Table 6.2. The cluster electron affinities reported here were taken as the value midway between the electron affinities of neutrals for which charge-transfer was and was not observed. For example, C<sub>4</sub><sup>-</sup> did undergo charge-transfer with 1,4-Naphthoquinone (1.81 eV) but did not charge-transfer with 3-Nitro-trifluorotoluene (1.41 eV). Since the EA of C<sub>4</sub> can lie anywhere between 1.41 and 1.81 eV, the uncertainty is reported as  $\pm \frac{1}{2}$  the gap size. In this particular case, the gap is 0.4 eV, giving an uncertainty of 0.2 eV for C<sub>4</sub>.

Table 6.3 compares the electron affinities determined in this study with some previously reported experimental and theoretical values. Although electron affinities have been bracketed successfully by the charge-transfer technique, some limitations are attached to this method, perhaps the most

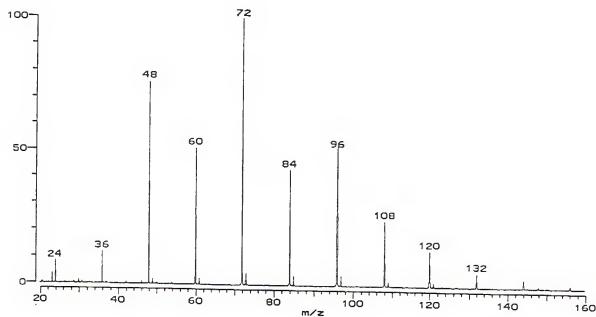
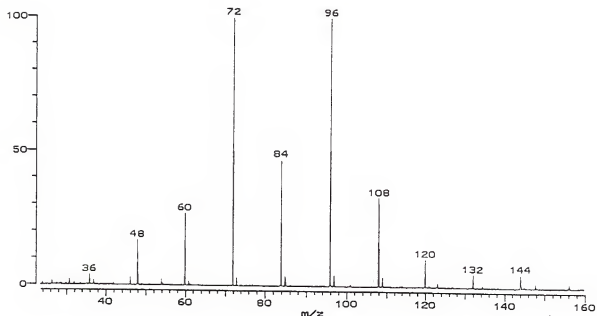


Figure 6.1 Mass spectra of carbon cluster anions observed following laser vaporization of a graphite plug by  $10.60\text{ }\mu\text{m}$  wavelength light from a  $\text{CO}_2$  laser with (top) 500 mJ/pulse and (bottom) 900 mJ/pulse

Table 6.2 Results from reaction between  $C_n^-$  and charge-transfer reference compounds.

Reference Compound (Neutral)	EA <sup>a</sup>	MW	$C_4^-$	$C_5^-$	$C_6^-$	$C_7^-$	$C_8^-$	$C_9^-$
Tetracyanoethylene	3.17	128	Y	Y	Y	Y	N	N
Tetrachloro-1,4-benzoquinone	2.72	244						
Tetrafluoro-1,4-benzoquinone	2.64	168	Y	Y	Y	N	N	N
2,6-Dichloro-1,4-benzoquinone	2.48	177	Y	Y	N	N	N	N
2,5-Dichloro-1,4-benzoquinone	2.48	177						
2,3-Dichloro-1,4-naphthoquinone	2.19	227						
3,5-Dinitrobenzene	2.10	168						
1,4-Dinitrobenzene	2.00	168	Y	N	N	N	N	N
1,4-Benzoquinone	1.81	108						
1,4-Naphthoquinone	1.81	108	Y	N	N	N	N	N
3-Nitro-trifluorotoluene	1.81	191	N	N	N	N	N	N
1-Fluoro-3-nitrobenzene	1.23	141	N	N	N	N	N	N

N = Charge-transfer between the anion and the reference compound was not observed.

Y = Charge-transfer was observed.

a) Lias, S. G.; Bartmess, J. E.; Liebman, J. F.; Holmes, J. L.; Levin, R. D.; Mallard, W. G. *J. Phys. Chem. Ref. Data* 1988, 17.

Table 6.3 Comparison of experimental and theoretical EA's of C<sub>4</sub> - C<sub>9</sub>

C <sub>n</sub>	AEA from this study	AEA <sup>a</sup> from previous Bracketing Exp	VEA Experimental	VEA Theory	AEA Theory
C <sub>4</sub>	1.58 ± 0.17	1.3 ± 0.1 <sup>a</sup>	3.70 <sup>b</sup> , 3.88 <sup>d</sup> ,	3.41 <sup>c</sup> , 3.39 <sup>e</sup> 3.47 <sup>g</sup> , 3.47 <sup>h</sup> 3.29 <sup>i</sup> , 2.02 <sup>i</sup>	3.49 <sup>e</sup> , 3.69 <sup>f</sup> 3.52 <sup>g</sup> , 3.83 <sup>h</sup>
C <sub>5</sub>	2.24 ± 0.24	1.5 ± 0.1 <sup>a</sup>	2.80 <sup>b</sup> , 2.83 <sup>d</sup>	2.43 <sup>c</sup> , 2.42 <sup>g</sup> 2.73 <sup>h</sup>	2.82 <sup>f</sup> , 2.49 <sup>g</sup> 2.76 <sup>h</sup>
C <sub>6</sub>	2.56 ± 0.08	1.5 ± 0.1 <sup>a</sup>	4.10 <sup>b</sup> , 4.2 <sup>d</sup>	3.69 <sup>c</sup> , 3.81 <sup>g</sup>	3.87 <sup>g</sup>
C <sub>7</sub>	2.91 ± 0.27	1.6 ± 0.1 <sup>a</sup>	3.10 <sup>b</sup> , 3.36 <sup>d</sup>	2.88 <sup>g</sup> ,	2.95 <sup>g</sup>
C <sub>8</sub>	> 3.17	1.6 ± 0.1 <sup>a</sup>	4.42 <sup>b</sup> , 4.38 <sup>d</sup>	4.00 <sup>g</sup>	4.07 <sup>g</sup>
C <sub>9</sub>	> 3.17		3.70 <sup>b</sup> , 3.68 <sup>d</sup>	3.14 <sup>g</sup>	3.21 <sup>g</sup>

AEA=adiabatic electron affinity and VEA=vertical electron affinity

- a - reference 299  
 b - reference 280  
 c - reference 290  
 d - reference 284  
 e - reference 291  
 f - reference 292  
 g - reference 288  
 h - reference 287  
 i - reference 293, the lower value was calculated for the cyclic rhombic form of C<sub>4</sub>.

serious one is reactions other than charge transfer for which the carbon cluster anions undergo with charge-transfer reference compounds. However, the capability of FTICR mass spectrometry to eject an ion while following a charge-transfer reaction allowed most of the complications caused by the side reactions to be overcome. Although these side ion-molecule reactions caused difficulties in bracketing the EA's of small carbon clusters, they gave some insight into the reactivity of small carbon clusters. The products of each side reactions are listed in Table 6.4.

The existence of relatively few charge-transfer reference compounds in a given EA range further limits the application of this technique to small carbon clusters. In particular, the unavailability of electron affinity reference compounds above 3.17 eV limited the bracketing of C<sub>8</sub> and C<sub>9</sub> in this study. Other limitations of the charge-transfer bracketing technique have been discussed in detail (293).

#### Discussion

#### Carbon Cluster Distribution

Spectra of carbon cluster anions, C<sub>n</sub><sup>-</sup>, produced by direct laser ablation of a graphite plug are shown in Figures 6.1a and 6.1b. A similar distribution was observed in previous FTICR studies using different lasers (282,300-301). The

Table 6.4  $C_n^-$  reactions other than charge-transfer with charge-transfer reference compounds.

Reference Compound (Neutral)	Ions other than $M^-$ observed
Tetracyanoethylene (M)	$[M+C_n+CN]^-$ , $[M+C_n+(CN)_2]^-$ , $[M-CN]^-$ , $[C_n(CN)_2]^-$ , $[M+C_n-CN]^-$
Tetrachloro-1,4-benzoquinone (M)	$^{35}Cl^-$ , $^{37}Cl^-$
Tetrafluoro-1,4-benzoquinone (M)	$[M+C_n-CO]^-$ , $[M+C_n-(CO)_2]^-$ $[(M)_2+C_n-CO]^-$ , $[(M)_2+C_n-(CO)_2]^-$
2,6-Dichloro-1,4-benzoquinone (M)	$^{35}Cl^-$ , $^{37}Cl^-$
1,4-Dinitrobenzene (M)	$[M-NO]^-$ , $[M+C_n-NO]^-$
1,4-Naphthoquinone (M)	$[M+C_n]^-$ , $[(M)_2C_n]^-$

carbon cluster anions produced range in size from 2 to 13 atoms. Usually a "bell-shaped" distribution with  $C_4^-$ ,  $C_5^-$ ,  $C_6^-$ ,  $C_7^-$ ,  $C_8^-$  and  $C_9^-$  species in the middle and  $C_2^-$ ,  $C_3^-$  and  $C_{10}^- - C_{13}^-$  species at the edges was observed. The even/odd alternation in abundance observed in Figures 6.1 a and 6.1b is consistent with previous studies (282,300-301). Laser ablation of the graphite plug using both the 532 nm output from a Nd: YAG laser (300) and the 10.6  $\mu m$  output from a pulsed CO<sub>2</sub> laser failed to produce cluster anions with more than 13 atoms. The absence of clusters  $> C_{13}^-$  has been documented in earlier laser desorption (300) and ion bombardment (257) studies.

As shown in Table 6.3, EA's of carbon clusters containing from 4 through 9 atoms were bracketed using the charge-transfer technique. It was not possible to produce sufficient  $C_2^-$ ,  $C_3^-$  and  $C_{10}^- - C_{13}^-$  species. Therefore, ion isolation, thermalization, and charge-transfer reactions were not possible. Our attempts to produce enhanced abundance of these species by varying the laser energy were not successful. As shown in Figures 6.1a and 6.1b, varying the laser energy only shifts the most abundant species among  $C_4^-$ ,  $C_6^-$  and  $C_8^-$ . Additional experiments involving chemical ionization to produce  $C_2^-$  and  $C_3^-$  and applying the bracketing technique are in progress. Comparison of the bracketed EA's of  $C_2$  and  $C_3$  with well established EA values available in the literature (266) will allow us to verify the validity of the electron affinities bracketed in this chapter.

Although EA's have been bracketed in a reliable and straightforward manner by the charge-transfer bracketing method, some limitations are attached to this technique. Two such limitations have already been discussed in the experimental section. The third limitation is incomplete thermalization of the carbon cluster anions before the charge-transfer reaction time period. If complete thermalization were not achieved the bracketed EA would be lower than the actual EA. Such incomplete thermalization of the anions could have caused the earlier EA's determined using this technique (299) to be lower than the values reported here.

Since the FTICR mass spectrometer is capable of trapping ions for a long time periods, thermalization is not a difficult task. Thermalization is achieved by trapping the ions in the FTICR cell and allowing them to undergo many collisions with a neutral thermalizing gas (Ar, N<sub>2</sub>, or SF<sub>6</sub>). Thermalization depends on: thermalization time; gas pressure; and gas molecular complexity. The maximum pressure of the thermalizing gas is limited by the pumping system available with the mass spectrometer and the thermalizing time depends on the trapping capabilities of the FTICR cell. A thermalizing time of 2000 ms and peak pressure of  $5 \times 10^{-6}$  Torr argon were used in these experiments. For each of the bracketed EA's, the charge-transfer reactions which determined the upper and the lower boundaries were studied with and without the thermalizing gas. The occurrence of these

reactions showed no dependence on the introduction of the thermalizing gas; however, their rates often did.

#### Charge-Transfer Reactions Versus Side Reactions

The electron affinity of  $C_4^-$  is bracketed in this experiment between that of 1,4-naphthoquinone (1.81 eV) and 3-nitro-trifluorotoluene (1.41 eV). The time plot of normalized ion intensities vs. reaction time for the reaction of  $C_4^-$  with 1,4-naphthoquinone is shown in Figure 6.2. Representative mass spectra obtained at reaction times of 800 and 5000 ms are shown in Figures 6.3a and 6.3b, respectively. As shown in these mass spectra and the time plots, 1,4-naphthoquinone underwent non-charge transfer reactions with  $C_4^-$  along with charge-transfer reaction. The types of non-charge transfer reactions which hindered the straightforward determination of EA of small carbon clusters are listed in Table 6.4. The non-charge transfer products formed during the reaction between  $C_4^-$  and 1,4-naphthoquinone were  $[C_4^- + (1,4\text{-naphthoquinone})]^-$  ( $m/z$  206) and  $[C_4^- + (1,4\text{-naphthoquinone})_2]^-$  ( $m/z$  364). The continuous ejection capability of the FTICR mass spectrometer was used in these reactions to ensure that charge-transfer was occurring in a straightforward manner rather than by some multiple reaction pathway. First,  $[C_4^- + (1,4\text{-naphthoquinone})]^-$  was continuously ejected during the charge-transfer reaction time and  $C_4^-$ ,  $[(1,4\text{-naphthoquinone})]^-$  and

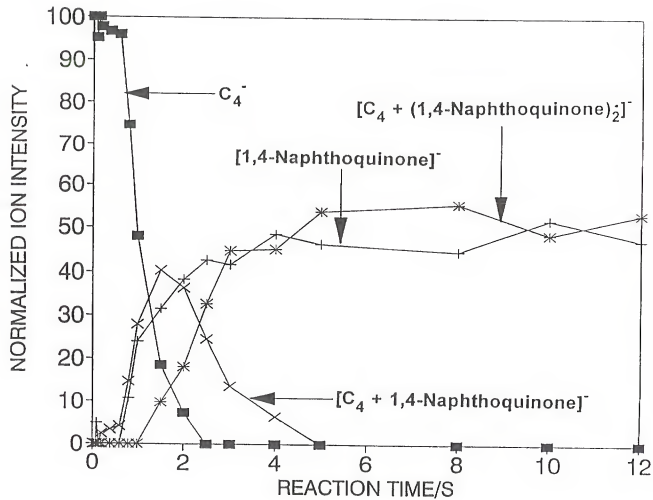


Figure 6.2 Ion intensity vs. reaction time plot for the reaction of  $\text{C}_4^-$  with 1,4-naphthoquinone.

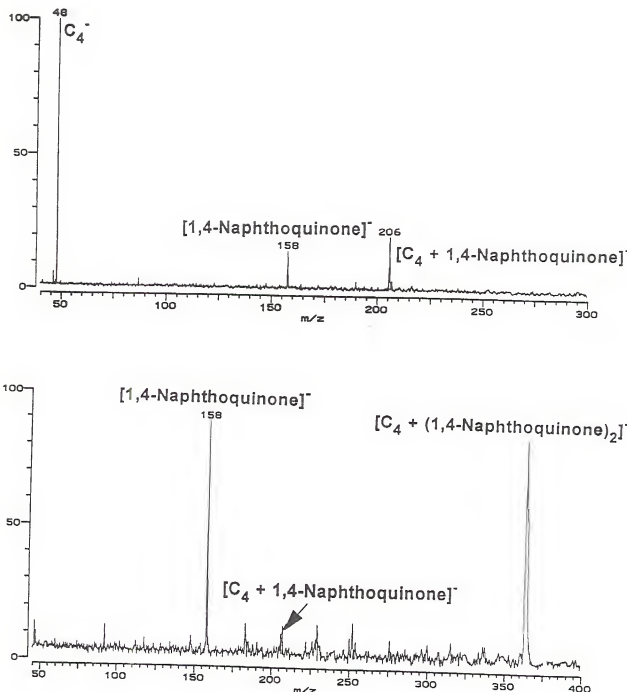


Figure 6.3 Mass spectra following  $C_4^-$  reaction with 1,4-naphthoquinone obtained at reaction times of: (top) 800 ms and (bottom) 5000 ms.

$[C_4^- + (1,4\text{-naphthoquinone})_2]^-$  were monitored. Similarly,  $[C_4^- + (1,4\text{-naphthoquinone})_2]^-$  was continuously ejected and the reaction was repeated. These separate runs showed exponentially decaying intensity for  $C_4^-$  and increasing intensity for  $[(1,4\text{-naphthoquinone})]^-$  indicating that charge-transfer was occurring in a straightforward manner.

Since  $C_5^- - C_9^-$  did not undergo charge-transfer with 1,4-naphthoquinone, these reactions were not complicated to study. For example, the time plot obtained for reaction of  $C_6^-$  with 1,4-naphthoquinone is shown in Figure 6.4. During the reaction of  $C_6^-$  with 1,4-naphthoquinone,  $[C_6^- + (1,4\text{-naphthoquinone})]^-$  ( $m/z$  230) was formed as a primary product and  $[C_6^- + (1,4\text{-naphthoquinone})_2]^-$  ( $m/z$  388) was formed as a secondary product. Mass spectra obtained at reaction times of 100, 1500, 4000 and 10000 ms to plot this time graph are shown in Figures 6.5a, 6.5b, 6.6a 6.6b, respectively.

To confirm the upper and lower boundaries of the EA bracket for  $C_n^-$ , usually reactions with one additional reference compound above and below the bracketing compound was performed. To support the EA bracket of  $C_4^-$ , charge-transfer experiments were carried out with 1,4-dinitrobenzene and 1-fluoro-3-nitrobenzene. Figure 6.7 shows the time plot obtained by following the charge-transfer reaction between  $C_4^-$  and 1,4-dinitrobenzene for 10 s. Mass spectra obtained at reaction times of 500 and 10,000 ms are shown in Figures 6.8a and 6.8b, respectively. In addition to charge-transfer

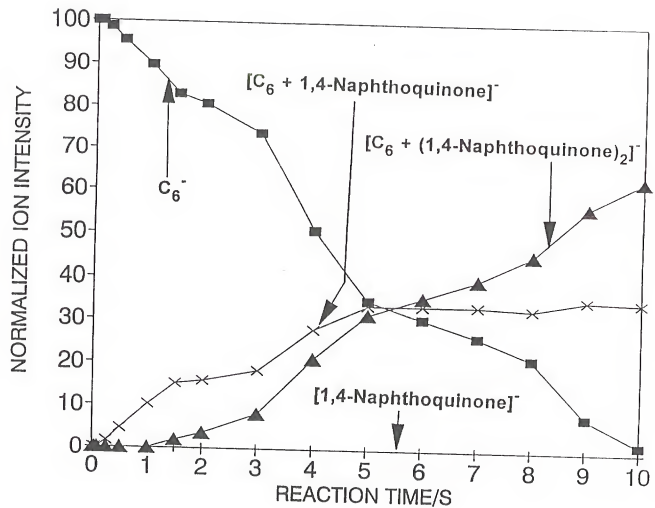


Figure 6.4

Ion intensity vs. reaction time plot for the reaction of  $C_6^-$  with 1,4-naphthoquinone.

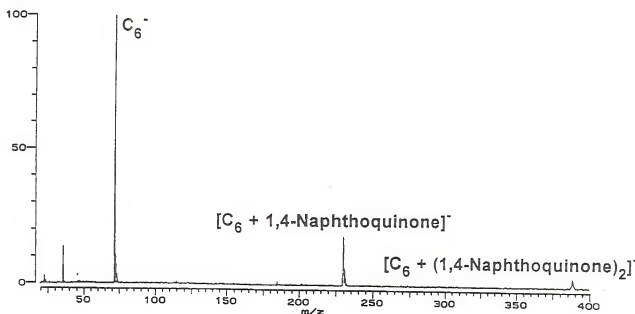
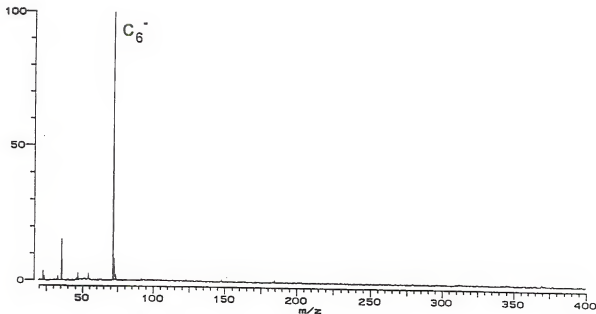


Figure 6.5 Mass spectra following C<sub>6</sub><sup>-</sup> reaction with 1,4-naphthoquinone obtained at reaction times of: (top) 100 ms and (bottom) 1500 ms.

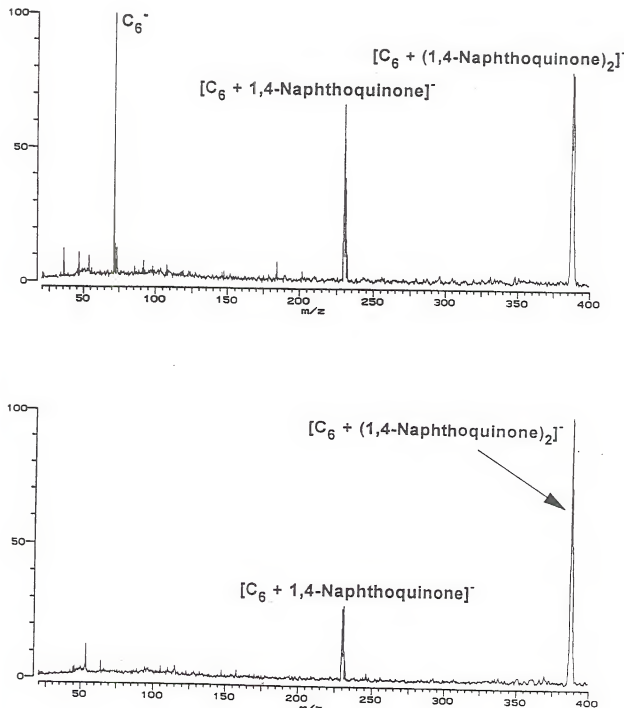


Figure 6.6 Mass spectra following  $C_6^-$  reaction with 1,4-naphthoquinone obtained at reaction times of: (top) 4000 ms and (bottom) 10000 ms.

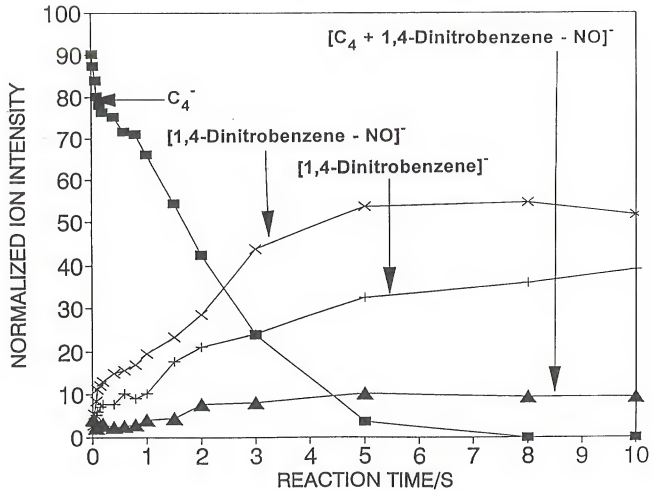


Figure 6.7 Ion intensity vs. reaction time plot for the reaction of  $\text{C}_4^-$  with 1,4-dinitrobenzene.

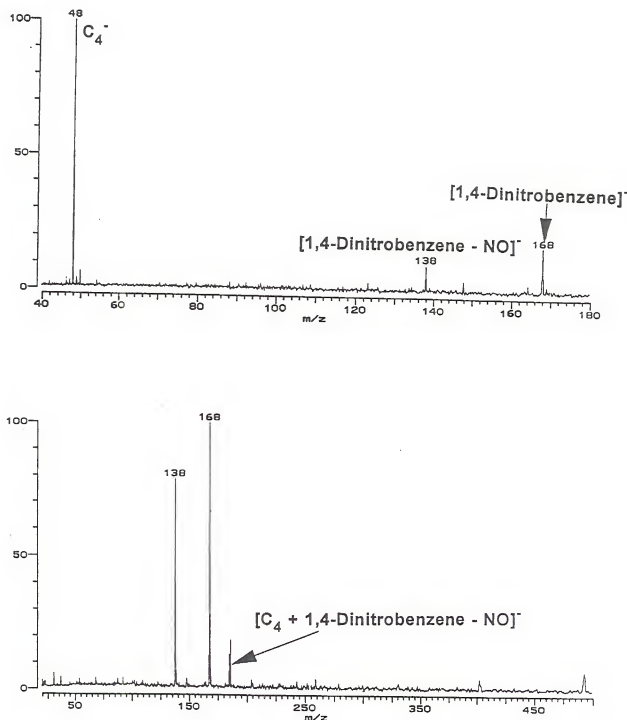


Figure 6.8 Mass spectra following  $C_4^-$  reaction with 1,4-dinitrobenzene obtained at reaction times of: (top) 500 ms and (bottom) 10000 ms.

reaction, side reactions result in the formation of [1,4-dinitrobenzene -NO]<sup>-</sup> (m/z 138) and [C<sub>4</sub> + 1,4-dinitrobenzene -NO]<sup>-</sup> (m/z 186). These side reaction products were continuously ejected one by one during the charge-transfer reaction delay time to confirm the straightforward charge-transfer between C<sub>4</sub><sup>-</sup> and 1,4-dinitrobenzene.

All charge-transfer reference compounds which contained Cl (from 2,3-dichloro-1,4-naphthoquinone to tetrachloro-1,4-benzoquinone) were very reactive with small carbon cluster anions. Such side reactions prevented the use of 2,3-dichloro-1,4-naphthoquinone, 2,5-dichloro-1,4-benzoquinone and tetrachloro-1,4-benzoquinone from the bracketing experiments.

Charge-transfer reactions between C<sub>n</sub><sup>-</sup> and 2,6-dichloro-1,4-benzoquinone were difficult to study due to the formation of <sup>35</sup>Cl<sup>-</sup> and <sup>37</sup>Cl<sup>-</sup>. For example, Figure 6.9 shows the time plot obtained during the reaction of C<sub>5</sub><sup>-</sup> with 2,6-dichloro-1,4-benzoquinone. During this reaction <sup>35</sup>Cl<sup>-</sup> and <sup>37</sup>Cl<sup>-</sup> species formed more rapidly than the charge-transfer products at m/z 176 and 178. Thus, continuous ejection of <sup>35</sup>Cl<sup>-</sup> or <sup>37</sup>Cl<sup>-</sup> species was necessary to observe the direct charge-transfer reaction between C<sub>5</sub><sup>-</sup> and 2,6-dichloro-1,4-benzoquinone. Such experiments were performed by applying an rf pulse to eject the <sup>37</sup>Cl<sup>-</sup> continuously during the charge-transfer reaction delay time. The rf-pulse was applied with a larger amplitude than necessary hoping that the excess energy could eject most of the neighboring <sup>35</sup>Cl<sup>-</sup> species. A mass spectrum obtained by

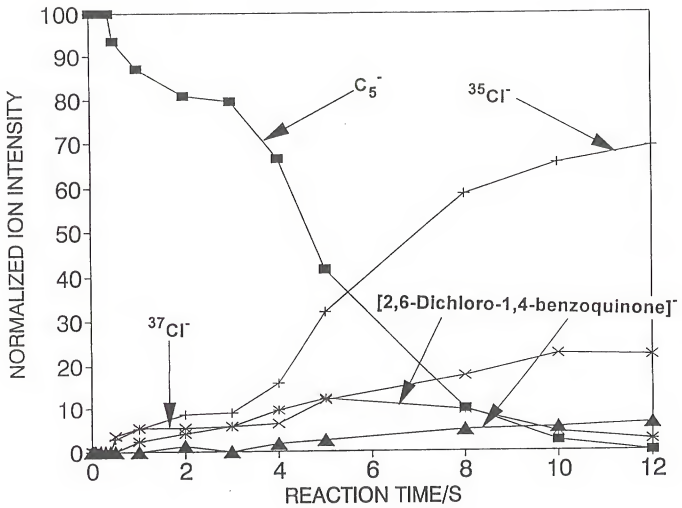


Figure 6.9 Ion intensity vs. reaction time plot for the reaction of  $C_5^-$  with 2,6-dichloro-1,4-benzoquinone.

ejecting  $^{37}\text{Cl}^-$  continuously during the charge-transfer reaction delay time (5000 ms) is shown in Figure 6.10. Although all the  $^{37}\text{Cl}^-$  species have been ejected, some  $^{35}\text{Cl}^-$  species are still present during the reaction. Similarly,  $^{35}\text{Cl}^-$  was continuously ejected and the reaction was repeated. These separate runs showed exponentially decaying intensity for  $\text{C}_5^-$  and increasing intensity for [2,6-dichloro-1,4-benzoquinone] $^-$  ( $m/z$  176 and 178) indicating that charge-transfer was occurring in a straightforward manner.

A typical time-plot obtained when charge-transfer reactions do not take place between the reference compound and the  $\text{C}_n^-$  is shown in Figure 6.11. This particular reaction involved  $\text{C}_8^-$  and 2,6-dichloro-1,4-benzoquinone. A mass spectrum obtained at a reaction time of 5000 ms is shown in Figure 6.12. There is some evidence of [2,6-dichloro-1,4-benzoquinone] $^-$  ( $m/z$  176 and 178),  $^{35}\text{Cl}^-$  and  $^{37}\text{Cl}^-$  in the mass spectrum. Since the normalized intensity of [2,6-dichloro-1,4-benzoquinone] $^-$  did not exceed 25% of the zero time normalized intensity of  $\text{C}_8^-$ , we have attributed no charge-transfer to this reaction. This rule was applied throughout this study.

EA's of  $\text{C}_4 - \text{C}_9$

Table 6.3 compares the EA's obtained in this chapter with some previously reported experimental and theoretical values.

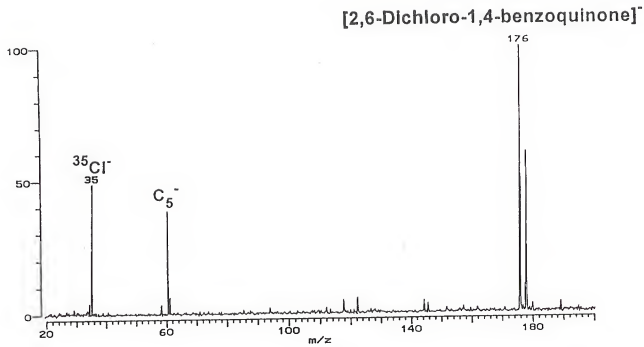


Figure 6.10 Mass spectrum following  $\text{C}_5^-$  reaction with 2,6-dichloro-1,4-benzoquinone obtained at 5000 ms reaction time while continuously ejecting  $^{37}\text{Cl}^-$ .

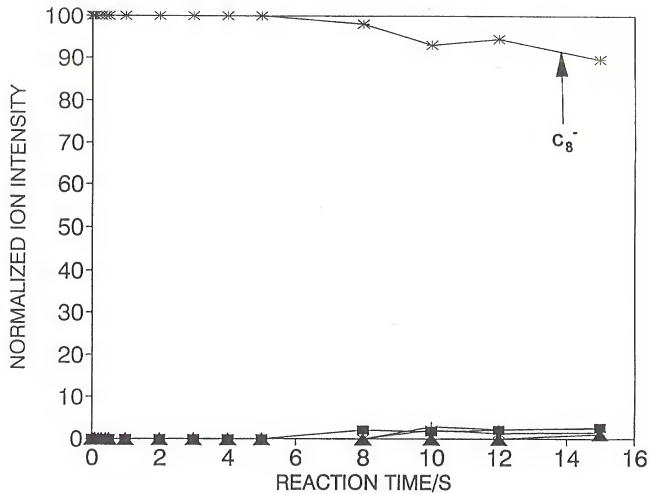


Figure 6.11 Ion intensity vs. reaction time plot for the reaction of  $C_8^-$  with 2,6-dichloro-1,4-benzozquinone.

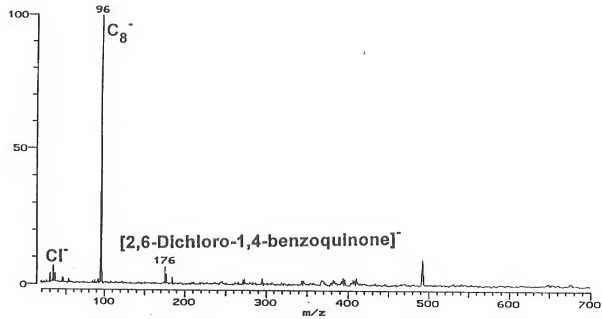


Figure 6.12 Mass spectrum following  $C_8^-$  reaction with 2,6-dichloro-1,4-benzoquinone obtained at 6000 ms reaction time.

Experimental EA's available in the literature for carbon clusters were obtained using photoelectron spectroscopy. The first ultraviolet photoelectron spectra for  $C_2^- - C_{29}^-$  were obtained by Smalley et al. (280). These spectra were obtained with a resolution of ca.  $1000\text{ cm}^{-1}$  which allowed only the electronic states to be resolved. The EA values obtained were vertical rather than adiabatic. Recently, Neumark et al. (286) obtained photoelectron spectra for  $C_2^- - C_{11}^-$  with a resolution of about  $100\text{ cm}^{-1}$ . This allowed them to resolve the vibrational states and assign electron affinities closer to adiabatic rather than vertical.

Columns five and six of Table 6.3 show the theoretical EA's available for small carbon clusters. Vertical electron affinities of linear  $C_3 - C_6$  were obtained by Adamowicz using an *ab initio* procedure which combined the first order correlation method and the coupled cluster method. These values were systematically lower than the experimental values obtained by Smalley et al. (280) and Neumark (284). Both vertical and adiabatic EA's for linear carbon clusters containing from 2 to 11 atoms were calculated by Watts and Bartlett (288). Recently, EA's of linear  $C_2 - C_5$  were calculated by the same group using more accurate geometries (287).

The experimental EA value available for  $C_4$  was determined by Smalley et al. (280) using PES to be 3.70 eV. Later, higher resolution PES experiments by Neumark et al. (284)

yielded 3.882 eV. Using the many-body perturbation theory (MBPT) and the coupled cluster methods Watts and Bartlett (287) calculated vEA and aEA of  $C_4$  to be 3.72 and 3.83 eV, respectively. All the other EA values determined experimentally and calculated theoretically are listed in Table 6.3. Our EA of  $1.58 \pm 0.2$  eV for  $C_4$  agrees poorly with all the literature values. The bracketed EA agrees somewhat with the value of 2.02 eV calculated by Bernholdt et al. (293) for cyclic rhombic form and agrees poorly with EA calculated for linear form, 3.29 eV. However, side ion-molecule reactions between carbon cluster anions and the reference compounds indicate that only one isomer of the  $C_n^-$  is formed during the laser desorption of a graphite plug and the clusters are linear in structure (*vide infra*) (300). The reason for the disagreement is unclear.

The EA ( $2.24 \pm 0.24$ ) of  $C_5$  agrees somewhat with theoretical AEA'S 2.49, 2.76 and 2.82 (287-288, 292) available in the literature. The bracketed EA of  $C_6$  ( $2.56 \pm 0.1$ ) is in poor agreement with the AEA, 3.87 eV, calculated by Bartlett et al. (288). However, photodetachment studies of carbon cluster anions performed in the presence of  $CCl_4$  indicated that EA of  $C_6$  is lower than 4.0 eV (282). This suggests that true adiabatic EA is less than the values (4.1 and 4.2) reported by Smalley et al. (280) and Neumark et al. (284). The EA reported in Table 6.3 for  $C_7$  agrees very well with the theoretical EA (2.95 eV) reported by Bartlett et al. (288).

In addition, our bracketed EA is in close agreement with the values reported by Smalley et al. (3.10 eV) (280) and Neumark et al. (3.36 eV) (284). Since reference compounds with EA's above 3.17 eV were not available, EA's of  $C_8^-$  and  $C_9^-$  were not bracketed in this study. Both  $C_8^-$  and  $C_9^-$  did not undergo charge-transfer with any of the available reference compounds. This indicated that the EA's of  $C_8^-$  and  $C_9^-$  are higher than 3.17 eV. However, the photodetachment studies of  $C_n^-$  by Dunbar et al. (282) suggest that the EA values for these clusters are lower than 4 eV. Adiabatic EA values of 4.07 and 3.21 eV calculated by Bartlett et al. (288) for  $C_8^-$  and  $C_9^-$ , respectively, support Dunbar's prediction. However, they do not support the values obtained by Smalley et al. (280) and Neumark et al. (284).

Ion-molecule reactions between laser vaporized carbon cluster anions and either  $F_2$  or  $C_2N_2$  were studied by McElvany (300). This study indicated that only linear  $C_n^-$  are formed during direct laser vaporization of a graphite plug. In addition, no structural isomers of  $C_n^-$  were observed. In that study, reactions of  $C_n^-$  with  $F_2$  resulted in addition of F or reduction in cluster size and loss of neutral  $CF_2$ . Primary ion-molecule reaction products were  $C_nF^-$  and  $C_{n-1}^-$ . These products were observed to further react with  $F_2$  to form  $C_{n-1}F^-$  and  $CF_2$ . During the ion-molecule reactions between carbon cluster anions and  $F_2$ , both even and odd clusters gave the same products but with different branching ratios. In

contrast, ion-molecule reactions between  $C_2N_2$  and carbon cluster anions gave different products for even and odd clusters. The even carbon cluster anions,  $C_n^-$ , reacted with  $C_2N_2$  to produce  $C_nCN^-$  and  $C_nC_2N_2^-$  but the odd  $C_n^-$  reacted with  $C_2N_2$  to give only  $C_nC_2N_2^-$ . These ion-molecule reaction pathways allowed McElvany to predict that carbon cluster anions containing from 4 through 13 atoms produced by laser vaporization are linear and only one isomer is present for each  $C_n^-$ . In addition, polyacetylenic ( $[ \cdot C \equiv C - C = C \equiv C \cdot ]^-$ ) and cumulenic ( $[ : C = C = C = C = C : ]^-$ ) structures for even and odd  $C_n^-$  respectively, were suggested.

A similar reaction pathway was observed during the reaction between  $C_n^-$  and tetracyanoethylene ( $C_2(CN)_4$ ). Both  $C_nCN^-$  and  $C_nC_2N_2^-$  along with  $[C_2(CN)_4C_nCN]^-$ ,  $[C_2(CN)_4C_nC_2N_2]^-$  and  $[C_2(CN)_3C_n]^-$  were detected during this reaction. In addition, other side reactions listed in Table 6.4 indicate the sequential formation of all the adduct species. Particularly, the reactions between 1,4-naphthoquinone and  $C_n^-$  result in the formation of  $[C_n + 1,4\text{-naphthoquinone}]^-$  as the primary product and  $[C_n + (1,4\text{-naphthoquinone})_2]^-$  as the secondary product. These observations suggest that these ion-molecule reactions may be occurring at two carbene ends of the linear carbon cluster ions. As to the presence of structural isomers of  $C_n^-$ , clearly the time plots (Figures 6.3 and 6.8) indicate that only one form of  $C_n^-$  is produced during laser desorption of a graphite plug.

CONCLUSIONS

The charge-transfer bracketing technique which has been proven valuable in bracketing the IP's of carbon clusters (291-293) has been successfully extended to the bracketing of EA's of small carbon clusters ( $C_n$ ,  $n=4-9$ ). The EA's determined in this study are closer to adiabatic rather than vertical values. The EA's of  $C_4$  and  $C_6$  agree poorly with most of the literature values. The reason for this disagreement is not clear. However, EA's of  $C_5$ ,  $C_7$ ,  $C_8$  and  $C_9$  agree reasonably with literature values. No evidence for structural isomers of small carbon clusters was observed. During these charge-transfer studies, several side reactions were observed with the charge-transfer reference compounds. However, extensive study of these ion-molecule reactions has resulted in a better understanding of small carbon cluster reactivity. In addition these side reactions suggested that  $C_n^-$  reactions may be occurring at the carbene ends of linear carbon chains.

CHAPTER 7  
CONCLUSIONS AND FUTURE WORK

Conclusions

The primary motivation for performing the work presented in this dissertation was to develop an electrospray source and couple it with a FTICR mass spectrometer. Although I entered this endeavor with little knowledge about electrospray ionization techniques, problems posed by this coupling effort made it more interesting and gave me an opportunity to learn more about this technique. These problems are listed in chapter 1 and the steps necessary to overcome these problems are discussed in chapter 3.

The recent emergence of ESI mass spectrometry as the method of choice for investigating less volatile molecules has brought a significant amount of focus to investigation of its fundamental operating principles. Chapter 3 gives a detailed description of all the ESI source designs tried in our laboratory along with all the necessary modifications required to couple this source to a 2 Tesla FTICR mass spectrometer. Several experiments were carried out to investigate fundamental operating parameters for the internal ESI source developed in our laboratory. These ESI/FTICR parameters obtained are also presented in Chapter 3.

The home-built internal source ESI/FTICR mass spectrometer was applied to several organometallic complexes, a protein and an organic dye and the results are presented in chapter 4. These molecules were further used to demonstrate CID in the region between the skimmer and the desolvating capillary. Results showed that the internal ESI source can be used to obtain molecular weight information as well as structural information.

An external source ESI/(FTICR) mass spectrometer was used in the work reported in chapter 5 to study the organometallic complexes  $\text{Ag}_2(\text{DPM})_2(\text{BF}_4)_2$  (where DPM = bis-diphenylphosphino-methane),  $\text{Ag}_2(\text{DPM})_3(\text{BF}_4)_2$  and  $\text{Ru}(\text{II})(\text{bpy})_3(\text{PF}_6)_2$  (where bpy = 2,2'-bipyridyl). The high mass resolution and accurate mass assignment of parent and collisionally induced dissociation (CID) fragment ions provided structural information on these organometallic complexes. CID was performed on these complexes in the capillary/skimmer region and inside the FTICR analyzer cell and results from each type of experiment were compared. Important fragmentation pathways and reaction types, including bond cleavage, ligand loss, and ligand substitution were identified.

In chapter 6, the electron affinities (EA) of small carbon clusters ( $\text{C}_n$ ,  $n = 4-9$ ) were bracketed with an uncertainty of a few tenths of an eV by charge-transfer methods in a FTICR mass spectrometer. Electron affinities bracketed were compared to previously determined experimental and theoretical values.

Future Work

This section explores some of the interesting research projects which can stem from the research presented in this dissertation.

Instrument Modifications

Several problems were posed during the coupling of an internal electrospray source with a FTICR mass spectrometer and they have been discussed in this dissertation. One such problem was unstable electrospray due to heat transfer from the desolvating capillary to the sample solution. This problem was eliminated by flowing water through a 3.2 mm o.d. copper tube around the Teflon tubing delivering the sample solution. In addition to copper tubing, a high voltage wire, two wires for supplying the current required for resistive heating of the desolvating capillary and two thermocouple wires filled most of the space in the 1.7 cm i.d. electrospray probe and made it difficult to insert and pull the Delrin or PEEK spray assembly from the probe.

This problem could be eliminated by replacing the 1.9 cm o.d. x 1.73 cm i.d. probe with a 2.54 cm o.d. x 2.3 cm i.d. probe. This will require replacing the 1 m x 4 cm o.d. first differentially pumped vacuum chamber (perhaps with a 1 m x 5 cm o.d. tube), the 1.9 cm probe port and the gate valve to

accommodate a 2.54 cm o.d. electrospray probe. Replacing the electrospray probe would further require modifications of the skimmer/lens holder and the PEEK spray cavity to adapt to a 2.54 cm o.d. tube. These modifications would allow the source to be inserted and pulled from the probe with less difficulty. In addition, a 2.54 cm o.d. probe will provide more space for additional tubing (to carry a discharge suppressing gas) required for negative ion electrospray.

#### Negative Ion Electrospray

Although ESI is rapidly growing as the preferred method for producing gas-phase ions from electrolytes in solution, negative ion ES is relatively scarce compared to positive ion ES. One reason for this is the fact that discharge onset potential in the negative mode of operation is much lower than in the positive mode of operation (302). When a negative high voltage is applied to the spray needle, electrons are emitted from the tip of the spray needle from the liquid Taylor cone. The electrons emitted are accelerated due to the presence of high electric field around the spray needle. The fast electrons break down the gaseous molecules, resulting in a corona discharge. Onset of corona discharge prevents stable operation of the electrospray at higher spray needle voltages.

The corona discharge onset potential can be increased by using a counter flow (opposite direction of the spray) of gas

with a high electron affinity (e.g. SF<sub>6</sub> or O<sub>2</sub>) (302). The ESI source designs described in this dissertation could be easily modified to allow the flow of a high electron affinity gas either in the same or the opposite direction of the spray. To flow the gas against the spray, a 7 cm x 1 mm i.d. stainless steel capillary with one end closed could be positioned next to the desolvating capillary with a Vespel ferrule/brass screw assembly. A second Teflon tube could be attached next to the ferrule/brass screw assembly to introduce a discharge suppressing gas in the region between desolvating capillary and the spray needle. To flow the gas in the direction of the spray, a stainless steel nipple could be welded into the Swagelok assembly used in positioning the spray needle (Figure 3.10) and the Teflon tubing carrying the discharge suppressing gas could be attached to this nipple. Then several 0.2 mm holes could be placed on the front surface of the Swagelok assembly for the gas to exit along the spray needle. In addition to the optimization experiments discussed in chapter 3, negative mode ESI would require optimization of ion current with respect to gas flow rate and spray needle potential.

Another problem posed by this design was the presence of high pressure in the cell region during ion excitation and detection events. Addition of the shutter (page 136) reduced the pressure in the analyzer region to 2-4 x 10<sup>-8</sup> Torr during these events and improved mass resolution. The pressure in the FTICR analyzer cell could be further improved by flowing

liquid nitrogen (77 K) around either the 4 cm o.d. tubing or the 10.2 cm o.d. tube. This would provide an additional cold surface for condensing the solvent molecules.

In addition to providing better vacuum, flowing liquid nitrogen around the 4 cm o.d. tube could cool the region between the desolvating capillary exit and the skimmer and facilitate formation of solvated ions. Usually solvated metal ions are produced using supersonic expansion in molecular beam instruments. Although doubly and triply charged ions such as  $Mg^{2+}$ ,  $Ca^{2+}$ ,  $Cu^{2+}$ ,  $Zn^{2+}$ , etc. exist, molecular beam studies have been restricted to singly charged species. Preliminary experiments performed with reduced desolvating capillary temperatures suggest that methanol and water solvated cluster ions can be formed very efficiently using the internal ESI source. These weakly bound cluster ions could be probed using the lasers available in our laboratory. To demonstrate the formation of cluster ions with the internal ESI source, a 50/50 methanol/water solution of  $MnCl_2$  and  $CaF_2$  was electrosprayed and the mass spectrum obtained is shown in Figure 7.1. In addition, results presented in chapter 4 showed that  $CH_3CN$  solvated ions can be formed with the internal ESI source.

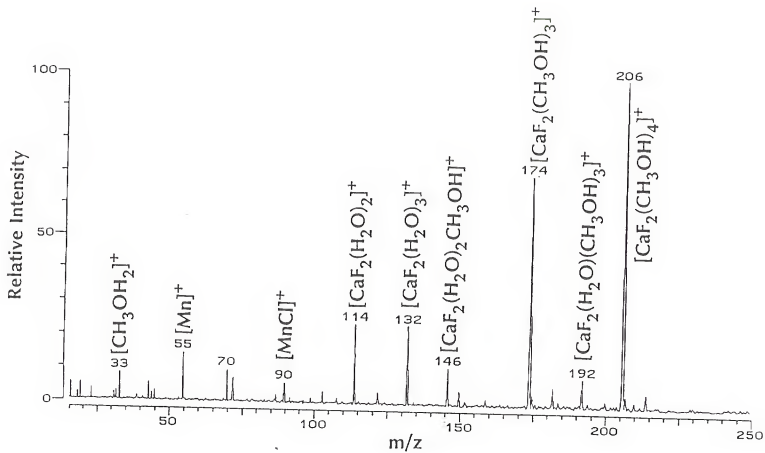


Figure 7.1 Mass spectrum obtained electrospraying  $1 \times 10^{-5}$  M  $MnCl_2$  and  $CaF_2$  in 50/50 methanol/water solution.

#### REFERENCES

1. Thomson, J. J. *Rays of Positive Electricity and Their Application to Chemical Analysis*; Longmans Green and Co.; London, 1913.
2. Hipple, J. A.; Condon, E. U. *Phys. Rev.* 1945, 68, 54.
3. Dempster, J. A. *Phys. Rev.* 1918, 11, 316.
4. Munson, M. S. B.; Field, F. H. *J. Am. Chem. Soc.* 1966, 88, 2621.
5. Beckey, H. D. *Int. J. Mass Spectrom. Ion Phys.*, 1969, 2, 500.
6. Beckey, H. D. *Principles of Field Ionization and Field Desorption Mass Spectrometry*, Pergamon Press; Oxford England, 1977.
7. Prokai, L. in *Field Desorption Mass Spectrometry*, Prokai, L., Ed., Marcel Dekker, Inc.; New York, 1990.
8. Schulten, H. R. *Int. J. Mass Spectrom. Ion Phys.* 1979, 32, 97.
9. Wada, Y.; Hayashi, A.; Fujita, T.; Matsuo, T.; Katakase, I.; Matsuda, H. *Biochim. Biophys. Acta.*, 1981, 233, 667.
10. Benninghoven, A. in *Ion Formation from Organic Solids* Benninghoven, A., Ed., Springer-Verlag; Berlin, 1983.
11. Bletsos, I. V.; Hercules, D. M.; Griefendorf, D.; Benninghoven, A. *Anal. Chem.* 1985, 57, 2384.
12. Kidwell, D. A.; Ross, M. M.; Colton, R. J. *J. Am. Chem. Soc.* 1984, 106, 2219.
13. Barber, M.; Bordoli, R. S.; Sedgwick, R. D.; Tyler, A. N. *J. Chem. Soc., Chem. Commun.* 1981, 37, 325.
14. Naylor, S.; Findeis, F.; Gibson, B. W.; Williams, D. H. *J. Amer. Chem. Soc.* 1986, 108, 6359.

15. Caprioli, R. M.; Fan, T. *Biochem. Biophys. Res. Commun.* 1986, 141, 1058.
16. Barber, M.; Green, B. N. *Rapid Commun. Mass Spectrom.* 1987, 1, 80.
17. Caprioli, R. M. *Biologically Active Molecules*, Schlunegger, U. P., ed., Springer Verlag; Berlin, 1989.
18. Caprioli, R. M. in *Continuous-Flow Fast Atom Bombardment Mass Spectrometry*, Caprioli, R. M., Ed., John Wiley and Sons; New York, 1990.
19. Torgerson, D. F.; Showronski, R. P.; Macfarlane, R. D. *Biochem. Biophys. Res. Commun.* 1974, 60, 616.
20. Jonsson, G. P.; Hedin, A. B.; Hakansson, P. L.; Sundqvist, B. U. M.; Save, B. G.; Nielsen, P. F.; Roepstorff, P.; Johansson, K. E.; Kamensky, I.; Lindberg, M. S. L. *Anal. Chem.* 1986, 58, 1084.
21. Jonsson, G. P.; Hedin, A. B.; Hakansson, P. L.; Sundqvist, B. U. M.; Bennich, H.; Roepstorff, P.; *Rapid Commun. Mass Spectrom.* 1989, 3, 190.
22. Evans, C. A.; Hendricks, C. D. *Rev. Sci. Instrum.* 1972, 43, 1527.
23. Stimpson, B. P.; Simons, D. S.; Evans, C. A. *J. Phys. Chem.* 1978, 82, 660.
24. Lai, S. T. F.; Chan, K. W.; Cook, K. D. *Macromolecules* 1980, 13, 953.
25. Honing, R. E.; Woolston, J. R. *Appl. Phys. Lett.* 1963, 2, 138.
26. Yank, L. C.; Wilkins, C. L. *Org. Mass Spectrom.* 1989, 24, 409.
27. Brown, R. S.; Wilkins, C. L. *Anal. Chem.*, 1986, 58, 3196.
28. Nuwaysir, L. M.; Wilkins, C. L. *Anal. Chem.*, 1988, 60, 279.
29. Tanaka, K.; Waki, H.; Ido, Y.; Akita, S.; Yoshida, Y.; Yoshida, T. *Rapid Commun. Mass Spectrom.* 1988, 2, 151.
30. Karas, M.; Hillenkamp, F. *Anal. Chem.* 1988, 60, 2299.
31. Beavis, R. C.; Chait, B. T. *Rapid Commun. Mass Spectrom.* 1989, 3, 233.

32. (a) Hillenkamp, F.; Karas, M.; Beavis, R. C.; Chait, B. T. *Anal. Chem.* 1991, 63, 1193A. (b) Spengler, B.; Cotter, R. J. *Anal. Chem.* 1990, 62, 793. (c) Vertes, A. *Microbeam Anal.* 1991, 26, 25.
33. Wilkins, C. L.; Castoro, J. A. *Pittcon*, 1994, Chicago, IL, paper 303.
34. Solouki, T.; Gillig, K. J.; Russell, D. H. 2nd European FTMS Work Shop, Antwerp, Belgium, September, 1993.
35. (a) Murray, K. K.; Russell, D. H. *J. Am. Soc. Mass Spectrom.* 1994, 5, 1. (b) Murray, K. K.; Lewis, T. M.; Beeson, M. B.; Russell, D. H. *Anal. Chem.* 1994, 66, 1601.
36. Feng, R.; Konishi, Y. *Anal. Chem.* 1993, 65, 645.
37. Edmonds, C. G.; Smith, R. D.; Loo, J. A.; Barinaga, C. J.; Udseth, H. R. 5<sup>th</sup> Montreux Symposium on LC/MS Freiburg, FRG., Nov. 1988.
38. (a) Dole, M.; Mack, L. L.; Hines, R. L.; Mobley, R. C.; Ferguson, L. D.; Alice, M. B. *J. Chem. Phys.* 1968, 49, 2240. (b) Zeleny, J. *J. Phys. Rev.* 1917, 10, 1
39. Dole, M.; Cox, H. L.; Giemic, J. *Adv. Chem. Ser.* 1973, 125, 73.
40. Dole, M.; Gupta, C. V.; Mack, L. L.; Nakamae, K. *Polym. Prepr. Am. Chem. Soc. Div. Polym. Chem.* 1977, 18, 188.
41. Nakamae, K.; Kumar, V.; Dole, M. 29<sup>th</sup> ASMS Conference on Mass Spectrometry and Allied Topics, Minneapolis, Mn, May 24-29, 1981.
42. Yamashita, M.; Fenn, J. B. *J. Phys. Chem.* 1984, 88, 4451.
43. Aleksandrov, M. L.; Gall, L. N.; Krasnov, V. N.; Nikolaev, V. I.; Pavlenko, V. A.; Shkurov, V. A. *Int. Dokl. Akad. Nauk. SSRR* 1984, 277, 379.
44. Stein, R. *Int. J. Mass Spectrom. Ion Phys.* 1974, 14, 205.
45. Price, D.; Milnes, G. J. *Int. J. Mass Spectrom. Ion Phys.* 1990, 99, 1.
46. Bergmann, T.; Martin, T. P.; Schaber, H. *Rev. Sci. Instrum.*, 1989, 60, 347.
47. Macfarlane, R. D. *Anal. Chem.* 1983, 55, 1247A.

48. Niehuis, E.; Heller, T.; Field, H.; Benninghoven, A. *J. Vac. Sci. Technol. A*, 1987, 5, 1243.
49. Cotter, R. J.; Tabet, J. C. *Am. Lab.* 1984, 16, 86.
50. (a) Karas, M.; Bahr, U.; GieBmann, U. *Mass Spectrom. Rev.* 1991, 10, 335. (b) Strobel, F. H.; Solouki, T.; White, M. A.; Russell, D. H. *J. Am. Soc. Mass Spectrom.* 1991, 2, 91.
51. Bakker, J. M. B. *J. Phys. E.* 1973, 6, 785.
52. Boyle, J. G.; Whitehouse, C. M. *Anal. Chem.* 1992, 64, 2084.
53. Chien, B. M.; Lubman, D. M. *Anal. Chem.* 1994, 66, 1630.
54. Paul, W.; Steinwedel, H. U. *S. Patent* 2,939,952 1960.
55. Stafford, G. C.; Kelley, P. E.; Syka, J. E. P.; Reynolds, W. F.; Todd, J. F. *Int. J. Mass Spectrom. Ion Process.* 1984, 60, 85.
56. (a) Glish, G. L.; Goeringer, D. E.; Asano, K. G.; McLuckey, S. A. *Int. J. Mass Spectrom. Ion Process.* 1989, 94, 15. (b) Chamber, D. M.; Goeringer, D. E.; McLuckey, S. A.; Glish, G. *Anal. Chem.* 1993, 65, 14. (c) Van Berkel, G. J.; Glish, G. L.; McLuckey, S. A. *Anal. Chem.* 1990, 62, 1284. (d) Van Berkel, G. J.; McLuckey, S. A.; Glish, G. L. *Anal. Chem.* 1992, 64, 1586. (e) Van Berkel, G. J.; Asano, K. G. *Anal. Chem.* 1994, 66, 2096.
57. McLuckey, S. A.; Van Berkel, G. J.; Goeringer, D. E.; Glish, G. L. *Anal. Chem.* 1994, 66, 689A.
58. Louris, J. N.; Brodbelt, L. J. S.; Cooks, R. G.; Glish, G. L.; Van Berkel, G. J.; McLuckey, S. A. *Int. J. Mass Spectrom. Ion Proc.* 1990, 96, 117.
59. Schwartz, J. C.; Bier, M. E. *Rapid Commun. Mass Spectrom.* 1993, 7, 27.
60. Cooks, R. G.; Williams, J.; Cox, K.; Kaiser, K.; Schwartz, J. C. *Rapid Commun. Mass Spectrom.* 1991, 5, 327.
61. Katta, V.; Chowdhury, S. K.; Chait, B. T. *Anal. Chem.* 1991, 63, 174.
62. Yost, R. A.; Enke, C. G. *J. Am. Chem. Soc.* 1978, 100, 2274.

63. Dawson, P. H. *Quadrupole Mass Spectrometry and its Applications*, Dawson, P. H. Ed., Elsevier; Amsterdam, 1976.
64. Udseth, H. R.; Friedman, L. *Anal. Chem.* 1981, 53, 29.
65. Li, Y. T.; Hsieh, Y. L.; Henion, J. D.; Ganem, B. *J. Am. Soc. Mass Spectrom.* 1993, 4, 631.
66. Busch, K. L.; Glish, G. L.; McLuckey, S. A. *Mass Spectrometry/Mass Spectrometry: Techniques and Applications of Tandem Mass Spectrometry*, VCH publishers; New York, 1988.
67. Holland, J. F.; Enke, C. G.; Allison, J.; Stults, J. T.; Pinkston, J. D.; Newcome, B.; Watson, J. T. *Anal. Chem.* 1983, 55, 997A.
68. (a) Larsen, B. S.; McEwen, C. N. *J. Am. Soc. Mass Spectrom.* 1991, 2, 205. (b) Fabris, D.; Kelly, M.; Murphy, C.; Wu, Z.; Fenselau, C. *J. Am. Soc. Mass Spectrom.* 1993, 4, 652. (c) Murata, H.; Takao, T.; Shimonishi, Y. *Rapid Commun. Mass Spectrom.* 1994, 8, 205.
69. Cody, R. B.; Tamura, J.; Musselman, B. D. *Anal. Chem.* 1992, 64, 1561.
70. Dell, A.; Taylor, G. W. *Mass Spectrom. Rev.* 1984, 3, 319.
71. Williams, E. R.; Henry, K. D.; McLafferty, F. W. *J. Am. Chem. Soc.* 1990, 112, 6157.
72. Peiris, D. M.; Riveros, J. M.; Eyler, J. R. in *Proceedings of the 42<sup>nd</sup> ASMS Conference on Mass Spectrometry and Allied Topics* Chicago, IL, 1994.
73. Bruce, J. E.; Anderson, G. A.; Hofstadler, S. A.; Winger, B. E.; Smith, R. D. *Rapid Commun. Mass Spectrom.* 1993, 7, 700.
74. Campana, J. E. *Applied Spectroscopy in Material Science SPIE-The International Society for Optical Engineering*, 1991, 138.
75. Senko, M. W.; Beu, S. C.; McLafferty, F. W. *Anal. Chem.* 1994, 66, 415.
76. Yang, L. C.; Wilkins, C. L. *Org. Mass Spectrom.* 1989, 24, 409.
77. Peiris, D. M.; Cheeseman, M. A.; Ramanathan, R.; Eyler, J. R. *J. Phys. Chem.* 1993, 97, 7839.

78. McCrery, D. A.; Ledford, E. B.; Gross, M. L. *Anal. Chem.* 1982, 54, 1437.
79. Castro, M. E.; Russell, D. H. *Anal. Chem.* 1984, 56, 578.
80. Ghaderi, S.; Littlejohn, D. in *Proceedings of the 33<sup>rd</sup> ASMS Conference on Mass Spectrometry and Allied Topics* San Diego, CA, May 26-31, 1985, 727.
81. McIver, R. T.; Hunter, R. L.; Bowers, W. D. *Int. J. Mass Spectrom. Ion Proc.* 1985, 64, 67.
82. McIver, R. T. *Int. J. Mass Spectrom. Ion Proc.* 1990, 98, 35.
83. Kofel, P.; Allemann, M.; Kellerhals, H.; Wanczek, K. P. *Int. J. Mass Spectrom. Ion Proc.* 1985, 65, 97.
84. Kofel, P.; McMahon, T. B. *Int. J. Mass Spectrom. Ion Proc.* 1990, 98, 1.
85. Hofstadler, S. A.; Laude, D. A. *Anal. Chem.* 1992, 64, 569.
86. Hofstadler, S. A.; Laude, D. A. *J. Am. Soc. Mass Spectrom.* 1992, 3, 615.
87. Guan, Z.; Hofstadler, S. A.; Laude, D. A. *Anal. Chem.* 1993, 65, 1586.
88. Buseck, P. B.; Tsipursky, S. J.; Hettich, R. *Science*, 1992, 257, 215.
89. Amster, I. J.; Loo, J. A.; Furlong, J. P.; McLafferty, F. W. *Anal. Chem.* 1987, 59, 313.
90. Loo, J. A.; Williams, E. R.; Amster, I. J.; Furlong, J. J. P.; Wang, B. H.; McLafferty, F. W. *Anal. Chem.* 1987, 59, 1880.
91. Hill, N. C.; Marshall, A. G. in *Proceedings of the 38<sup>th</sup> ASMS Conference on Mass Spectrometry and Allied Topics* Tuscon, AZ, 1990, MP84.
92. Li, Y.; McIver, R. T.; Hunter, R. L. *Anal. Chem.* 1994, 66, 2077.
93. Henry, K. D.; Williams, E. R.; Wang, B. H.; McLafferty, F. W.; Shabanowitz, J.; Hunt, D. F. *Proc. Natl. Acad. Sci. USA* 1989, 86, 9075.
94. Henry, K. D.; McLafferty, F. W. *Org. Mass Spectrom.* 1990, 25, 490.

95. Henry, K. D.; Quinn, J. P.; McLafferty, F. W. *J. Am. Chem. Soc.* 1991, 113, 5447.
96. Beu, S. C.; Senko, M. W.; Quinn, J. P.; Wampler, F. M.; McLafferty, F. W. *J. Amer. Soc. Mass Spectrom.* 1993, 4, 557.
97. Chowdhury, S. K.; Katta, V.; Chait, B. T. *Rapid Commun. Mass Spectrom.* 1990, 4, 81.
98. Winger, B. E.; Hofstadler, S. A.; Bruce, J. E.; Udseth, H. R.; Smith, R. D. *J. Am. Soc. Mass Spectrom.* 1993, 4, 566.
99. Winger, B. E.; Hein, R. E.; Becker, B. L.; Campana, J. E. *Rapid Commun. Mass Spectrom.* 1994, 8, 495.
100. Kruppa, G. H.; Caravatti, P.; Radloff, C.; Zurcher, S.; Laukien, F.; Watson, C.; Wronka, J., in *FT-ICR/MS: Analytical Applications of Fourier Transform Ion Cyclotron Resonance Mass Spectrometry*; Asamoto, B., Ed., VCH; New York, 1991.
101. Buchanan, M. V.; Hettich, R. L. *Anal. Chem.* 1993, 65, 245A.
102. Koster, C.; Kahr, M. S.; Castoro, J. A.; Wilkins, C. L. *Mass Spectrom. Rev.* 1992, 11, 495.
103. Laude, D. A.; Johlman, C. L.; Brown, R. S.; Weil, D. A.; Wilkins, C. L. *Mass Spectrom. Rev.* 1986, 5, 107.
104. Dunbar, R. C. in *FT-ICR/MS: Analytical Applications of Fourier Transform Ion Cyclotron Resonance Mass Spectrometry*; Asamoto, B. Ed., VCH; New York, 1991.
105. Lawrence, E. O.; Livingston, M. S. *Phys. Rev.*, 1932, 40, 19.
106. Sommer, H.; Thomas, H. A.; Hipple, J. A. *Phys. Rev.* 1949, 76, 1877.
107. Wobschall, D.; Graham, J. R.; Malone, D. P. *Phys. Rev.*, 1963, 131, 1565.
108. McIver, R. T. *Rev. Sci. Instrum.* 1970, 41, 555. McIver, R. T. *Rev. Sci. Instrum.* 1970, 41, 555.
109. Comisarow, M. B.; Marshall, A. G. *Chem. Phys. Lett.* 1974, 25, 282.

110. Marshall, A. G.; Grosshans, P. B. *Anal. Chem.*, 1991, 63, 215A.
111. Grosshans, P. B.; Marshall, A. G. *Int. J. Mass Spectrom. Ion Proces.* 1992, 115, 1.
112. Buchanan, M. V.; Comisarow, M. B. in *Fourier Transform Mass Spectrometry: Evolution, Innovation and Applications*; ACS Symp. Series 359; Buchanan, M. V., Ed., American Chemical Society; Washington, DC, 1987.
113. Marshall, A. G.; Verdun, F. R. in *Fourier Transforms in NMR, Optical and Mass Spectrometry*, Elsevier; New York, 1990.
114. Hunter, R. L.; Sherman, M. G.; McIver, R. T. *Int. J. Mass Spectrom. Ion Phys.* 1983, 50, 259.
115. Comisarow, M. B.; Marshall, A. G. *Chem. Phys. Lett.* 1974, 25, 282.
116. Marshall, A. G.; Roe, D. C. *J. Chem. Phys.* 1980, 73, 1581.
117. Comisarow, M. B.; Marshall, A. G. *Chem. Phys. Lett.* 1974, 25, 489.
118. Kofel, P.; Allemann, M.; Kellerhals, H. P.; Wanczek, K. *Int. J. Mass Spectrom. Ion Proc.* 1986, 74, 1.
119. Wang, M.; Marshall, A. G. *Anal. Chem.* 1990, 62, 515.
120. Hanson, C. D.; Castro, M. E.; Kerley, E. L.; Russell, D. H. *Anal. Chem.* 1990, 62, 521.
121. Marshall, A. G.; Wang, T. -C.; Ricca, T. L. *Chem. Phys. Lett.* 1984, 108, 63.
122. Ijames, C. F.; Wilkins, C. L. *Chem. Phys. Lett.* 1984, 108, 58.
123. Marshall, A. G.; Wang, T. C. L.; Ricca, T. L. *J. Am. Chem. Soc.* 1985, 107, 7893.
124. Wang, T. C. L.; Ricca, T. L.; Marshall, A. G. *Anal. Chem.* 1986, 58, 2935.
125. McIver, R. T.; Hunter, R. L.; Baykut, G. *Anal. Chem.* 1989, 61, 489.
126. McIver, R. T.; Baykut, G.; Hunter, R. L. *Int. J. Mass Spectrom. Ion Proc.* 1989, 89, 343.

127. Comisarow, M. B.; Marshall, A. G. *Chem. Phys. Lett.* **1974**, *25*, 282.
128. Guan, S.; Gorshkov, M. V.; Marshall, A. G. *Chem. Phys. Lett.* **1992**, *198*, 143.
129. Schweikhard, L.; Blundschling, M.; Jertz, R.; Kluge, H. *J. Int. J. Mass Spectrom. Ion Proc.* **1989**, *89*, R7.
130. Rempel, D. L.; Ledford, E. B.; Huang, S. K.; Gross, M. L. *Anal. Chem.* **1987**, *59*, 2527.
131. Schweikhard, L.; Guan, S.; Marshall, A. G. *Int. J. Mass Spectrom. Ion Proc.* **1992**, *120*, 71.
132. Guan, S.; Xiang, X.; Marshall, A. G. *Int. J. Mass Spectrom. Ion Proc.* **1993**, *122*, 102.
133. Schweikhard, L.; Marshall, A.G. *J. Am. Soc. Mass Spectrom.* **1993**, *4*, 131.
134. Guan, S.; Wahl, M. C.; Wood, T. D.; Marshall, A. G. *Anal. Chem.* **1993**, *65*, 1753.
135. Speir, P. J.; Gorman, G. S.; Pitsenberger, C. C.; Turner, C. A.; Wang, P. P.; Amster, J. I. *Anal. Chem.* **1993**, *65*, 1746.
136. Kemper, R. P.; Bowers, M. T. in *Techniques for the Study of Ion-Molecule Reactions*, Farrar, J. M.; Saunders, W. H., Eds., John Wiley and Sons; New York, 1988.
137. Comisarow, M. B. *J. Chem. Phys.* **1978**, *69*, 4097.
138. Wronka, J.; Ridge, D. P. *Rev. Sci. Instrum.* **1982**, *53*, 491.
139. Huntress, W. T.; Simms, W. T. *Rev. Sci. Instrum.* **1973**, *44*, 1274.
140. Hofstadler, S. A.; Bruce, J. A.; Rockwood, A. L.; Anderson, G. A.; Winger, B. E.; Smith, R. E. *Int. J. Mass Spectrom. Ion Proc.* **1994**, *132*, 109.
141. Comisarow, M. W.; Marshall, A. G. *Int. J. Mass Spectrom. Ion Phys.* **1981**, *37*, 251.
142. Comisarow, M. B.; Marshall, A. G. *Chem. Phys. Lett.* **1974**, *26*, 489.
143. Hunter, R. L.; Sherman, M. G.; McIver, R. T. *Int. J. Mass Spectrom. Ion Phys.* **1983**, *50*, 259.

144. Kofel, P.; Allemann, M.; Kellerhalls, H. P.; Wanczek, K. *P. Int. J. Mass Spectrom. Ion Proc.* 1986, 74, 1.
145. Yin, W. W.; Wang, M.; Marshall, A. G.; Ledford, E. B. *J. Am. Soc. Mass Spectrom.* 1992, 3, 188.
146. Beu, S. C.; Laude, D. A. *Int. J. Mass Spectrom. Ion Phys.* 1992, 112, 215.
147. Vartanian, V. H.; Hadjarab, F.; Laude, D. A. in *42<sup>nd</sup> ASMS Conference on Mass Spectrometry and Allied Topics*, Chicago, IL. 1994.
148. Grosshans, P. B.; Wang, M.; Marshall, A. G. in *36<sup>th</sup> ASMS Conference on Mass Spectrometry and Allied Topics*, 1988, 592.
149. Caravatti, P.; Alleman, M. *Org. Mass Spectrom.* 1991, 26, 514.
150. Chen, R.; Marshall, A. G. *Int. J. Mass Spectrom. Ion Proc.* 1994, 133, 29.
151. Wang, M.; Marshall, A. G. *Anal. Chem.* 1989, 61, 1288.
152. Hanson, C. D.; Castro, M. E.; Kerley, E. L.; Russell, D. *H. Anal. Chem.* 1990, 62, 520.
153. Wang, M.; Marshall, A. G. *Anal. Chem.* 1990, 62, 515.
154. Gross, M. L.; Rempel, D. L. *Science*, 1984, 226, 261.
155. Ledford, E. B.; Rempel, D. L.; Gross, M. L. *Int. J. Mass Spectrom. Ion. Proc.* 1984, 55, 143.
156. Wang, M.; Marshall, A. G. *Int. J. Mass Spectrom. Ion Proc.* 1988, 31.
157. Ijames, C. F.; Wilkins, C. L. *J. Am. Chem. Soc.* 1988, 110, 2687.
158. Lebrilla, C. B.; Wang, D. T. S.; Hunter, R. L.; McIver, R. T. *Anal. Chem.* 1990, 62, 878.
159. Bose, G. M. *Recherches sur la cause et sur la veritable theorie de l'electricite* Wittenberg, 1745.
160. Pfeifer, R. J.; Hendricks, C. D. *AIAA J.* 1968, 6, 496.
161. Smith, D. P. H. *IEEE*, 1986, IA-22, 527.
162. Hayati, I.; Bailey, A.; Tadros, T. F. *J. Col. Inter. Sci.* 1987, 117, 222.

163. Ikonomou, M. G.; Blades, A. T.; Kebarle, P. *Anal. Chem.* 1991, 63, 1989.
164. Taylor, G. I. *Proc. R. Soc. London A*; 1964, A280, 383. Melcher, J. R.; Taylor, G. I. *Annu. Rev. Fluid Mech.* 1, 1969, 111.
165. Iribarne, I. V.; Thompson, B. A. *J. Chem. Phys.* 1976, 64, 2287.
166. Schmelzeisen-Redeker, R.; Butfering, L.; Rollgen, F. W. *Int. J. Mass Spectrom. Ion Proc.* 1989, 90, 139.
167. Lord Rayleigh *Philos. Mag.* 1882, 14, 31.
168. Taflin, D. C.; Zhang, S. H.; Allen, T.; Davis, E. J. *AIChe Journal* 1988, 34, 1310.
170. Waters/Extrel, P. O. Box 4508, Madison, WI
171. Ion Spec Corporation, Irvine, CA.
172. Bruker Instruments, Inc. Billerica, MA.
173. Hamdan, M.; Curcuto, O. *Int. J. Mass Spectrom. Ion Proc.* 1991, 108, 93.
174. Ramanathan, R.; Shalosky J. A.; Eyler, J. R. in *Proceedings of the 41<sup>st</sup> ASMS Conference on Mass Spectrometry and Allied Topics*, San Francisco, CA, 1993.
175. Barshick, C. B.; Eyler, J. R. *J. Am. Soc. Mass Spectrom.* 1993, 4, 387.
176. Ikonomou, M. G.; Blades, A. T.; Kebarle, P. *J. Am. Soc. Mass Spectrom.* 1991, 2, 497.
177. Wampler, F. W.; Blades, A. T.; Kebarle, P. *J. Am. Soc. Mass Spectrom.* 1993, 4, 289.
178. Tang, L.; Kebarle, P. *Anal. Chem.* 1991, 63, 2709.
179. Hayati, I.; Bailey, A. I.; Tadros, Th. F. *Nature* 1986, 319, 41.
180. Ikonomou, M. G.; Blades, A. T.; Kebarle, P. *Anal. Chem.* 1991, 63, 1989.
181. Ikonomou, M. G.; Blades, A. T.; Kebarle, P. *Anal. Chem.* 1990, 62, 957.

182. Siu, K. W. M.; Guevremont, R.; Le Blanc, J. C. Y.; O'Brien, R. T.; Berman, S. S. *Org. Mass Spectrom.* 1993, 28, 579.
183. Le Blanc, J. C. Y.; Beuchemin, D.; Siu, K. W. M.; Guevremont, R.; Berman, S. S. *Org. Mass Spectrom.* 1991, 26, 831.
184. Cusworth, W. H.; Turecek, F. in *The 40<sup>th</sup> ASMS Conference on Mass Spectrometry and Allied Topics*; 1992, Washington, DC, Pg. 199.
185. Campargue, R. *J. Phys. Chem.* 1984, 88, 4466.
186. Gray, A. L. *J. Anal. At. Spectrom.* 1989, 4, 371.
187. Hofstadler, S. A.; Schmidt, E.; Guan, Z.; Laude, D. A. *J. Am. Soc. Mass Spectrom.* 1993, 4, 168.
188. Nohmi, T.; Fenn, J. B. *J. Am. Chem. Soc.* 1992, 114, 3241.
189. Bourell, J. H.; Clauser, K. P.; Kelley, P.; Carter, P.; Stults, J. T. *Anal. Chem.* 1994, 66, 2088.
190. Lee, E. D.; Covey, T. R.; Henion, J. D. *Microcolumn. Sep.* 1989, 1, 14.
191. Smith, R. D.; Barinaga, C. J.; Udseth, H. R. *Anal. Chem.* 1988, 60, 1948.
192. Katta, V.; Chowdhury, S. K.; Chait, B. T. *J. Am. Chem. Soc.* 1990, 112, 5348.
193. Blades, A. T.; Jayaweera, P.; Ikonomou, M. G.; Kebarle, P. *Int. J. Mass Spectrom. Ion Proc.* 1990, 101, 325.
194. Blades, A. T.; Jayaweera, P.; Ikonomou, M. G.; Kebarle, P. *Int. J. Mass Spectrom. Ion Proc.* 1990, 102, 251.
195. Cheng, Z. L.; Siu, K. W. M.; Guevremont, R.; Berman, S. S. *J. Am. Soc. Mass Spectrom.* 1992, 3, 281.
196. Gatlin, C. L.; Turecek, F. *Anal. Chem.* 1994, 66, 712
197. Van Berkel, G. J.; Asano, K. G. *Anal. Chem.* 1994, 66, 2096.
198. Van Berkel, G. J.; McLuckey, S. A.; Glish, G. L. *Anal. Chem.* 1992, 64, 1586.
199. Katta, V.; Chowdhury, S. K.; Chait, B. T. *Anal. Chem.* 1991, 63, 174.

200. Guevremont, R.; Siu, K. W. M.; Le Blanc, Berman, S. S. *J. Am. Soc. Mass Spectrom.* 1992, 3, 216.
201. Balzani, V.; Scandola, F. *Supramolecular Photochemistry*, Horwood; Chichester, 1990.
202. Chow, C. S.; Barton, J. K. *J. Am Chem. Soc.* 1990, 112, 2839.
203. Wright, P. E.; Dyson, H. J.; Lerner, R. A. *Biochemistry* 1988, 27, 7167.
204. Taylor, J. W.; Kaiser, E. T. *Pharmacol. Rev.* 1986, 38, 291.
205. Meier, M.; Van Eldik, R.; Chang, I.; Mines, G. A.; Wuttke, D. S.; Winkler, J. R. *J. Am. Chem. Soc.* 1994, 116, 1577.
206. Cerny, R. L.; Sullivan, B. P.; Bursey, M. M.; Meyer, T. *J. Inorg. Chem.* 1985, 24, 397.
207. Liang, X.; Suwanrumpha, S.; Freas, R. B. *Inorg. Chem.* 1991, 62, 652.
208. Argazzi, R.; Bignozzi, C. A.; Bortolini, O.; Traldi, P. *Inorg. Chem.* 1993, 32, 1222.
209. Smith, R. D. *Proceedings of the 42<sup>nd</sup> Conference on Mass Spectrometry and Allied Topics*; Chicago, IL, May 29 - June 3, 1994.
210. Chowdhury, S. K.; Katta, V.; Chait, B. T. *J. Am. Chem. Soc.* 1990, 112, 9012.
211. Katta, V.; Chowdhury, S. K.; Chait, B. T. *J. Am. Chem. Soc.* 1990, 112, 5348.
212. Loo, J. A.; Loo, R. R. O.; Udseth, H. R.; Edmonds, C.G.; Smith, R. D. *Rapid Commun. Mass Spectrom.* 1991, 5, 101.
213. Blades, A. T.; Jayaweera, P.; Ikonomou, M. G.; Kebarle, P. *Int. J. Mass Spectrom and Ion Proc.* 1990, 101, 325.
214. Eyler, J. R.; Richardson, D. E. *J. Am. Chem. Soc.* 1985, 107, 6130.
215. Watson, C. H.; Baykut, G.; Eyler, J. R. *Anal. Chem.* 1987, 59, 1133.
216. Unger, S. E. *Anal. Chem.* 1987, 57, 776.

217. (a) Branan, D. M.; Hoffman, N. W.; McElroy, E. A.; Ramage, D. L.; Robbins, M. J.; Eyler, J. R.; Watson, C. H.; Leary, J.A. *Inorg. Chem.* 1990, 29, 1915. (b) Bruce, M. I.; Liddell, M. J. *Appl. Organomet. Chem.* 1987, 1, 191. (c) Cerny, R. L.; Sullivan, B. P.; Bursey, M. M.; Meyer, T. J. *Inorg. Chem.* 1985, 24, 397.
218. (a) Tanaka, M.; Nagai, T.; Miki, E. *Inorg. Chem.* 1989, 28, 1704. (b) Feld, H.; Angelika, L.; Rading, D.; Benninghoven, A.; Reusmann, G.; Krebs, B. *Int. J. Mass Spectrom. and Ion Proc.* 1991, 11, 225. (c) Pierce, J. L.; Busch, K. L.; Cooks, R. G.; Walton, R. A. *Inorg. Chem.* 1982, 21, 2597.
219. (a) Panell, L. K.; Fales, H. M.; Scovill, J. P.; Klayman, D. L.; West, D. X.; Tate, R. L. *Transition Met. Chem.* 1985, 10, 141. (b) Feld, H.; Angelika, L.; Rading, D.; Benninghoven, A.; Reusmann, G.; Krebs, B. *Int. J. Mass Spectrom. and Ion Proc.* 1991, 11, 225.
220. Chan, K. W. S.; Cook, K. D. *J. Am. Chem. Soc.* 1982, 104, 5031.
221. (a) Beavis, D.; Lindner, J.; Grottemeyer, J.; Atkinson, D. A.; Keene, F. R.; Knight, A. E. W. *J. Am. Chem. Soc.* 1988, 110, 7534. (b) Grottemeyer, J.; Bosel, U.; Walter, K.; Schlag, E. W. *Org. Mass Spectrom.* 1986, 21, 645.
222. (a) Bjarnason, A.; Desenfansrana, D. M.; Barr, M. E.; Dahl, L. F. *Organometallics*, 1990, 9, 657. (b) Marshall, A. G.; Mullen, S. L.; Shomo, R. E., II; Weisenberger, C. R. *Proceedings of the 33<sup>rd</sup> Conference on Mass Spectrometry and Allied Topics*; San Diego, CA, May 31-June 4, 1985.
223. Wong, S. F.; Meng, C. K.; Fenn, J. B. *J. Phys. Chem.* 1988, 92, 546.
224. (a) Tang, L.; Kebarle, K. *Anal. Chem.* 1991, 63, 2709. (b) Thomson, B. A.; Iribarne, J. V. *J. Chem. Phys.* 1979, 71, 4451.
225. Balley, A. G. *Electrostatic Spraying of Liquids*, John Wiley; New York, 1988.
226. Fenn, J. B. *J. Am. Soc. Mass Spectrom.* 1993, 4, 525.
227. Guevremont, R.; LeBlanc, J. C. Y.; Siu, K. W. M. *Org. Mass Spectrom.* 1993, 28, 1345.
228. Carlin, T. J.; Freiser, B. S. *Anal. Chem.* 1983, 55, 574.

229. Loo, J. A...; Udseth, H. R.; Smith, R. D. *Rapid Commun. Mass Spectrom.* 1988, 2, 207.
230. Katritzky, A. R.; Watson, C. H.; Szafran, Z. D.; Eyler, J. R. *J. Am. Chem. Soc.* 1990, 112, 2471.
231. Cole, L. D.; Barigelli, F.; Balzani, V.; Belser, P.; Von Zelewsky, A.; Seel, C.; Frank, M.; Vogtle, F. *Coord. Chem. Rev.* 1991, 111, 225.
232. Nazeeruddin, M. K.; Kay, A.; Radicio, I.; Humphry-Baker, R.; Muller, E.; Liska, P.; Valachopoulos, N.; Gratzel, M. *J. Am. Chem. Soc.* 1993, 115, 6382.
233. Miller, J. M.; Balasamugan, K.; Nye, J.; Deacon, G. B.; Thomas, N. C. *Inorg. Chem.* 1987, 26, 560.
234. Van der Ploeg, A. F. M. J.; Van Koten, G. *Inorg. Chim. Acta.* 1981, 51, 225.
235. Che, C. M.; Kwong, H. L.; Poon, C. K.; Yam, V. W. W. *J. Chem. Soc. Dalton Trans.* 1990, 3215.
236. Obendorf, D.; Probst, M.; Peringer, P.; Falk, H.; Muller, N. *J. Chem. Soc. Dalton Trans.* 1988, 1709.
237. Analytica of Branford, Inc., 29, Business Park Drive, Branford, CT 06405.
238. Yersin, H.; Gallhuber, E.; Vogler, A.; Kunkely, H. *J. Am. Chem. Soc.*, 1983, 105, 4155.
239. Busch, K. L.; Cooks, R. G.; Walton, R. A.; Wood, K. V. *Inorg. Chem.* 1984, 23, 4093.
240. DeKock, R. L.; Van Zee, R. D.; Ziegler, T. *Inorg. Chem.* 1987, 26, 563.
241. Gaspar, R.; Tamassy-Lentei, I. *Acta Phys. Acad. Sci. Hung.* 1981, 50, 343.
242. Liang, X.; Suwanrumpha, S.; Freas, R. B. *Inorg. Chem.* 1991, 30, 652.
243. Ramanathan, R.; Dejupa, C.; Eyler, J. R. *Proceedings of the 42<sup>nd</sup> Conference on Mass Spectrometry and Allied Topics*; Chicago, IL, May 29 - June 3, 1994.
244. Allemann, M.; Kellerhals, H. -P.; Wanczek, K. -P. *Int. J. Mass Spectrom. Ion Proc.* 1983, 46, 139.

245. Hahn, O.; Strassman, F.; Mattauch, J.; Ewald, H. *Naturwiss.*, 1942, 30, 541.
246. Marks, R. W. *The Dymaxion World of Buckminster Fuller*, Reinhold; New York, 1960.
247. Kroto, H. W.; Heath, J. R.; O'Brien, S. C.; Curl, R. F.; Smalley, R. E. *Nature*, 1985, 318, 162.
248. (a) Kraetschmer, W.; Lamb, L. D.; Fostiropoulos, K.; Huffman, D. R. *Nature*, 1990, 347, 354. (b) Haufler, R. E.; Chai, Y.; Chibante, L. P. F.; Conceicao, J.; Changming, J.; Lai, S. W.; Maruyama, S.; Smalley, R. E. *Mater. Res. Soc. Proc.* 1991, 206, 627.
249. Greenwood, P. E. *Org. Mass Spectrom.* 1994, 29, 61.
250. Jarrold, M.F.; Ray, U.; Creegan, K.M. *J. Chem. Phys.* 1990, 93, 224.
251. Trevor, D.J.; Cox, D.M.; Kaldor, A. *J. Am. Chem. Soc.* 1990, 112, 3742.
252. Petrie, S.; Javahery, G.; Bohme, D. K. *Astron. Astrophys.* 1993, 271, 662.
253. Brill, F. W.; Eyler, J. R. *J. Phys. Chem.* 1981, 85, 1091.
254. Chupka, W.A.; Inghram, M.G. *J. Chem. Phys.* 1953, 21, 1313.
255. Drowart, J.; Burns, R. P.; DeMaria, G.; Inghram, M. G. *J. Chem. Phys.* 1959, 31, 1131.
256. Furstenau, N.; Hillenkamp, F.; Nitsche, R. *Int. J. Mass Spectrom. Ion Phys.* 1979, 31, 85.
257. Honig, R. E. *Adv. Mass Spectrom.* 1963, 2, 25.
258. Rohlfing, E. A.; Cox, D. M.; Kaldor, A. *J. Chem. Phys.* 1984, 81, 3322.
259. Rohlfing, E. A. *J. Chem. Phys.* 1990, 93, 7851.
260. Campbell, E. E. B.; Ulmer, G.; Hasselberger, B.; Busmann, H. G.; Hertel, I. V. *J. Chem. Phys.* 1990, 93, 6900.
261. So, H. Y.; Wilkins, C. L. *J. Phys. Chem.* 1989, 93, 1184.
262. Pitzer, K.S.; Clementi, E. *J. Amer. Chem. Soc.* 1959, 81, 4477.

263. Ewing, D.W.; Pfeiffer, G.V. *Chem. Phys. Lett.* 1982, 86, 365.
264. Strickler, S.J.; Pitzer, K.S. in *Molecular Orbitals in Chemistry*, edited by Pullman, B and Lowdin, P.O. Academic Press; New York, 1964, 281.
265. Weltner, W. Jr.; McLeod, D. Jr. *J. Chem. Phys.* 1966, 45, 3096.
266. Weltner, W. Jr.; Van Zee, R.J. *Chem. Rev.* 1989, 89, 1713.
267. Kroto, H.W. *Chem. Soc. Rev.* 1982, 11, 435.
268. Herbst, E. *Angew. Chem. Int. Ed. Engl.* 1990, 29, 595.
269. Cody, R.B.; Burnier, R.C.; Reent, W.D. Jr.; Carlin, T.J.; McCrery, D.A.; Lengel, R.K.; Freiser, B.S. *Int. J. Mass Spectrom. Ion Proc.* 1980, 33, 37. Wilkins, C.L.; Gross, M.L. *Anal. Chem.* 1981, 53, 1661A.
270. Katritzky, A.R.; Malhotra, N.; Ramanathan, R.; Kemerait, R.C. Jr.; Zimmerman, J.A.; Eyler, J.R. *Rapid Commun. Mass Spectro.* 1992, 6, 25.
271. Brown, R.S.; Wilkins, C.L. *Anal. Chem.* 1986, 58, 3196.
272. Nicol, G.R.; Pan, Y.; Ridge, D.P. *39th Annual Conference on Mass Spectrometry and Allied Topics*, Nashville, Tennessee, 1991, 360.
273. Brown, C.E.; Kovacic, P.; Welch, K.J.; Cody, R.B.; Hein, R.E.; Kinsinger, J.A. *Polym. Plast. Technol. Eng.* 1988, 27, 487.
274. Shomo, R.E.; Marshall, A.G.; Weisenberger, C.R. *Anal. Chem.* 1985, 57, 2940.
275. Hettich, R.L.; Buchanan, M.V. *39th Annual Conference on Mass Spectrometry and Allied Topics*, Nashville, Tennessee, 1991, 929. Beavis, R.C.; Chait, B.T. *Rapid Commun. Mass Spectro.* 1989, 3, 432.
276. McElvany, S.W.; Dunlap, B.I.; O'Keefe, A. *J. Chem. Phys.* 1987, 86, 715.
277. McElvany, S.W. *J. Chem. Phys.* 1988, 89, 2063.
278. Parent, D.C.; McElvany, S.W. *J. Am. Chem. Soc.* 1989, 111, 2393.

279. Yang, S. H.; Pettiette, C. L.; Conceicao, J.; Cheshnovsky, O.; Smalley, R. E. *Chem. Phys. Lett.* 1987, 139, 233.
280. Yang, S.; Taylor, K. J.; Craycraft, M. J.; Conceicao, J.; Pettiette, C. L.; Cheshnovsky, O.; Smalley, R. E. *Chem. Phys. Lett.* 1988, 144, 431.
281. Lias, S.G.; Bartmess, J.E.; Liebman, J.F.; Holmes, J.L.; Levin, R.D.; Mallard, W.G. *J. Phys. Chem. Ref. Data* 1988, 17.
282. Pozniak, B.; Dunbar, R. C. *Int. J. Mass Spectrom. Ion Proc.* 1994, 133, 97.
283. Bruce, J. E.; Eyler, J. R. in *The 40<sup>th</sup> ASMS Conference on Mass Spectrometry and Allied Topics* Washington, DC, 1992, pg. 126.
284. Arnold, C. C.; Zhao, Y.; Kitsopoulos, T. N.; Neumark, D. M. *J. Chem. Phys.* 1992, 97, 6121.
285. Arnold, C. C.; Bradforth, S. E.; Kitsopoulos, T. N.; Neumark, D. M. *J. Chem. Phys.* 1991, 95, 8753.
286. Kitsopoulos, T. N.; Chick, C. J.; Zhao, Y.; Neumark, D. M. *J. Chem. Phys.* 1991, 95, 5479.
287. Kitsopoulos, T. N.; Chick, C. J.; Zhao, Y.; Neumark, D. M. *J. Chem. Phys.* 1991, 95, 1441.
288. Watts, J. D.; Bartlett, R. J. *J. Chem. Phys.* 1994, 101, 409.
289. Watts, J. D.; Bartlett, R. J. *J. Chem. Phys.* 1992, 97, 3445.
290. Watts, J. D.; Bartlett, R. J. *J. Chem. Phys.* 1992, 96, 6073.
291. Adamowicz, L. *J. Chem. Phys.* 1992, 96, 6073.
292. Watts, J. D.; Cernusak, I.; Bartlett, R. J. *J. Chem. Phys. Lett.* 1991, 178, 259.
292. Ortiz, J. V. *J. Chem. Phys.* 1993, 99, 6716.
293. Bernholdt, D. E.; Mayers, D. H.; Bartlett, R. J. *J. Chem. Phys.* 1988, 89, 3612.
294. Bach, S.B.H.; Eyler, J.R. *J. Chem. Phys.* 1990, 92, 358.

295. Ramanathan, R.; Zimmerman, J. A.; Eyler, J. R. *J. Chem. Phys.* 1993, 98, 5790.
296. Zimmerman, J.A.; Eyler, J.R.; Bach, S.B.H.; McElvany, S.W. *J. Chem. Phys.* 1991, 94 , 3556
297. Zimmerman, J.A.; Bach, S.B.H.; Watson, C.H.; Eyler, J.R.; *J. Chem. Phys.* 1991, 95, 98.
298. Cheeseman, M.A.; Eyler, J.R. *J. Phys. Chem.* 1992, 96, 1082.
299. Bruce, J. E. *PhD Dissertation*, University of Florida, 1992.
300. McElvany, S. W. *Int. J. Mass Spectrom. Ion Proc.* 1990, 102, 81.
301. Knight, R. D.; Walch, R. A.; Foster, S. C.; Miller, T. A.; Mullen, S. L.; Marshall, A. G. *Chem. Phys. Lett.* 1986, 129, 331.
302. Yamashita, M.; Fenn, J. B. *J. Phys. Chem.* 1984, 88, 4671.

#### BIOGRAPHICAL SKETCH

Ragulan Ramanathan was born on September 18, 1966, in Jaffna, Sri Lanka and is son of Saravanamuttu Ramanathan and Sakuntala Ramanathan. He has two younger brothers, Ragavan and Muhunthan. The author received his high school education from St. John's College, in Jaffna, Sri Lanka. He graduated in May of 1988 from The University of Southern Mississippi, receiving a Bachelor of Science degree in chemistry. In January of 1989, he began his graduate studies at the University of Florida. In October of 1989, he joined the research group directed by Dr. John R. Eyler. Following the completion of his master's program, he continued his doctoral studies under the guidance of Dr. Eyler.

I certify that I have read this study and that in my opinion it conforms to acceptable standards of scholarly presentation and is fully adequate, in scope and quality, as a dissertation for the degree of Doctor of Philosophy.

John R. Eyler  
John R. Eyler, Chairman  
Professor of Chemistry

I certify that I have read this study and that in my opinion it conforms to acceptable standards of scholarly presentation and is fully adequate, in scope and quality, as a dissertation for the degree of Doctor of Philosophy.

Martin T. Vala  
Martin T. Vala  
Professor of Chemistry

I certify that I have read this study and that in my opinion it conforms to acceptable standards of scholarly presentation and is fully adequate, in scope and quality, as a dissertation for the degree of Doctor of Philosophy.

Robert J. Hanrahan  
Robert J. Hanrahan  
Professor of Chemistry

I certify that I have read this study and that in my opinion it conforms to acceptable standards of scholarly presentation and is fully adequate, in scope and quality, as a dissertation for the degree of Doctor of Philosophy.

Kirk S. Schanze  
Kirk S. Schanze  
Associate Professor of  
Chemistry

I certify that I have read this study and that in my opinion it conforms to acceptable standards of scholarly presentation and is fully adequate, in scope and quality, as a dissertation for the degree of Doctor of Philosophy.

Gar B. Hoflund

Gar B. Hoflund  
Professor of Chemical  
Engineering

This dissertation was submitted to the Graduate Faculty of the Department of Chemistry in the College of Liberal Arts and Sciences and to the Graduate School and was accepted as partial fulfillment of the requirements for the degree of Doctor of Philosophy.

December 1994

---

Dean, Graduate School